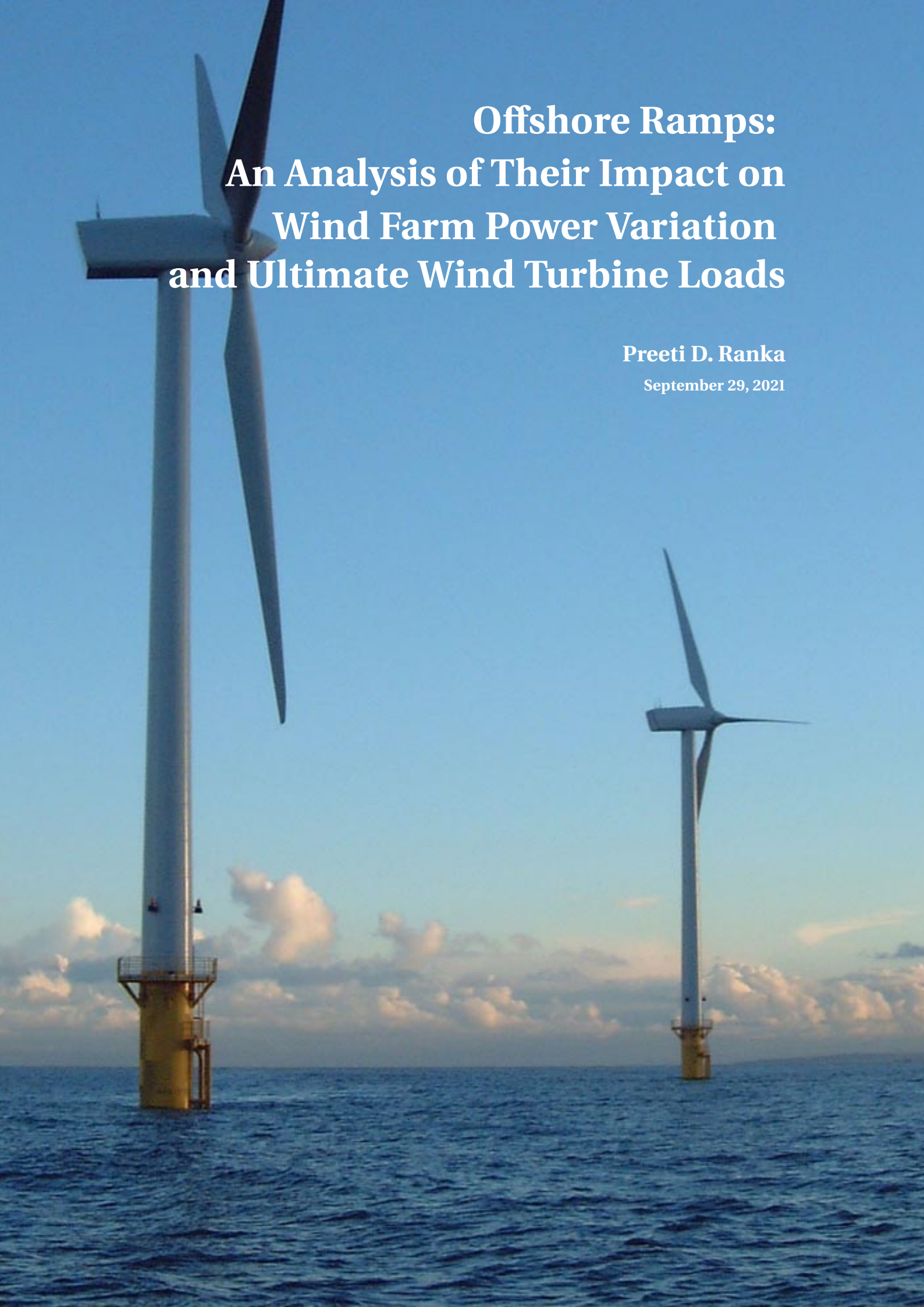

Offshore Ramps: An Analysis of Their Impact on Wind Farm Power Variation and Ultimate Wind Turbine Loads

Preeti D. Ranka

September 29, 2021

Offshore Ramps: An Analysis of their Impact on Wind Farm Power Variation and Ultimate Wind Turbine Loads

A measurement-based approach for improving ultimate design-driving loads modelling

by

Preeti Ranka

to obtain the degree of Master of Science in Sustainable Energy Technology
at the Delft University of Technology,

Wind Energy Group, Faculty of Aerospace Engineering, Delft University of Technology,

Faculty of Electrical Engineering, Mathematics and Computer Science, Delft University of Technology

Siemens Gamesa Renewable Energy

Student number: 5030811

Thesis committee:

Dr.ir. W. A. A. M. Bierbooms,	TU Delft, supervisor
Dr. Laura Valldecabres Sanmartin,	Siemens Gamesa, supervisor
Dr. Sebastian Schafhirt ,	Siemens Gamesa, supervisor
Prof.dr. S. J. Watson	TU Delft
Dr. S. R. de Roode	TU Delft

September 29, 2021

TU Delft Delft University of Technology

SIEMENS Gamesa

Acknowledgement

I owe gratitude to many people for keeping me motivated during the pandemic, shaping my critical thinking, and interesting discussions.

I would like to start by thanking my family, especially Varsha, for their constant emotional and financial support. It is while pursuing Masters when you realise the monetary value of time, and I feel privileged to have had their support and backing to further my education.

Foremost credit of the success of this thesis goes to my thesis supervisors at SGRE and TU Delft. This thesis is the result of your constant support, motivation, knowledge, and expertise. In particular, I wish to thank Laura Valldecabres for investing significant time, providing thorough corrections, interesting discussions, excellent guidance, and being patient with my writing. I enjoyed working on the turbulence intensity problem together, which made me think how amazing this thesis would have been in case of no pandemic. I also owe thanks to Sebastian Schafhirt. Your knowledge and expertise in load, constructive discussions, patience and constant inspiration throughout the thesis were admirable. My appreciation extends to Wim Beirbooms for encouraging me to write a report since the start of this project and for critical feedback. Your words "at TU Delft we give importance to the quality results rather than quantity" encouraged me to develop critical and qualitative thinking.

I am grateful to Sachin Navalkar, Alexandros Iliopoulos, Valentin Bernard, and Soeren Vittarp for being patient with my data requirements, approachable and patiently handling my doubts. My gratitude extends to Simon Watson and Stephan de Roode for being part of the thesis committee and to help out with your expertise. A special thanks to Mihir Mehta and Rameen Ghauri for their constant technical support.

Surviving in this pandemic was possible due to my beloved friends at TU Delft and my dance group DDC. A special thank you to Agney, Devyani, Maitheli, and Avikar for help with writing and all amazing dinners. Staying motivated would not have been possible without the company of Kunal Mavani and our chess games. A final thanks to Aditya Ghate for encouraging and persuading me to stay productive, focused and improve my skills.

Summary

With the growing offshore wind industry, ramp events, i.e., significant variation in wind power and wind speed within a short period of time, have become of critical importance to the end-users. The analysis of offshore wind power ramp events from the perspective of grid operators or energy traders is prevalent in the literature. However, this area of research is still evolving. Existing studies have not adequately addressed the influence of the techniques used to normalize wind farm power on end-users. In addition, the selection of the minimum number of turbines criterion and its effect on the detection of ramp events, threshold value, or smoothing of power fluctuations have not been studied so far. Moreover, little research has been conducted on analyzing the impact of ramp events on ultimate wind turbine loads. To the best of the author's knowledge, the results have not yet been validated with measurements. Therefore, the primary objective of this report is

"to investigate the impact of wind-induced ramp events on the offshore wind farm power and ultimate wind turbine loads - a measurement-based approach"

At first, a wind power ramp detection algorithm is developed from the perspective of a wind turbine designer. The algorithm is developed using two years of 10-min measurement statistics provided by Siemens Gamesa Renewable Energy (SGRE). The analysis is performed for two offshore wind farms, Westermost Rough and Dudgeon, of different sizes. After a thorough literature review, a suitable ramp detection definition is selected based on the available data set, an end-user's objective, and power fluctuation smoothing effect. This thesis also discusses the significance of wind farm power normalization techniques for end-users. The aggregated power is normalized by the nominal capacity of the available number of wind turbines at each time step. The selection is based on identifying the wind-induced ramp events by removing the effect of variability of a turbine's data availability. Afterwards, the criterion of minimum number of available turbines is selected by considering the wind farm layout and power fluctuation smoothing effect. Using the ramp detection algorithm, the characteristics of the observed wind power ramp events in the two wind farms are compared. The analysis revealed that the wind power ramp events were mainly related to the non-linearity of the power curve. Moreover, the number of ramp events showed a decreasing trend with increasing wind speed, turbulence intensity, ramp duration, and wind direction changes. Furthermore, the provided measurement data does not adequately capture the correlation or travel time of large-scale ramp events within the two wind farms. Therefore, detailed meteorological information with the high spatial and temporal resolution is necessary for thorough analysis.

Following that, the influence of wind power and wind speed ramp events on the ultimate wind turbine loads are examined. The initial analysis is conducted on a 10-min basis for a single turbine at the Dudgeon wind farm. It is found that 10-min wind speed ramps could be the extreme load governing factor when a pitch controller is inactive, whereas wind power ramp events show no influence. Subsequently, extreme wind speed fluctuations events were found to be a governing factor for wind speed bins that fall under inactive pitch or above rated wind speed region.

Subsequently, the loads associated with extreme wind speed fluctuations are compared to the aeroelastic simulations of the extreme turbulence load case as prescribed by the International Electrotechnical Commission (IEC). In general, the measured loads associated with extreme fluctuations did not outperform the simulations, except for the tower side-side moments. Besides, it is found that extreme loads near rated wind speed region exceed the simulation results, but the values are not related to the extreme fluctuations. It is worth mentioning that the average simulation loads show a good agreement with the average measurements. Thus, the obtained results do not contain significant uncertainties.

Finally, the high-frequency data of some specific events are examined. The analysis of the blade root flap-wise moments has shown that the extreme bending moments per wind speed bin are mainly caused by a sudden fluctuation in the wind speed time series leading to the transition of the pitch angle from the inactive to the active region. Therefore, the extreme loads over the entire wind speed range, except near rated wind speed, are governed by extreme turbulence or ramp events that involve pitch transition. Around rated wind speed, extreme loads are caused by comparatively lower fluctuations, but higher than the normal turbulence prescribed by the IEC. However, the higher fluctuations that occur during active pitch do not result in higher loads.

In conclusion, for the ultimate load analysis, the wind speed time series for the extreme turbulence model should include a sudden transition of a pitch angle from inactive to the active region. However, as the high-frequency analysis is only conducted based on the blade root flap-wise moment, further investigation of other moments is vital.

Contents

Nomenclature

Acronyms and Abbreviations

BHawC	Bonus energy Horizontal axis wind turbine Code
CWT	Continuous Wavelet Transform
DLC	Design load case
DUD	Dudgeon wind farm
ECD	Extreme coherent gust with direction change
ETM	Extreme Turbulence Model
EWS	Extreme wind shear
I	Indicator function
IEC	International Electrotechnical Commission
LLJ	Low-Level Jet
NaN	Not a number
NCM	Normal Current Model
NTM	Normal turbulence model
OWT	Offshore Wind Turbine
PLM	Power Load Management
PSD	Power spectral density
RNA	Rotor Nacelle assembly
SCADA	Supervisory Control and Data Acquisition
TBFA	Tower base fore-aft moment
TBSS	Tower base side-side moment
TI	Turbulence intensity
TTFA	Tower top fore-aft moment
TTSS	Tower top side-side moment
WMR	Westermost Rough wind farm

Symbols

ΔDr_f	Change in the wind direction of wind farm ramp events	$[^o]$
ΔP	Power differences time series	$[W]$
ΔP_f	Wind farm power differences time series	$[W]$
ΔP_n	Normalized power differences time series	$[-]$

ΔP_{fn}	Normalized wind farm power differences time series	[–]
ΔP_{rn}	Normalized ramp amplitude	[–]
ΔTI_f	Change in the turbulence intensity of wind farm ramp events	[–]
Δu_f	Change in the wind speed of wind farm ramp events	$[m/s]$
Δ_t	Time duration of ramp event - refers to rise/fall time of a ramp	[s]
κ	von Karman's constant	[-]
Ω	Generator rotational speed	[rpm]
ϕ_{MET}	Meteorological wind direction	$[^o]$
ϕ_{POLAR}	Wind direction in polar system	$[^o]$
ϕ_{VECT}	Wind azimuth angle (Oceanographic convention)	$[^o]$
ψ	Yaw angle	$[^o]$
ψ_{max}	10-min maximum yaw angle	$[^o]$
ψ_{min}	10-min minimum yaw angle	$[^o]$
$\sigma(\Delta P)$	Standard deviation of power differences	$[W]$
$\sigma(\Delta P_f)$	Standard deviation of wind farm power differences	$[W]$
$\sigma(\Delta P_n)$	Standard deviation of normalized power differences	[–]
$\sigma(\Delta P_{fn})$	Standard deviation of the normalized wind farm power differences	[–]
σ_p	Standard deviation of power fluctuations	$[W]$
σ_u	Standard deviation of 10 min horizontal wind speed	$[m/s]$
σ_{pfn}	Standard deviation of the normalized wind farm power fluctuations	[–]
σ_{pf}	Standard deviation of wind farm power fluctuations	$[W]$
σ_{pn}	Standard deviation of the normalized power fluctuations	[–]
σ_{u90}	Standard deviation representing 90% quantile	$[m/s]$
σ_{uf}	Standard deviation of 10 min wind farm speed	$[m/s]$
τ	Generator torque	$[Nm]$
θ	Pitch angle of blade A	$[^o]$
θ_{min}	10-min minimum pitch angle of blade A	$[^o]$
a	Angle between sensor location of tower and north direction	$[^o]$
A_c	Charnok's constant	[-]
F_n	Thrust force	$[N]$
g	acceleration due to gravity	$[m/s^2]$
I_{15}	Average turbulence intensity at 15 m/s wind speed at hub height	[-]
I_{ref}	reference turbulence intensity	[-]
k	Sample time interval	[s]

M_n	Normalized bending moment	[–]
M_{FA}	Tower fore-aft moment	$[Nm]$
M_{SS}	Tower side-side moment	$[Nm]$
M_x	Calibrated moment at x-axis based on the sensor location	$[Nm]$
M_y	Calibrated moment at y-axis based on the sensor location	$[Nm]$
N	Number of wind turbines in a wind farm	[–]
n_{am}	No. of average power differences	[–]
n_{th}	Number of detected ramp events at the threshold value	[–]
P	Power time series	$[W]$
p'	Power fluctuations	$[W]$
P_t^f	Transformed power signal	$[W]$
P_{tn}^f	Normalized transformed power signal	[–]
p_f'	Wind farm power fluctuations	$[W]$
P_n	Normalized power time series	[–]
p_n'	Normalized power fluctuations	[–]
P_R	Rated power	$[W]$
P_{fn}	Normalized wind farm power time series	[–]
p_{fn}'	Normalized wind farm power fluctuations	[–]
P_f	Wind farm power time series	$[W]$
P_{limit}	Power limit	$[W]$
P_{val}	% Threshold power value	[–]
PRR_{val}	% Threshold power ramp rate value	[–]
r_D	Correlation coefficient for turbines in Dudgeon farm	[–]
r_W	Correlation coefficient for turbines in WMR farm	[–]
r_{DW}	Correlation coefficient between parameters of Dudgeon and WMR farms	[–]
r_{pij}	Correlation coefficient between power signals of two turbines 'i' and 'j'	[–]
t	Time	[s]
T_E	End time of a ramp event	[s]
T_s	Start time of a ramp event	[s]
t_w	Time window	[s]
TI_f	Turbulence intensity of a wind farm	[–]
u	10-min mean wind speed at hub height	$[m/s]$
u_{ave}	average of wind speed time series	$[m/s]$
u_f	10-min average wind speed of a wind farm	$[m/s]$

x	A positive real number	[–]
z	hub height	[m]
z_0	surface roughness parameter	[m]
u_E	Wind velocity vector towards east	$[m/s]$
u_N	Wind velocity vector towards north	$[m/s]$
V_H	Horizontal wind velocity vector	$[m/s]$

List of Figures

1 Introduction

Offshore wind energy is growing rapidly with an installed capacity of 29 GW and is expected to reach 234 GW by 2030 [1]. Various factors drive this rapid growth. For instance, deteriorating climate and depleting fossil fuel resources demand cleaner energy alternatives. Moreover, compared to onshore, offshore sites show higher wind potential. Their locations, being farther from human society, provide additional benefits of reduced visual impact, lower noise issues, and increased space availability, which allow turbines to be built larger for yielding more energy [2]. Conversely, the considerable similarity between offshore and onshore turbines and mature technologies of the onshore field have accelerated the growth of offshore wind energy [3]. Furthermore, the improved simulation and design optimization tools have led to significant cost reduction. As a result, the world's first subsidy-free wind farm will come into effect by 2022 [4].

Nonetheless, further cost reduction is necessary to fulfil 30% of global electricity needs by using offshore wind energy by 2050, which is 0.3% at present [5]. The potential pathways include increasing revenue by maximising energy yield and reducing costs by minimising extreme loads and material usage [6, 7]. Traditionally, the energy yield can be improved by increasing the rotor diameter, which increases the swept area, and thus the power output [6]. In addition, the design of an offshore wind turbine (OWT) is optimized to lower the use of materials. However, the expected growth is significantly hindered because of environmental uncertainties. For example, the power fluctuations caused by varying wind conditions significantly slow down the energy gain. Besides, OWTs have to survive against the offshore environmental uncertainties over their designed lifetime. Therefore, OWTs are simulated against these extreme conditions by using a synthesized wind speed time series. If these time series do not adequately capture the extreme environmental conditions, this can even lead to the failure of an OWT or its components, adding up the unplanned costs of maintenance, labour, materials, etc., which account for more than 30% of the total cost [6, 7]. Overly conservative designs also increase the material costs [8]. Moreover, the unavailability of OWTs for a certain time also affects the energy yield of a wind farm. Therefore, understanding the impact of unexpected extreme changes in wind speed on the components of OWTs and their performance is of paramount importance for the growth of the offshore wind industry [9].

1.1. Importance of ramp events to the offshore wind industry

As aforesaid, the growing offshore industry faces limitations due to environmental uncertainties, where ramp events have a significant influence [2, 10]. A ramp event is characterised as a sudden and significant shift in power or wind speed in a short time period [11]. Yet, there are no universally defined values for a ramp period and amplitude, but they vary as per the end user's objective and local site conditions [12]. Figure 1.1 illustrates an example of three ramp events in an OWT's power output induced by ramp-like changes in the horizontal wind speed. When a ramp event is associated with an increase in power (or wind speed), it is referred to as a ramp-up, whereas the decrease is known as a ramp-down.

Figure 1.1: An example of observed wind power and speed ramp events at the Dudgeon wind farm.

The significance of ramp events in the offshore wind industry is explained from different perspectives of **end-users**. Here, end-users are the ones whose tasks get affected by ramp events.

- **Wind turbine designer:** A wind turbine designer aims for a cost-effective and efficient design that yields significant power. These OWTs are designed using extensive simulation tools, where synthesised wind speed time series are one of the major inputs. The time series are generally developed using statistics of wind data, representing normal and extreme weather conditions that an OWT may face during its service life. Besides, extreme loads are estimated using extrapolation methods. An unexpected events, which are not sufficiently captured in the existing synthetic time series, could lead to extreme loads on an OWT. One of such events are ramp events [2, 13]. Moreover, short-period ramp events are regulated by the control system of

an OWT [14]. Therefore, it is crucial to identify the characteristics of ramp events and their impact on the performance and ultimate loads of an OWT.

- **Grid Operator:** To ensure the reliability of the electrical system, a grid operator constantly needs to balance energy supply and demand. Thus, increasing fluctuating wind power penetration to the grid negatively affects the system stability [10]. The short-term power fluctuations (lower than a minute) are beyond the system operator's control, which are regulated by the automatic generation control system of a wind turbine. In other words, long period ramp events of an hour to several hours have a substantial impact on system operation [14]. Moreover, wind power ramps associated with aggregated wind and solar farms of a specific area are more important for a grid operator than ramp events observed in a single wind turbine or a farm [15]. The actual concern is when a ramp event shows an opposite correlation with the demand, i.e., power production is increased, but the demand is low (or vice versa). In such cases, either power is curtailed to keep the voltage below the line rating of the network (supply is higher than demand) or a fast response from other generators is required to fulfil the difference in supply and demand (supply is lower than demand). As long as both vary in a similar direction, i.e., both supply and demand increase or decrease, it could be manageable. However, ramp events affect power systems whose the overall share of wind energy is comparable to the demand [14]. With increasing wind power, predicting large ramps is thus of utmost importance, specifically during the night, when the wind power output has a comparable fraction of supply [16].

- **Energy Traders:** The large unpredicted uncertainties in the wind power output could adversely affect the energy market. During the daytime, a grid operator adjusts demand and supply as per updated information and energy bids. If the error in a ramp forecast significantly lowers the power production from the wind farm, it may impose expensive penalties on energy traders. In short, wind power ramps may have a substantial impact on economics [12, 17]. The time period of interest for energy traders depends on the type of market, day-ahead, hourly, or less. Further details can be found in Pinson et al. [9]

- **Wind farm operator:** A farm operator aims to maximize the revenue and efficiency of a turbine. As described before, the wind power variability affects the energy yield of a wind farm. Based on the power limit imposed by a grid operator on a wind farm, the farm operator decides which turbine's power should be curtailed. A turbine operator tries to reduce such downtimes of OWTs and cut down the maintenance costs, which eventually rely on the intensity of ramp events [2]. Besides, the installation of the energy storage system can mitigate the impact of power fluctuations on the revenue. For its efficient design, wind power ramp events forecasting of a specific turbine cluster as well as the wind farm is vital [15, 18].

1.2. Problem description

Discussions over the influence of wind power ramps on grid stability and energy economics have dominated the research in recent years [10, 12, 14–17, 19]. They are also the governing factors in designing storage systems for wind farms [18]. Thus, many definitions are focused on wind power ramps forecasting [12, 15, 17]. The comprehensive literature studies suggest that research in this area is still evolving, and existing methodologies have not sufficiently considered the smoothing effect of wind farm power fluctuations. Thus, improvements in the proposed wind power ramp definitions are vital.

On the other hand, little research has been conducted to analyse the impact of wind speed (and power) ramps on the ultimate wind turbine loads. The widely used design guidelines from International Electrotechnical Commission (IEC) analyse the ultimate loads that a turbine may experience due to extreme turbulence, shear, or gusts. However, none of the load cases deals with wind speed ramp events. Hannesdóttir et al. [13] performed simulations with representative extreme wind speed ramps. The authors showed loads associated with ramp events exceed the IEC extreme turbulence load case for specific wind speed bins [13]. Nonetheless, the results are still not validated with measurements. Therefore, further research based on real measurements is needed to substantiate the existing findings and to investigate the real impact of ramp events on the ultimate wind turbine loads.

1.3. Research objective and methodology

This report aims to analyze the influence of wind power ramps on offshore wind farms of different sizes. In addition, to the best of our knowledge, the existing literature has not evaluated the effect of wind power and wind speed ramp events on the measured ultimate wind turbine loads. Therefore, the primary research objective is

"the investigation of the impact of wind-induced ramp events on the offshore wind farm power and ultimate wind turbine loads - a measurement-based approach"

It is addressed in the following steps:

1. Detection and categorization of wind power ramps events of two wind farms of different size, by considering the smoothing effect of wind farm power fluctuations.
2. Analysis of impact of wind power and speed ramp events on the maximum wind turbine loads.
3. Validation of Hannesdóttir et al. [13] findings by comparing measured loads associated with extreme fluctuations to simulation results.

1.4. Outline

The structure of the report is as follows:

Chapter 2 gives a theoretical background of offshore wind turbine technology and the origins of ramp events. Chapter 3 summarises the literature studies based on the definitions used to detect ramps and the impact on the ultimate wind turbine loads. Chapter 4 provides information on the available data and arguments on the implemented data filtering techniques. Chapter 5 elaborates on the methodology used to detect and categorise ramp events in two wind farms and summarises the characteristics of the observed ramp events. Chapter 6 validates the simulation results against measurements. Afterwards, Chapter 7 addresses the main objective of the research, i.e. the impact of ramp events on the ultimate wind turbine loads. Finally, Chapter 8 concludes the findings and provides recommendations for the future research scope of this topic.

2

Theoretical Background

The following chapter provides the reader with a theoretical overview of the environmental conditions of offshore wind turbines, their performance and loads. Finally, the possible origins of wind speed and wind power ramp events are briefly covered.

2.1. Introduction to offshore wind turbine technology

An OWT is a complex dynamic mechanical system used to convert wind energy into rotational energy and subsequently into electricity. Its fundamental structural components are illustrated in Figure 2.1.

- **Rotor**: It is a rotating part that usually includes three blades connected to the hub. Its main function is to convert wind energy into rotational energy.
- **Nacelle**: It houses the machinery, such as the drive train, yaw system, pitch system, etc. The rotor and nacelle together are referred to as the rotor nacelle assembly (RNA).

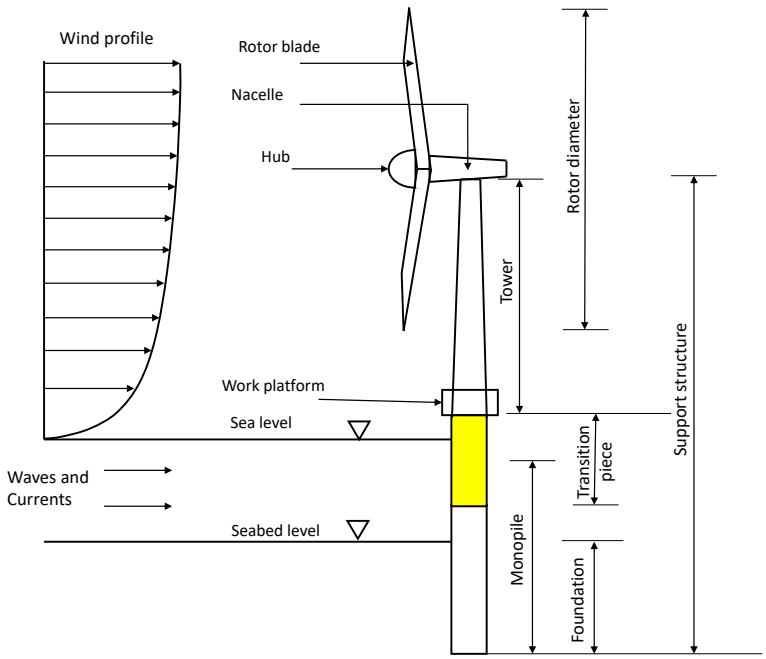

Figure 2.1: The major components of an offshore wind turbine with a monopile foundation.

- **Tower**: It supports the weight of the RNA and the loads induced by environmental conditions.

The height of the tower is decided based on the required altitude above mean sea level for wind power production.

- **Foundation**: It is a fundamental support system that must safely absorb and transfer all the loads to the seabed, simultaneously ensuring the stability of an OWT [3].

  All components from tower to foundation are together known as the support structure.

The surrounding offshore environment affects the performance of an OWT (or wind farm) as well as its loads. Wind turbine designers analyse the effects of such conditions on structural components of an OWT by using intensive simulation tools and following the design guidelines. This section provides further insight on these topics.

2.1.1. Offshore environmental conditions

An OWT encounters dynamic environmental conditions due to changing wind [20, 21], waves [20, 21], currents [21], soil [22], ice (if applicable) [21], and other conditions. The detailed information of these conditions can be found in the above-mentioned references. This work focuses primarily on the effect of wind variability on the power production of wind farms and the loads experienced by the components of an OWT.

In the atmosphere, wind speed and direction fluctuates with different temporal and spatial scales, where small-length scale events are short-lived and larger-scale phenomena last longer. Figure 2.2 summarises the time and horizontal length scales of different meteorological phenomena, which follow a straight line on a log-log plot. Moreover, small-scale weather events occur more often, whereas large-scale events are rare. The wind energy spectrum gives the energy content of various phenomena and the period of their occurrence (see Figure 2.3). Besides, wind speed also varies across height.

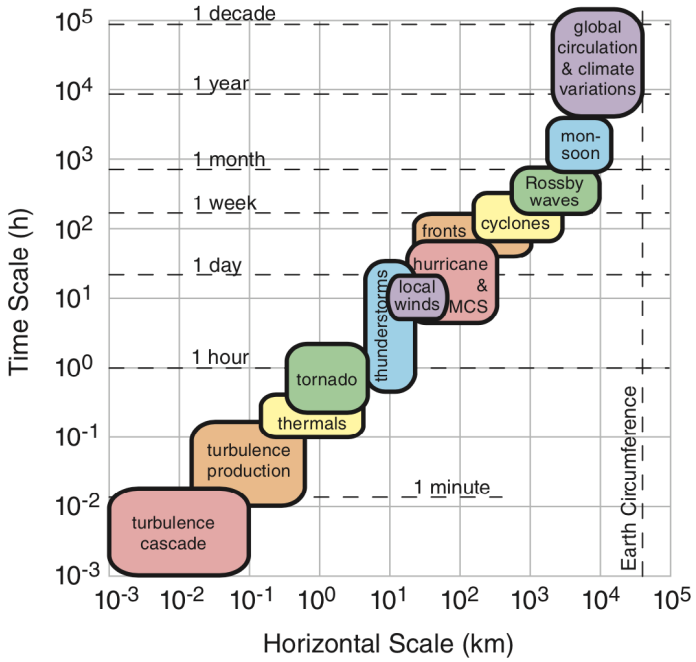

Figure 2.2: Spatial and temporal scales of some meteorological phenomena [23].

Because these conditions vary widely across time and length scales, it is time-consuming and computationally intensive to analyse wind turbines for each of these conditions. Therefore, based on the available measurements, the most common wind statistics are extracted, such as the 10-min mean horizontal wind speed (u) and the standard deviation of the 10-min wind speed time series (horizontal and vertical). Subsequently, the wind time series are synthesised and extrapolated to

represent different normal and extreme environmental conditions. In addition, a vertical wind profile is formulated by using the logarithmic and power laws, whose variation with height is as illustrated in Figure 2.1. Further details and formulas can be found in [24].

Similar to wind, waves conditions also vary at different temporal and spatial scales. They are induced by the friction between wind and water surface, which are also known as wind-induced gravity waves [20]. The energy spectra of ocean waves are shown in Figure 2.4, where the x-axis indicates the frequency or period at which the specific event (peak) occurs. The left side of the graph represents events with long time scales, while the right side represents high-frequency oscillations.

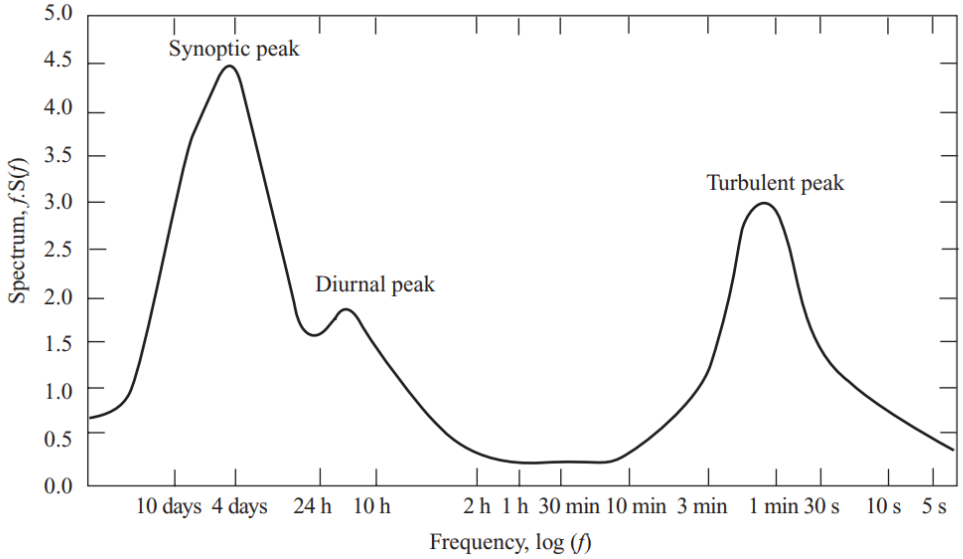

Figure 2.3: Energy spectrum of horizontal wind speed [20].

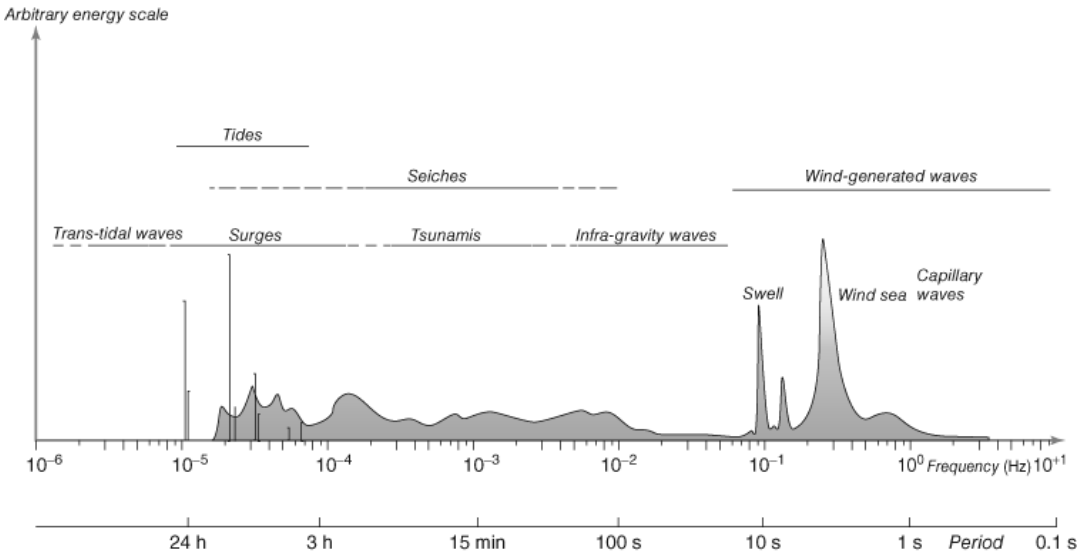

Figure 2.4: Energy spectrum of ocean waves [25].

Depending on the water depth, the foundation type of a turbine is selected. The waves in shallow water are usually modelled linearly by using the Airy wave theory [20], for which a monopile foundation can be used. As the water depth increases, the waves exhibit nonlinear behaviour and increased fatigue loads [26]. It requires a more complex foundation, such as a jacket, to withstand

the loads. Moreover, significant wave height is one of the most important factors for wave loading. It is estimated as the average of the highest one-third of the wave height. For more details on wave loading, [20, 27] can be referred.

2.1.2. Offshore wind turbine and wind farm power

The performance of a turbine is generally estimated based on its energy yield, i.e., power generation over time, which depends, among others, on weather conditions. The variation in power output as a function of horizontal wind speed is illustrated by the power curve of a wind turbine, which is divided into four regions [28] (see Figure 2.5):

- region I is the region below cut-in wind speed, where the turbine is idling.
- region II ranges from cut-in to rated wind speed, i.e., partial load region. Here, the power (P) increases non-linearly with the wind speed ($P \propto u^3$).
- region III covers the area from the rated to cut-out wind speed, i.e., the full load region. Here, power is maintained constant to the rated power within the generator capability [29].
- region IV is the area after cut-out wind speed, where the turbine is parked.

This transition in the power curve over the entire wind speed range is generally facilitated by the generator torque and pitch control. The filtered signal of the generator rotational speed (Ω) is an input to the control system. The signal is low-pass filtered to mitigate the high-frequency excitation of OWT components due to controller activities [30]. The fundamental goals of the controller are [31]:

- to maximize the output power in the region below rated wind speed.
- to maintain rotational speed and power within generator limits at wind speeds above rated wind speed.
- to maintain power output within the power limit imposed by the turbine operator.
- to minimize fatigue and extreme loads on the OWT components.

The structural loads are discussed later in subsection 2.1.3.

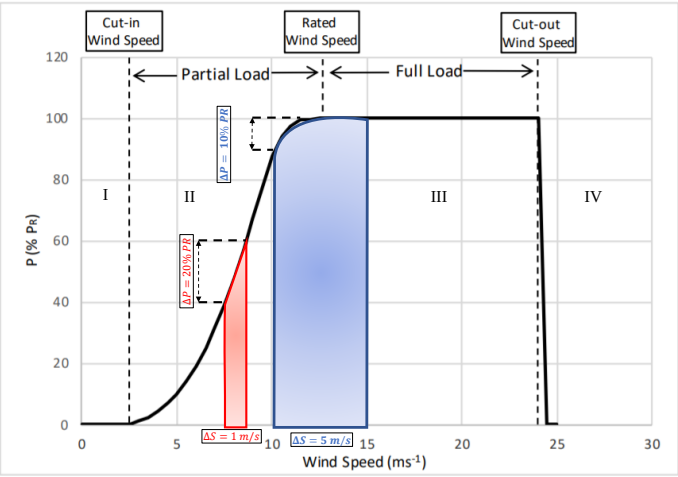

Figure 2.5: An example of a wind turbine power curve. Here, the red and blue contours represent the influence of non-linearity of the power curve at different wind speed regions (modified version of [32]).

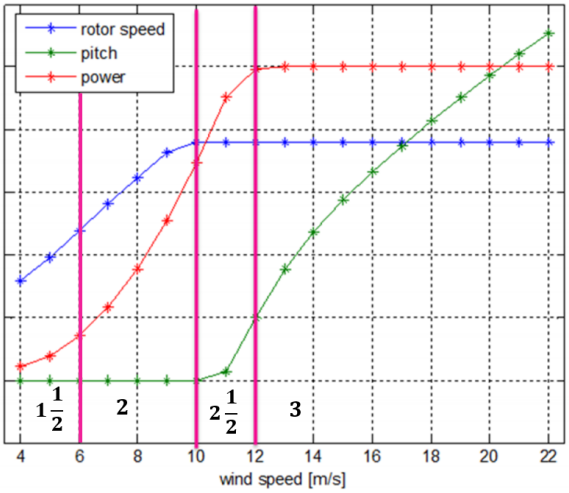

Figure 2.6: An example of the power, pitch, and rotational speed curves for a pitch-regulated wind turbine. The different control regions are indicated by the pink lines [27].

Figure 2.6 shows an example of the functioning of a pitch controller for a pitch-regulated wind turbine. Here, the pitch, rotational speed and power curves are divided according to the variation of a rotational speed. Region $1\frac{1}{2}$ is a start-up region, where the rotational speed (and torque) increases linearly to reach the optimal power coefficient. The region 2 is a partial load region, where the rotor speed varies with the wind speed, and the pitch is inactive. In other words, blade operates at its optimum angle of attack. In this region, the power (P) varies with the third power of the wind speed, i.e. $P \propto u^3$. in the region 3, power is also kept constant at the rated power by increasing the pitch activity. The pitch controller is activated in the region $2\frac{1}{2}$ to keep the rotor speed constant to the rated rotational speed, which is to prevent the rotor speed from exceeding the capability of the generator [29]. It is achieved by pitching the blades to vane (pitch into wind to reduce their surface area) and making linear adjustments in the torque curve. In particular, the angle of attack is decreased (lower than the optimal value), resulting in a decreased lift force and increased drag force. Finally, [27, 30].

Non-linearity of the power curve

Despite the significant wind power resource of offshore sites, fluctuating power output has always been a major challenge for the wind industry, and the non-linear relation between wind and power is a fundamental reason behind it. The intensity of power variations depends on the region in which a wind turbine is operating. For instance, because of the non-linearity in the partial load region, a minor change in wind speed leads to a significant shift in power output. Let us consider the example represented by a red contour in Figure 2.5. For an increase in the wind speed by 1 m/s, the corresponding power output augments by 20% of the rated power (P_R). If such significant power variations occur in a short period, these are known as **wind power ramp events** (see section 2.2). Moreover, the large variation in wind speeds does not necessarily induce significant power fluctuations. An example is represented by a blue contour in Figure 2.5. Here, power changes only by 10% P_R for a 5 m/s change in the wind speed, which is because of the constant power output in region III. On the other hand, in region IV, if the wind speed slightly exceeds the cut-out speed, power drops nearly by 100%. However, the advanced soft cutout technology helps to minimize the abrupt drop in power after cut-out speed [33].

Smoothing effect of power fluctuations

The arrangement of OWTs in a wind farm aims to minimize the wind-induced power fluctuations and increase overall energy yield. Therefore, the knowledge of power fluctuations smoothing effect is important for improving the performance of large wind farms.

When the fluctuations in the power output of individual wind turbines in a wind farm are uncorrelated, they get smoothed out upon aggregation [34]. The individual power variations that are caused by errors in yaw and pitch controllers or in other wind turbine components are usually independent of the rest of the turbines in the wind farm [35]. Moreover, when the wind turbines are far apart, the power fluctuations of spatial and temporal scales lower than the distance between two turbines are also uncorrelated. Therefore, the standard deviation of the fluctuations of the normalized wind farm power time series (σ_{pfn})) is smaller than the standard deviation of the fluctuations of the normalized power time series of an individual wind turbine (σ_{pn}). For a wind farm of N turbines, σ_{pfn} will be $\frac{\sigma_{pn}}{\sqrt{N}}$, i.e. it is decreased by the square root of the total number of turbines in a wind farm (N) [34] (see Appendix B for the comprehensive derivation). In other words, fluctuations diminish on summation, and so do the size of ramp events. An example of power fluctuation smoothing effect is shown in Figure 2.7. When uncorrelated power outputs of turbines T16 and T40 are aggregated, their fluctuations smooth out (black line), i.e. the fluctuations of the aggregated power are smaller than the fluctuations T16.

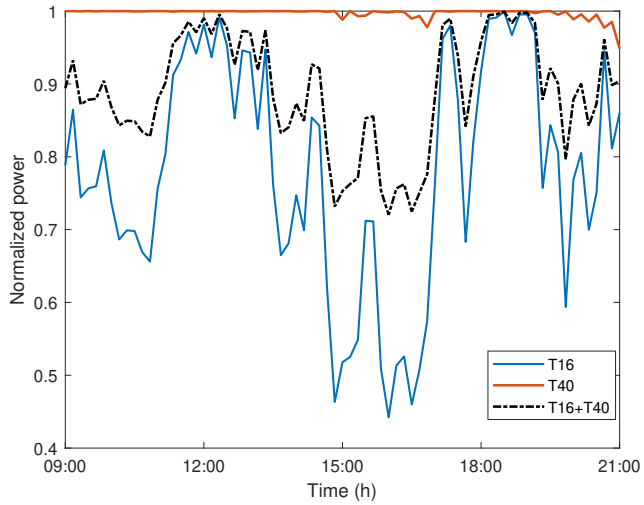

Figure 2.7: An example of smoothing effect of power fluctuations on the aggregated power of wind turbines.

However, in reality, the wakes of upstream wind turbines affect the power output of downstream wind turbines. Thus, based on the wind turbine arrangement in a wind farm and the incoming wind direction, the power fluctuations show some correlations. Wind farm power fluctuations in a row-configured wind farm show high dependency on wind direction, whereas in the square configuration the aggregated farm power fluctuations are independent of the wind direction. For instance, Seifert et al. [35] observed that stream-wise aligned wind turbine pairs show the highest correlation, which decreases towards the span-wise direction. In a square-configured farm, the number of downstream and free-stream turbines are similar for any wind direction. Therefore, wind direction has little influence on wind farm power fluctuations.

As the wake induced turbulence modifies the wind shear profile of a downstream turbine, the correlation between power fluctuations is driven by the spatial distancing between the turbine pairs. Lipman et al. [34] stated that the correlation in the power fluctuations decays exponentially with an increase in spacing in a span-wise direction. This is mainly influenced by the mesoscale weather phenomenon and the dependence of power fluctuations on the wind speed fluctuations below the rated wind speed [35]. Mehrens et al. [36] observed a similar exponential behaviour in the mesoscale wind speeds at different offshore wind farms. This is because the correlation in the spanwise direction is affected by the travel time of the event, which depends on its mean wind speed, wind direction and the spatial distancing between the turbines [35].

2.1.3. Offshore wind turbine loads

"In the design, certification, and optimization of offshore wind turbines, extensive loads simulation is inevitable to develop reliable and cost-effective turbines" [20].

As stated in Vorpahl et al. [20], the turbine must withstand significant loads over its lifetime. Varying environmental conditions, lack of comprehensive offshore site measurements, and computationally intensive models make it difficult to estimate the response of an OWT to the real-time data. Thus, many researchers focused on reproducing representative environmental time series to analyse the influence on the OWT structures. This section gives a general overview of OWT loads, their influencing environmental conditions, and the necessary design guidelines for running load simulations.

For simplification, OWT loads are divided as per the local coordinate system of a specific component. For instance, loads on the blades are divided into flap-wise and edge-wise moments. The direction of the flap-wise moment is perpendicular to the chord length, and the edge-wise motion occurs in the direction parallel to the chord length of an aerofoil (see Figure 2.8(a)). The tower side-side motion, which is induced by the generator torque, occurs around the rotational axis of a rotor. On the other hand, the fore-aft moment is in the direction parallel to the axis of rotation, and is driven by the out-of-plane forces (see Figure 2.8(b). The focus of this thesis lies on the rotor and tower loads.

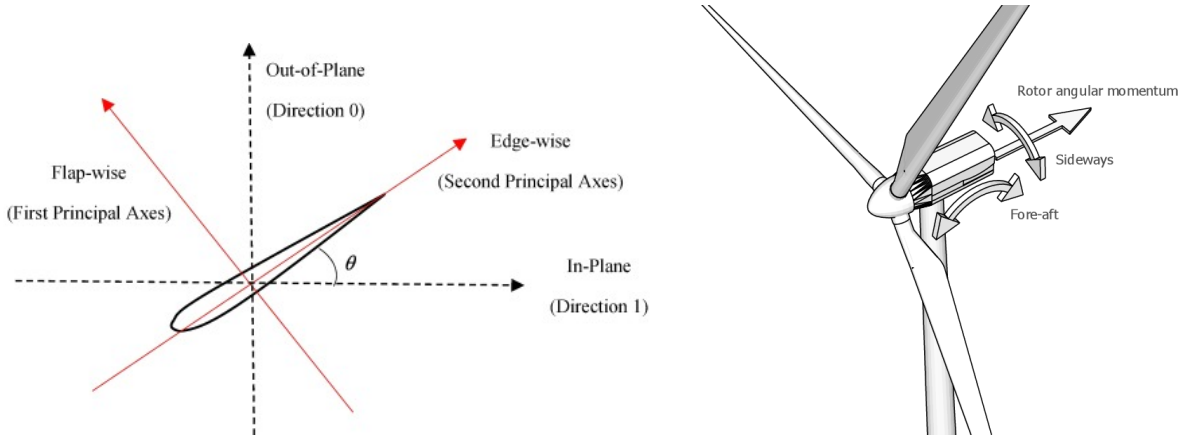

(a) Flap-wise and Edge-wise convention [37]

(b) Fore-aft and Side-side convention [38]

Figure 2.8: Wind turbine (a) blade and (b) tower direction conventions.

An OWT is a complex mechanical system, which experiences static as well as dynamic loads. Depending upon the load-inducing conditions, these loads are briefly classified into the following categories [24]:

- **Gravitational and inertial loads**: due to gravity (self-weight), rotor rotation, structural vibrations, or seismic activity
- **Aerodynamic Loads**: due to airflow interaction with stationary or moving components of the turbine. Therefore, these loads are mainly influenced by the mean wind speed, turbulence, wind shear, controller activity, tower shadow and rotational speed of the rotor.
- **Hydrodynamic Loads**: due to water flow interaction with the support structure. These loads are mainly dependent on the water flow kinematics, water depth, currents, and shape of the support structure.
- **Actuation Loads**: caused by wind turbine operation and control system. For example, loads resulted from mechanical brakes, pitch, yaw, and torque controller activities.
- **Other Loads**: wake loads, impact loads (breaking of waves).

In summary, environmental uncertainties, such as varying wind, wave, current and soil conditions have a substantial influence on the wind turbine loads. This thesis focuses only on the effect of horizontal wind speed variability.

Wind-induced loads

Wind velocity is a primary load governing factor during the operation of an OWT [27]. To understand the effect of wind variability on wind turbine loads, let us first consider the loads induced by the wind speed. The interaction of the wind flow with the turbine rotor mainly gives rise to in-plane force, which is governed by the torque and out-of-plane thrust force. Figure 2.9 illustrates these forces as a function of wind speed. Similar to power, these loads depict a non-linear relation with wind speed. Therefore, wind variability also affects OWT loads. For instance, the torque (τ) is a function of power and rotational speed, which is given as [39]:

$$\tau = \frac{P}{\Omega} \tag{2.1}$$

Since the rotational speed varies linearly with wind speed in the partial load region and is constant afterwards, (see Figure 2.6) the torque curve also shows a similar behaviour to the power curve Figure 2.9(a)). On the other hand, due to the constant power, the thrust force on the rotor decreases after rated wind speed. But, in the partial load region, the thrust force (F_n also increases with u^2 (see Figure 2.9) [39].

$$F_n \propto \frac{P}{u} \tag{2.2}$$

Additionally, the wind also induces a drag force on the tower, which varies across the height as per the wind shear profile.

As explained in subsection 2.1.1, wind speed and direction fluctuates with different temporal and spatial scales. In addition, pitch moment, rotor yawing, yaw misalignment, rotor rotation, tower shadow (i.e., when a blade passes by in front of the tower) and other operations of an OWT modify the wind shear profile and turbulence [27]. The extreme load sensitivity analysis conducted by Robertson et al. [40] disclosed the high sensitivity of the blade loads to these operational conditions. Moreover, as stated in the literature, all significant loads occurred near or above rated wind speeds.

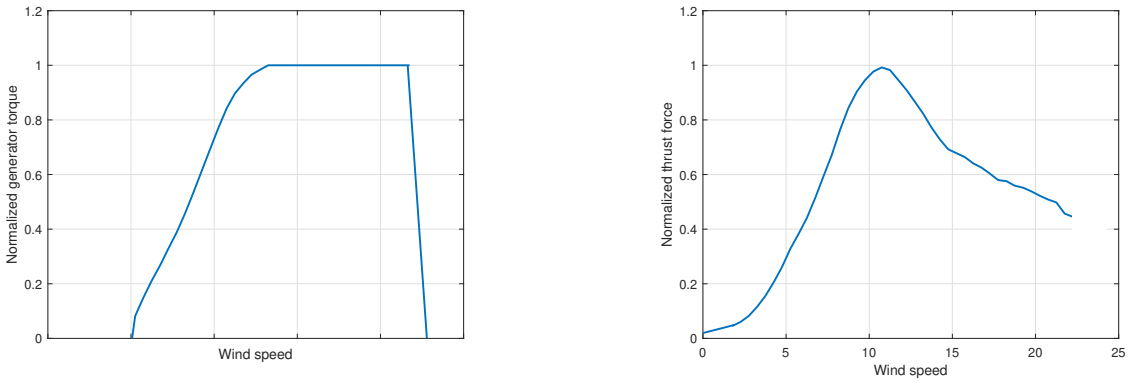

(a) Torque curve

(b) Thrust curve

Figure 2.9: Variation of in generator torque and thrust force with wind speed.

Effect of wind-wave misalignment

The **wind-wave misalignment** is a significant driver of extreme tower loads. Theoretically, a constant long-term wind speed leads to a unidirectional wind and wave alignment. However, in reality, wind speed and direction fluctuate over time, which affects the wind-wave interaction, leading to directional mismatches, and irregular ocean waves [20]. For instance, Fischer et al. [26]

observed the largest effects when the wave direction was perpendicular to the wind direction, i.e, they reported nearly a fivefold increase in a side-side moment compared to only a 30% reduction in the fore-aft moment of the support structure (In Koukoura [27], there is a typo of 30% "higher", which should be 30% "lower"). According to the author, the most probable reason for this could be the first eigenfrequency of the support structure, being closer to the wave peak, led to the very high excitation [26].

Another reason for high side-side moments can be the deceased aerodynamic damping effect, which is explained in Figure 2.10. In this case, the fore-aft motion of the tower is in the opposite direction to the wind velocity. Due to this, the rotor experiences increased relative wind velocity and consequently high thrust force, which counteracts the tower motion. When the tower moves in the same direction as the wind, the resulting aerodynamic force decreases due to the decreased relative wind speed. In other words, the aerodynamic force dampens the fore-aft motion of the tower caused by the hydrodynamic loads. This phenomenon is known as **aerodynamic damping**. The damping effect is maximum when the wind and wave directions are perfectly aligned and reduced otherwise [27].

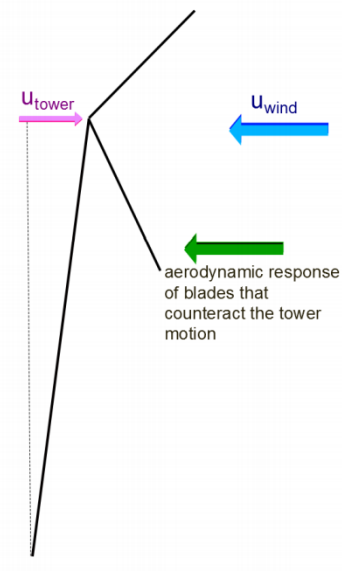

Figure 2.10: Effect of aerodynamic damping on a tower fore-aft moment [27].

IEC design load cases

As discussed in chapter 1, intensive simulations are performed to estimate various loads that an OWT may face during its lifetime. Moreover, varying environmental conditions significantly affect OWT loads. For this purpose, various design guidelines and synthesised wind, wave time series models are available, where IEC standards are widely accepted. The IEC design load cases (DLCs) aim to keep the limit state probability of OWT components below a certain value prescribed by the ISO 2394 standard [24, 41]. The IEC DLCs also follow the certification guidelines, for which the turbine design should at least be verified against the following limit states:

- **Ultimate limit state (ULS)**: Loads should not exceed the maximum load-carrying capacity of the designed structure.
- **Fatigue limit state (FLS)**: The fatigue damage of the structure should not exceed the value of 1. Here, the fatigue damage estimates the accumulated damage of the structure due to cyclic loading and stresses during its service life.

- **Structural instability**: The load-carrying components shall not deform during their service life.
- **Critical deflection**: Deflection of one component shall not mechanically affect the other component. (e.g., a blade should not hit the tower).

The above checks ensure that an OWT is engineered to withstand the potential hazards over its lifetime. Given the uncertainties in wind conditions, a number of time-domain simulations are performed for different seeds representing the different stochastic wind patterns. Additionally, to account for variations in material properties, manufacturing, and measurement errors, the simulation results are multiplied with partial load safety factors to define the limit state. These load safety factors vary depending on turbine components and loading conditions [24, 27].

Following the design criteria and possible loads, the IEC 61400-3 standard prescribes various design load cases (DLCs) [24] based on the operating condition of an OWT. These include power production, power production plus the occurrence of a fault, start-up, normal and emergency shut down, parked, parked plus the occurrence of a fault. Further details on the design conditions, such as relevant wind, wave, wind-wave directionality, can be found in IEC 61400-3 [24].

Since the DLCs of IEC 61400-3 include hydroelastic loads in addition to the aeroelasticity, this can be said as an extension of the IEC 61400-1. The hydroelasticity determines the response of the support structure caused by the interaction between inertial, hydrodynamic and elastic loads. While, aeroelasticity investigates the loads induced by the interaction of the inertial, aerodynamics and elastic forces on the structure.

With the increasing size of OWTs, ultimate loads are becoming increasingly critical. An OWT is subjected to various extreme loading conditions during its operation, which is determined by the statistical extrapolation of loads for 50 years or by synthesising extreme wind time series. When the wind variability is not adequately captured, it may cause an inaccurate representation of the ultimate design loads [2, 20]. The wind conditions that are considered under IEC are normal and extreme turbulence, extreme wind shear, and extreme coherent gusts. An overview of related DLCs during the operation of an OWT includes:

- **DLC 1.1**: It estimates the loads experienced due to the atmospheric turbulence during normal operation conditions. The corresponding statistical turbulence model is based on the standard deviation of the 10-min horizontal wind speed time series (σ_u). The normal turbulence model (NTM) of IEC is representative of 90% quantile of these standard deviations at a given hub height. The estimated extreme loads, at least the blade root moments, are extrapolated for a period of 50 years to identify probable ultimate loads in 50 years.
- **DLC 1.2**: Similar to DLC 1.1, it also estimates the loads due to atmospheric turbulence. However, it is the only operational case which analyses the damage caused by fatigue analysis.
- **DLC 1.3**: It simulates the loads by using the IEC extreme turbulence model (ETM). It is a statistical approach based on the extreme wind fluctuations that a turbine could experience during its operational life. Depending on the site conditions, turbulence models are divided into three classes as per intensity. The simulations are repeated until the extreme loads (at least the blade root moments) are higher than those determined with DLC 1.1. Thus, it could be said that DLC 1.3 is representative of extreme loads resulting from normal as well as extreme turbulence in the 50-year return period.
- **DLC 1.4**: It analyses the extreme coherent gust with direction change (ECD). It is considered as a potentially critical transient condition during the service life of an OWT.
- **DLC 1.5**: It determines the loads caused by an extreme wind shear (EWS). It is also considered a critical transient condition during the service life of an OWT.

Further information related to wave, current, and soil conditions can be found in the IEC 61400-3 standard [24].

In summary, to the best of our knowledge, no load case has been developed to analyse the impact of ramp events on the ultimate wind turbine loads. Therefore, this thesis hereafter focuses only on ramp events.

2.2. Ramp events

As introduced in chapter 1, ramp events are generally manifested as a sudden and significant change in power or wind speed in a short time period (see Figure 1.1).

The definition of short period also varies with the objective. Gallego-Castillo et al. [12] summarised wind power ramp events on a time scale of five minutes to six hours. Cheneka et al. [42] examined ramp events lasting for 15 hours. On the other hand, Hannesdóttir et al. [43] defined wind speed ramp as an event with a temporal and spatial scale greater than turbulence or gust. In this thesis, events that fall under the temporal scale of few minutes (higher than the turbulence time scale) to several hours, and follow spatial scales ranging from a few meters to 100 km are studied.

The knowledge of the ramp direction helps in distinguishing ramp events into ramp-up and ramp-down categories. Ramp-up is defined as a sudden increase in wind power (or speed), which may occur because of intense low-pressure systems (cyclones), low-level jets (LLJs), thunderstorms, wind gusts, and similar weather phenomena. In contrast, ramp-down is a sudden decrease in wind power (or speed), which can result from a slackening of the pressure gradient, the passage of pressure couplets, yaw misalignment, and power curtailment [12, 17, 44].

Understanding the root cause of ramp events is an important precursor for analyzing their influence on end-users and finding solutions to alleviate the impact. This section summarises some of the origins of wind speed and power ramps.

2.2.1. Origin of wind speed ramps

Several atmospheric conditions may lead to the generation of the ramp-like structures. Various literature addressed the generation of a ramp event based on the thermal stability of the boundary layer. For example, in the stable boundary layer, it may originate due to induced turbulence from vertical wind shear of horizontal winds, such as gravity waves, pressure gradient, Kelvin Helmholtz instability, or surface heterogeneity [45]. The development of ramps in the convective boundary is perhaps due to surface buoyancy fluxes, latent heat release, or cloud radiative effects, which are present as convective cells or rolls [46]. In a neutral boundary layer, a ramp may arise because of shear, which is observed as streaks [47].

A few of the underlying phenomena, which are frequently mentioned, are described below:

- **High Turbulence:** The horizontal turbulence intensity measures the velocity fluctuations in the horizontal direction as $\frac{\sigma_u}{u}$, where σ_u and u are the standard deviations and mean wind speed over a 10-minute period at a given height, respectively [32]. Thus, higher turbulence intensity indicates a high standard deviation in 10-min horizontal wind speed is perhaps an indication of a ramp. Hannesdóttir et al. [43] has identified a ramp-like increase in wind speed when an extreme variance event is observed in 10-min wind speed time series. Higher horizontal turbulence intensity could be observed during frontal systems.

  High vertical turbulence intensity also provides the characteristics of large-scale weather events. For example, vertical turbulent mixing is observed in the convective atmosphere (thunderstorms, gravity waves). In a stable atmosphere, coherent turbulent structures are observed just below LLJ [48, 49]. High turbulence can also result from the superposition of the wakes of wind turbines.

- **Frontal Systems:** A front is a transition zone between two interacting air masses, which majorly indicates a strong horizontal gradient in temperature, humidity, wind speed, pressure

and vertical shear. Air mass is a volume of air that generally has constant temperature and humidity. As the pressure at any height in the atmosphere is related to the mass of the air, it is associated with a synoptic-scale system, which is a spatial scale of pressure distribution. In a hydrostatic environment (i.e., no vertical acceleration), the weight of air mass balances a decreasing pressure with increasing height. In Figure 2.11(a), the solid black line represents hydrostatic pressure. However, a column of air in the environment may experience different variations in pressure across the height (non-hydrostatic) that deviate from hydrostatic pressure (dashed curve). If at higher altitudes, this deviation is positive, at lower altitudes, it will be negative. The combination of positive and negative pressure deviations from hydrostatic pressure form pressure couplets. Figure 2.11(a) gives a fundamental overview of the presence of non-hydrostatic pressure couplet in the atmosphere as a function of height and pressure. A rise or fall in the values of these pressure couplets results in a rapid decrease or increase in wind velocity and different air masses[23]. The abrupt changes in air masses give rise to weather fronts, which are also related to a sudden directional shift, precipitation and strong winds [32].

Frontal systems are nothing but the presence of one or more fronts in the environment [23]. The fronts are classified depending upon their characteristics as a cold front or warm front. Figure 2.11(b) shows a symbolic representation of warm front (semi-circle), cold front (triangle) and when they combine, known as occluded fronts.

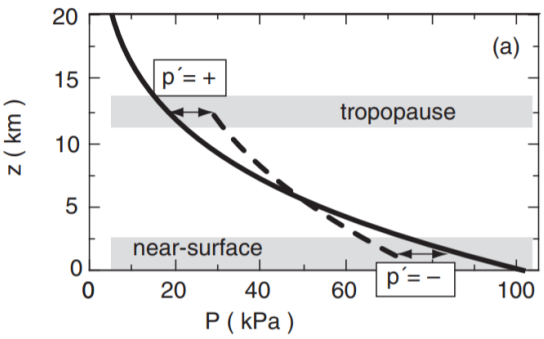

(a) Pressure couplet(solid line - hydrostatic pressure, dashed line - non hydrostatic pressure, p' - pressure deviation) [23]

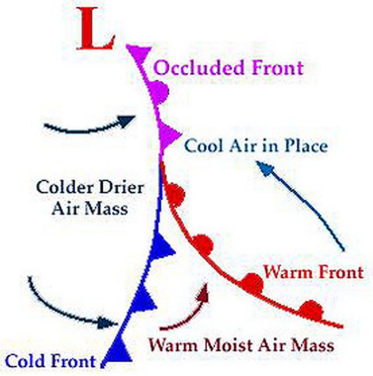

(b) Representation of cold, warm and occluded fronts [50]

Figure 2.11: Illustration of (a) Pressure couplets and (b) frontal system.

Pichault et al. [32] has summarized the front identification technique proposed by Simmonds et al. [51], in two steps: (1) if the sign of the meteorological wind direction changes from positive to negative (e.g. shifts from southwest to northwest) over a successive period of six hours, and (2) if the magnitude of wind speed change is higher than 2 m/s over the same six hours interval, it can be said that a front (or fronts) is present in the atmosphere. Thus, frontal activities give rise to either ramp-up or ramp-down events [32].

- **Convective outflow boundaries (moist convection):** Outflow boundaries are the separating layer between a thunderstorm cold air outflow and a surrounding warm moist air. When a cold air mass advects faster than a warmer air mass, the atmospheric condition becomes unstable, convective, and turbulent. However, a strong stable layer on the top of the air mass acts as a lid to convection. As the cold air from the thunderstorm downbursts, it spreads out in a horizontal direction, and the leading edge of the outflow is known as the gust front [23]. Mostly, these gust fronts lose their energy quickly by giving rise to a new storm, as shown in Figure 2.12.

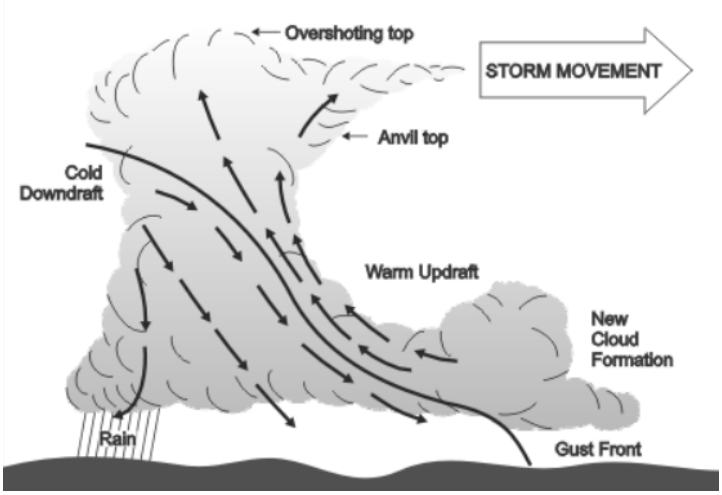

Figure 2.12: Illustration of thunderstorm and gust front [52].

Such gust fronts modify the wind shear profile into an inverted boundary layer profile (also known as nose-shaped profile) [53]. In this profile, the maximum wind speed occurs near the ground and it decreases exponentially upwards.

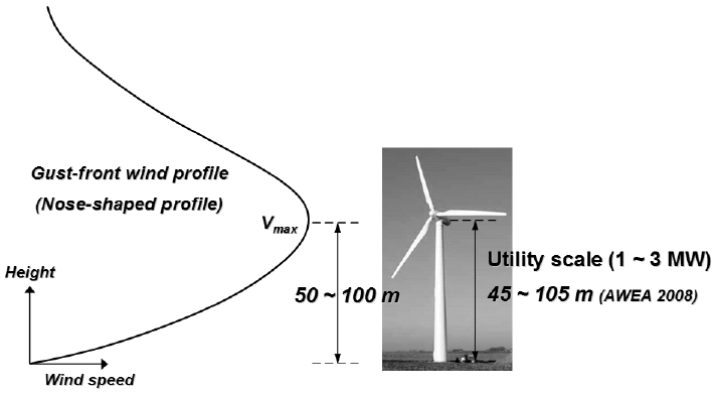

Figure 2.13: Wind profile of a gust front [53].

2.2.2. Origin of power ramps

As stated in subsection 2.1.2, the non-linear relation between wind speed and power output gives rise to power ramp events even for a minor change in the wind speed. Therefore, wind speed ramp events, associated with the partial load region, also induce ramps in the power time series. However, in addition to the weather conditions mentioned in the previous subsection, other conditions could also lead to power ramps. A few of them are as follows:

- **Power curtailment:**
  As discussed before in Chapter1, a grid operator constantly needs to balance supply and demand for the safe functioning of power systems. When the power output of a wind farm is higher than the demand, a grid operator imposes a power limit on its power production, i.e., power is curtailed. This is exemplified in Figure 2.14. Here, the power limit is imposed at 50% of the wind turbine's capacity. As indicated on the right-side figure, a sudden drop in power to 50% results in a ramp-down event.

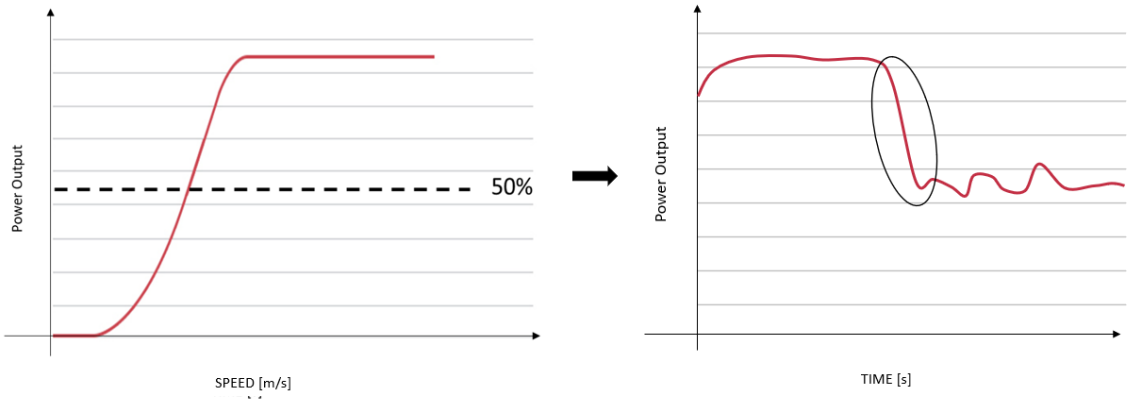

Figure 2.14: An example of a sudden power drop induced by power curtailment of 50%.

- **Yaw misalignment:**
  The yaw controller aims to keep a wind turbine facing towards the incoming wind direction during the power production. The yaw misalignment refers to the condition when a turbine is suddenly misaligned with the wind direction. A sudden shift in wind direction, usually greater than 70◦ leads to yaw misalignment. This usually appears as a dip in the power time series, i.e. ramp down [16].

  Figure 2.15 represents the variation in power for different degrees of yaw misalignment at different wind speed levels. In Cutler et al. [16], the author discovered that the yaw misalignment cases caused by a sudden and large change in wind direction are induced from pre and post-frontal activities.

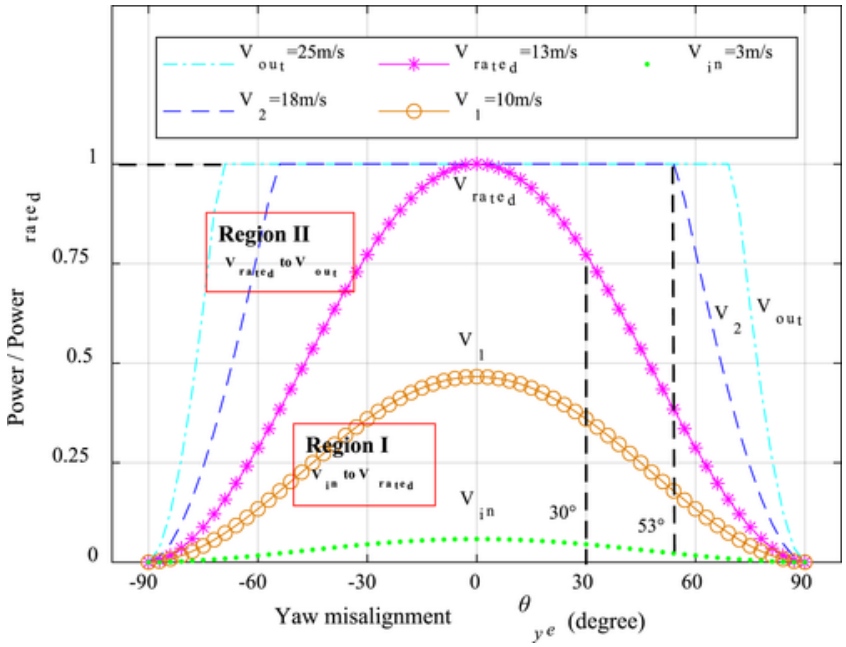

Figure 2.15: Variation of power output with yaw misalignment at different wind speed levels [54].

Effect of local conditions and farm layout on ramp events
Several authors also examined the atmospheric conditions of different offshore wind farms. It is hardly the case that two wind farms experience ramps with similar meteorological conditions. Even for individual wind farms that are located on the same latitude positions, local effects may differ,

such as site-specific terrain properties, roughness, topography, or sea-land interactions [12]. The landmasses and distance of a farm from the coast also influence the mean wind speed and mean wind direction [36]. Therefore, the observed intensities of ramp events vary, even when they are related to large-scale atmospheric processes, which affect neighbouring wind farms. [12].

Moreover, distinct characteristics of weather events, such as temporal and spatial scales, mean wind speed, direction, and stability distribution, also affect the correlation between power output of turbines [34, 35]. Even for large coherent structures, when the streamwise aligned pairs showed high correlations, the correlation in the spanwise direction is affected by the travel time of a ramp event. It depends on the mean wind speed and the spatial distancing between the turbines [35]. Thus, the size of a wind farm also influences ramp events. For example, smaller wind farms with less spatial diversity experienced more ramp events [12].

3

Literature Review

This chapter aims to provide a comprehensive literature review on wind power and wind speed ramp events. Section 3.1 summarises proposed power ramps detection methodologies based on the user-defined input parameters. Section 3.2 presents a study related to the influence of wind speed ramp events on extreme wind turbine loads. On the basis of existing literature, further research scopes are identified (section 3.3) and subsequently, objectives of this thesis are formulated (section 3.4).

3.1. Power ramp events detection methods

As discussed before, power ramp events are generalised as a significant shift in power output in a short period of time. Figure 3.1 illustrates an example of one ramp-up and two ramp-down events observed in the power time series of the Dudgeon wind farm.

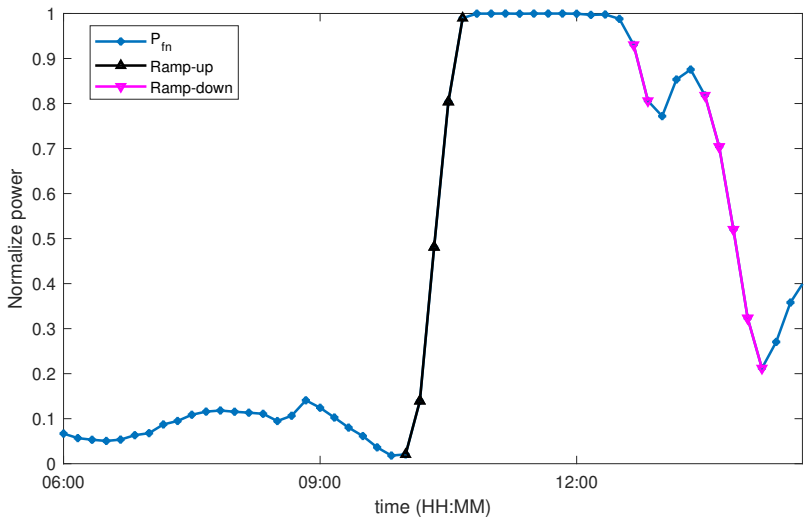

Figure 3.1: Normalized wind farm power time series (P_{fn} in blue) of Dudgeon in February 2018. A ramp-up event is shown by the black lines and two ramps-down events are depicted using the pink lines.

Most of the proposed ramp detection algorithms require some user-defined input parameters, such as the time signal (t), the time window (t_w), the power time series (P), power differences (ΔP), the threshold power value (P_{val}), or the threshold power ramp rate value (PRR_{val}) [12, 15, 19, 44]. For example, Freedman et al. [55] defined ramp event as an event with more than 20% change (threshold) in power output in a 30-min period (time window) as a ramp event. The common outputs of the ramp detection algorithm are ramp direction (ramp up and ramp down), ramp

duration (Δ_t), and ramp amplitude.

Typically, a simple binary indicator function (I) is used to categorize and concatenate co-directional ramp events detected in successive time frames [12]. At first, events are divided into a ramp-up ($I(t)$ = 1), a ramp-down ($I(t)$ = -1), or a no-ramp ($I(t)$ = 0) category, at each time step (seeEquation 3.1). For example, in Figure 3.1 four ramp-up events are concatenated to obtain an overall ramp amplitude. Thus, the time duration (Δt) refers to the rise or fall time of a ramp amplitude. Further implementation of this method can be found in 5.1.5.

$$I(t) = \begin{cases} 1, & \text{if } \Delta P_n(t) \geq P_{val} \\ -1, & \text{if } \Delta P_n(t) \leq -P_{val} \\ 0, & \text{otherwise} \end{cases} \tag{3.1}$$

Here, ΔP_n, P_{val} and PRR_{val} are normalized by the rated capacity of a wind turbine.

The technique used to normalize aggregated power time series (i.e., wind farm power) also influences the detection of ramp events, as the available rated capacity of a wind farm varies over time. These variations could be associated with the upgrading of wind farm capacity, shutdowns, or unavailability of data at different time steps [19]. To address this issue, Kamath [19] used a range of power threshold values to account for power variability. Along the same line, Cutler et al. [16] scaled up the available aggregate power to a wind farm with 37 turbines. The author also set a criterion for the minimum number of wind turbines to be 10. In simple words, time steps of power measurements of fewer than ten wind turbines were discarded. The further justification behind this criterion is not available. On the other hand, Wan [14] normalized the farm power with the total installed capacity of the specific year to consider the influence of the upgrading wind farm capacity.

Several ramp detection methods are summarised in Ferreira et al. [44], Gallego-Castillo et al. [12], and Bianco et al. [15]. In this report, these methods are divided into two parts. The first part reviews the definitions based on the variation of ramp amplitude and duration. The second part deals with the selection criteria used to define the threshold.

3.1.1. On the basis of ramp amplitude and time duration

The basic approach of defining a ramp event is the fixed time interval method. It estimates the power differences between the start and end points of a time window [12, 14–16, 19, 44, 56]. As discussed earlier, the time window (t_w) is a user-defined input that can vary from a sampling time to the total duration of an available time series. Therefore, its analytical selection is essential.

If the power difference in the normalized power time series (P_n) for a defined time window is higher than the threshold value, then a ramp event is identified. Equation 3.2 represents a mathematical formulation of the fixed time interval method.

$$|P_n(t+t_w) - P_n(t)| > P_{val} \tag{3.2}$$

As discussed before, it is possible that the time duration of an event is greater than the length of a time window (see Figure 3.2(a)). Therefore, when the co-directional events are observed in successive time windows, they are concatenated by using the indicator function (see Equation 3.1) to get an overall amplitude and time duration.

Since the above definition only considers the start and end points of a defined time window, events with time duration less than this time window will be missed. This can be observed in Figure 3.2(b), where time window size is much larger than the actual time duration ($t_w > \Delta_t$). In other words, the definition fails to detect true ramp-up and ramp-down events. Besides, the identified ramp (by the orange line) represents a false ramp structure.

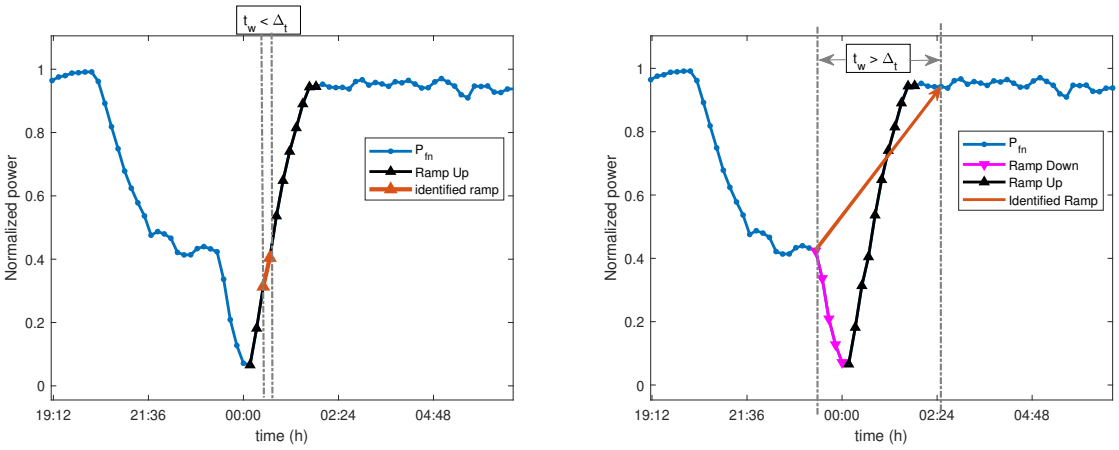

(a) $t_w < \Delta_t$ (b) $t_w > \Delta_t$

Figure 3.2: The fixed time interval method.

To resolve this issue, Kamath [19] presented the min-max method to account for ramps that occurred within the selected time window. As per the definition, when the difference between the minimum and maximum power value is greater than the threshold value, ramps are detected. Further, if the minimum occurs before the maximum, the detected ramp is classified as a ramp-up event, otherwise, as a ramp-down event. This definition (Equation 3.3) gives a maximum ramp amplitude in the sliding time window.

$$max(P_n[t,t+t_w]) - min(P_n[t,t+t_w]) > P_{val} \tag{3.3}$$

However, if other pairs in a specific time window also meet the threshold criteria, only the shortest time duration event is selected [15]. Figure 3.3(a) shows an example of ramp-down event (in pink) that is identified using min-max method. In the selected time window,apart from the minimum and maximum points, adjacent pairs also fulfil the threshold criteria (represented by purple lines). Here, a pair of points with the shortest ramp fall time is identified as a ramp-down event. All the points between the selected pair are marked as a ramp-down (I(t)=-1), and successive ramp events are concatenated.

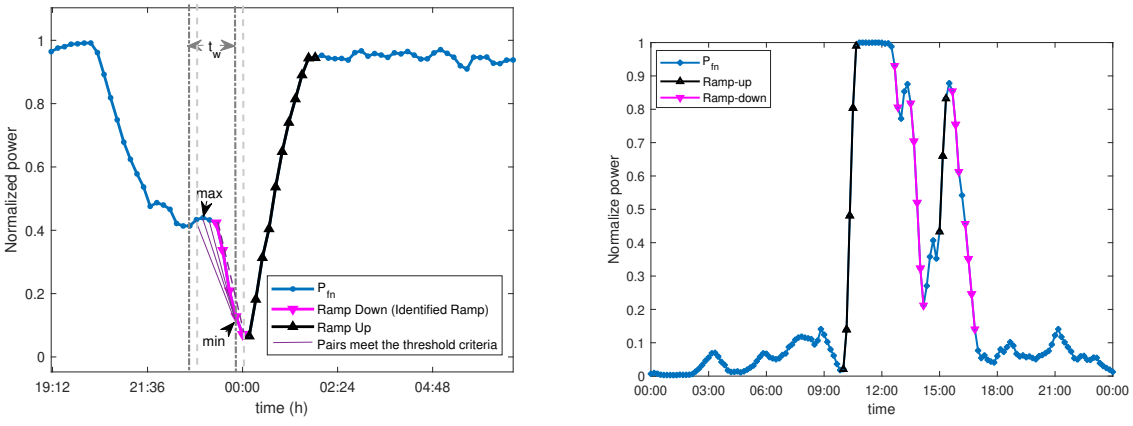

(a) min-max method. (b) ramp rate

Figure 3.3: Examples of ramp detection using (a) min-max method, where grey lines show current time window, and the light grey lines represent the next time step, and (b) ramp rate method.

As the duration of a ramp event can be greater or smaller than the selected time window, the probability of missing out on large intensity ramp events is notable. For example, the impact of a 30% power increase in a 10 minute period is higher than a 50% power increase in a 50 minute interval. Hence, if the threshold is set to 50%, a ramp with a 30% power increase will not be detected.

Therefore, it is important to consider the time factor while defining a ramp event.

Following that, Zheng et al. [57] defined ramp events based on power ramp rate value (PRR_{val}). If the ratio of the absolute power differences to the time interval (k) is greater than PRR_{val}, ramps are detected. For example, in Figure 3.3(b), PRR_{val} is defined considering a 10 minute interval data set.

$$\frac{|P_n(t+k) - P_n(t)|}{k} > PRR_{val} \tag{3.4}$$

On the other hand, high-frequency power signals incorporate noise due to turbulent wind speed. Since the above methods cannot handle the inherent large noise, Bossavy et al. [58] transformed the signal into a first-order derivative by smoothing and differentiating. For smoothing, the author used a linear moving average filter. Subsequently, first-order differences of these fluctuations are estimated by using the following formula:

$$P_t{}^f = mean(P_{t+i} - P_{t+i-n_{am}}; i = 1, ...n_{am}) \tag{3.5}$$

where, $P_t{}^f$ is a transformed signal, n_{am} indicates the number of time steps used for filtering. Thus, ramp event occurs in a given interval if $P_{tn}{}^f > P_{val}$

For better understanding, consider Figure 3.4, where three power signals are represented: an unfiltered one, one transformed with $n_{am} = 2$ and another with $n_{am} = 5$. The threshold P_{val} is taken at 25% of the nominal power. Thus, an event higher than the threshold value is known as a ramp event. The maxima at t = 13 and 32 hours represent the ramp amplitude. Similar to the min-max method, if multiple maxima are observed, the shortest time duration event is selected as a ramp event.

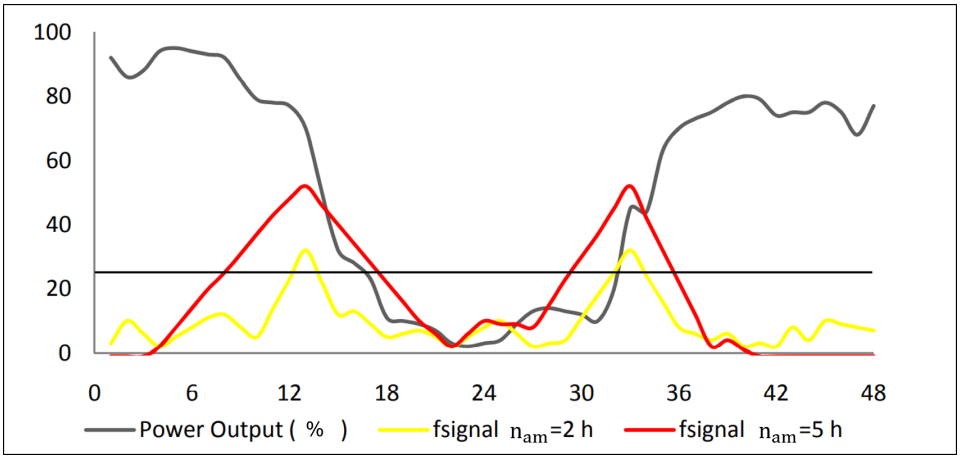

Figure 3.4: Example of wind power output with an unfiltered and two filtered signals. The threshold is taken at 25% of nominal capacity [44].

Nevertheless, as it can be seen from Figure 3.4, the real characteristics of ramp events are lost. Additionally, Gallego et al. [59] argued that the binary ramp classification of ramp events (indicator function) supports the notion that co-directional ramps are of similar characteristics (e.g., ramp amplitude). But ramps with distinct characteristics are usually observed. To overcome this drawback, the so-called ramp function was introduced to characterize the ramp intensity through a continuous-valued index. A wavelet transform method was added with surrogates to discriminate coherent structures from incoherent noise [43, 59]. The continuous wavelet transform (CWT) is continuous in both frequency and time, which is useful to identify and localise abrupt changes in non-stationary time series. Gallego et al. [59] compared the wavelet-based method with the binary indicator function. According to the author, knowledge of the continuous characteristics of ramp events is important for precise forecasting. The literature also highlights additional features of a wavelet transform method, such as preserving information of all ramp events, and their benefits to end-users, along with overcoming the shortcomings of the binary method. Cheneka et al. [60]

summarised that CWT is a useful tool to characterize ramp events. Zhang, Cui, Hodge, Florita, and Freedman [61] used and optimized the swinging door algorithm, where ramp events can be detected without setting any predefined threshold.

3.1.2. On the basis of power threshold values

Gallego-Castillo et al. [12] summarised various literature studies on setting the threshold criteria, which range from 10% to 75% of the rated power. Most commonly, the threshold is specified as a fixed percentage of installed wind farm capacity. However, because of changing nominal capacity (one or more units are turned off or new turbines are installed over time), Kamath [19] argued that the use of a fixed threshold could lead to unreliable results. The authors thus analyzed ramp events for thresholds ranging from 150 to 600 MW. On the other hand, Gan et al. [62] set different threshold criteria, 40% for ramp-up and 30% for ramp-down events.

Moreover, Gallego-Castillo et al. [12] reviewed that only a few authors included the discussion of end-users on the selection of the threshold for the detection of wind power ramp events. In Cutler et al. [16], by noting the different time scales of weather phenomena that have a substantial influence on the Australian Energy Market Operator, the author proposed the thresholds of varying time length (varying ramp rate). At the first stage, the threshold was set to 75% of the rated power to detect ramps within three hours time length using an hourly averaged power signal. Periods of the detected ramp events were removed for the next stage. Subsequently, a threshold was set to 65% for an hour duration, where 10-min average data was used for ramp detection. Aforementioned thresholds, i.e, 75% and 65% were determined using sensitivity analysis. For this analysis, the number of detected ramp events for the range of thresholds range from 40 to 90% with a step of 5% was recorded. As expected, the number of ramp events increased with decreasing threshold values, as represented in Figure 3.5. The sensitivity value was estimated using the Equation 3.6. Ultimately, a threshold with the highest sensitivity value was chosen for ramp detection (here, 75 and 65% respectively).

$$\text{sensitivity} = \frac{n_{th-5} - n_{th}}{n_{th} - n_{th+5}} \tag{3.6}$$

where, n_{th} is the number of ramp events at that threshold. The suffix th denotes the threshold value.

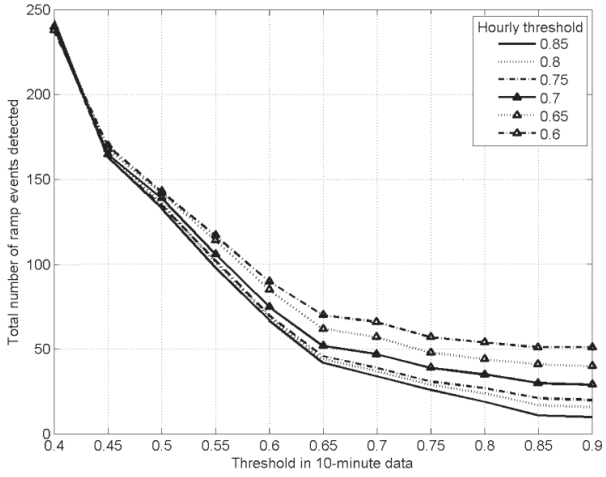

Figure 3.5: Total number of ramp events detected at different thresholds. Each line shows fixed values for stage 1 threshold (hourly data), and the stage 2 threshold (10-min data) on x axis [16].

However, the results from this method are sensitive to the selection of step size. For instance, if a step size value of 2.5% is chosen, it gives a different threshold value due to the different number of ramp events and hence the sensitivity ratio.

Gallego et al. [63] defined the threshold as a $x\sigma(\Delta P)$, where x is a positive real number and $\sigma(\Delta P)$ is a standard deviation of the successive power differences. The authors analysed several values of the threshold for x ranging from 0.2 to 2 with a time step of 0.2. The optimal value of x equals 1 was found suitable for their case study. In Wan [14], the author used a similar method for threshold, where the value of x was set to three, i.e. a 3σ approach. The first-order differences are estimated as

$$\Delta P(t) = P_n(t) - P_n(t-k) \tag{3.7}$$

This methodology gives the overall statistics of these successive power differences of a given power time series. In Valldecabres et al. [17], the authors followed a similar approach and found that the wind farm power differences smoothed out upon aggregation when compared to power differences of individual wind turbines. Therefore, it can be said that this method also considers the smoothing effect of wind farm power differences.

Table 3.1: Summary of literature based on ramp detection methods.

Author	**End User**	**Sample rate**	**Time window**	**Normalization of Wind farm power**	**Minimum turbines**	**Threshold**	**Categorization**
Cutler et al. (2007)	Energy Traders/ Grid Operator	2.5 min	10 min 1 h	Scaled-up aggregated power to installed capacity	10	65-75%PR sensitivity analysis	
Kamath (2009)	Grid operator	5 min	15, 30, 60 min	-	-	10-20%PR	
Gallego et al. (2011)	Energy Traders/ Grid Operator	1 h	1 h	-	-	$x\sigma_g$	Indicator function
Wan (2011)	Grid operator	1 min converted to 10 min 1 h	10 min 1 h	Installed capacity	-	$3\sigma_g$	Indicator function
Gan et al. (2014)	Grid Operator	10 min	-	Installed capacity	-	40%PR - ramp-up 30%PR - ramp-down	
Bianco et al. (2015)	Grid operator flexible for other users	10 min	-	-	-	40%PR	
Hannesdóttir et al. (2019)	Wind turbine designer (loads)	10 Hz	-	-	-	-	CWT

3.2. Impact of wind speed ramp events on ultimate wind turbine loads

Several studies have identified that 10-min horizontal wind speed standard deviations (σ_u) exceed the prescribed IEC ETM, claiming it is not a conservative approach [13, 64]. In addition, these events were found to be associated with wind speed ramps of temporal scales from a few minutes to hours and not with turbulence. Hannesdóttir et al. [13] observed similar events approximately simultaneously at the two met masts, which were 400 m apart, indicating that the length scale is longer than the turbulence scale [13]. Subsequently, the authors examined their impact on the extreme wind turbine loads. This analysis compared simulations from DLC 1.3 based on ETM wind time series and constrained ramp-like wind speed series. As depicted in Figure 3.6, the constrained synthesized time series shows a ramp-like wind speed increase at the middle of the time series, whereas DLC 1.3 time series is a representation of extreme turbulence.

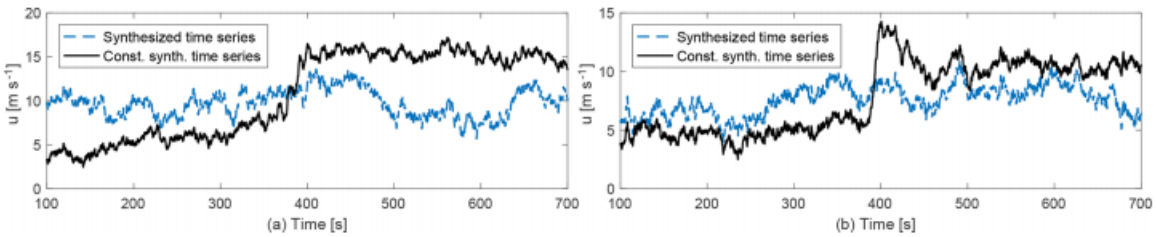

Figure 3.6: synthesised constrained (black) and unconstrained (blue) wind time series [13].

Further comparison between constrained and standard IEC DLC 1.3 simulations revealed that the blade root flap-wise and tower base fore-aft moments exceed the standard IEC DLC 1.3 moments near rated wind speed region. Elsewhere, the extreme loads were observed much lower than the IEC

DLC 1.3 results. According to the author, a relatively large length scale than turbulence led to a coherent increase in the speed throughout the rotor, resulting in increased thrust and thus high flap-wise and tower fore-aft moments.

However, the results are not yet validated with measurements. The simulation model uses the statistical representation of the wind time series, and the aeroelastic tool is simplified based on several assumptions. Hence, a comparison with real measurements is necessary to avoid a too conservative design. To the best of our knowledge, a similar analysis has not yet been performed on the load measurements.

Koukoura [27] has validated DLC 1.1 simulations with measurement data. As the research objective was to develop a good load prediction model, the focus was drawn on the validation with 10-min maximum average measurements and parameter tuning. In addition, the work also deduced that the validation of DLC 1.1 with measured loads is a good first check to identify large discrepancies in the measurements and simulations. Besides, the maximum loads obtained from DLC 1.2 represent the ultimate loads in the normal operation [24]. Therefore, DLC 1.2 can be used as a first check of the aeroelastic model.

3.3. Research scope

In recent years, offshore wind power and wind speed ramp events have received considerable attention in the offshore industry. Although numerous definitions for ramp detection are available, many questions remain unanswered. Some of the identified gaps in the literature are summarised as follows:

- From Table 3.1, for a similar end-user, wind farm power is either normalised by the constant installed capacity or the aggregated available power is scaled up to the total wind turbines in a wind farm. That brings to a question, "How does the power normalisation technique affect the objective of an end-user ?"

- Cutler et al. [16] has specified a minimum number of turbines whose data should be available at each time step to 10. The justification behind the selection criteria is not available in the paper. "What is an effective method for establishing a minimum number of turbine criteria for data availability at each time step, taking into account its influence on the smoothing of wind farm power fluctuations and ramp events?"

- Table 3.1 summarises some of the widely used definitions to identify ramp-like structures, where, to our knowledge, to date, only a few literature studies highlight the impact on wind turbine loads. Moreover, the research was based on simulation studies, and the results have not yet been validated with real-time measurements.

3.4. Research objectives

On the basis of the noticed scope of the research section 3.3, the primary research objective is

"to investigate the impact of wind-induced ramp events on the offshore wind farm power and ultimate wind turbine loads - a measurement-based approach"

It is addressed in the following steps:

1. Detection and categorization of wind power ramp events of two wind farms of different size, while addressing the following research questions:

   - "How does the power normalization technique affect the objective of an end-user ?"

- "How does the criterion of a minimum number of turbines, i.e., data availability at each time step influences the ramp detection method?"

- "How are the characteristics of detected wind power ramp events at two wind farms correlated?"

2. Analysis of the impact of wind power and speed ramp events on the maximum wind turbine loads.
3. Validation of Hannesdóttir et al. [13] findings by comparing measured loads associated with extreme fluctuations to simulation results.

4

Data Description and Filtering

This chapter provides an overview of the local site conditions of the wind farms under study, i.e., Westermost rough (WMR) and Dudgeon wind farms, which are located in the North Sea, UK. The Siemens 6MW pitch-regulated wind turbines are installed in both wind farms. Thus, for this thesis, Siemens Gamesa Renewable Energy (SGRE) has provided the required measurements as well as the simulations datasets. Since various parameters affect the measurement values, data cleaning is vital. Therefore, the adopted filtering techniques are explained at the end of this chapter.

4.1. Site description and measurements

As shown in Figure 4.1, the WMR and Dudgeon wind farms are located approximately 100 km apart from each other. WMR is an offshore wind farm situated roughly 8 km from the Holderness coast, and Dudgeon is located 32 km off the coast of Cromer. Although the Triton Knoll wind farm is between WMR and Dudgeon, it is under construction. On the other hand, wake effects from neighbouring wind farms may influence the power output of the Dudgeon wind farm, especially because of the southwesterly prevailing wind direction (see Figure 4.4). Nevertheless, examining their impact on ramp events is not within the scope of this report.

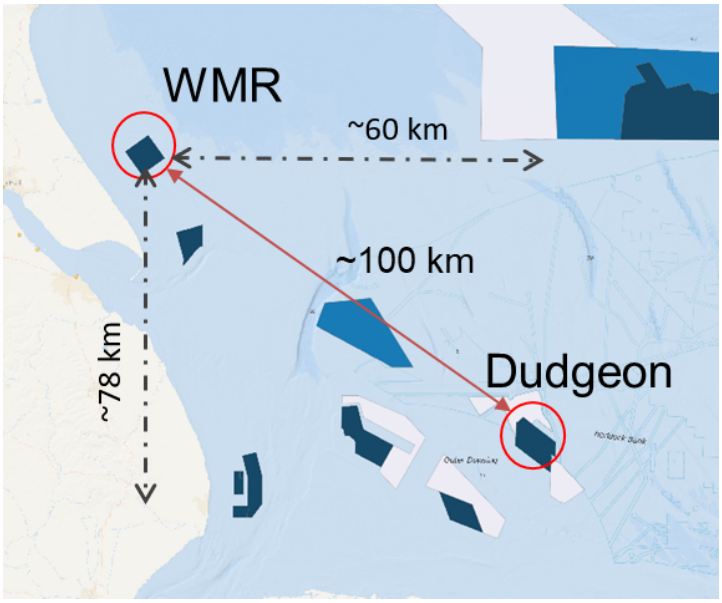

Figure 4.1: Location of WMR and Dudgeon wind farms [65].

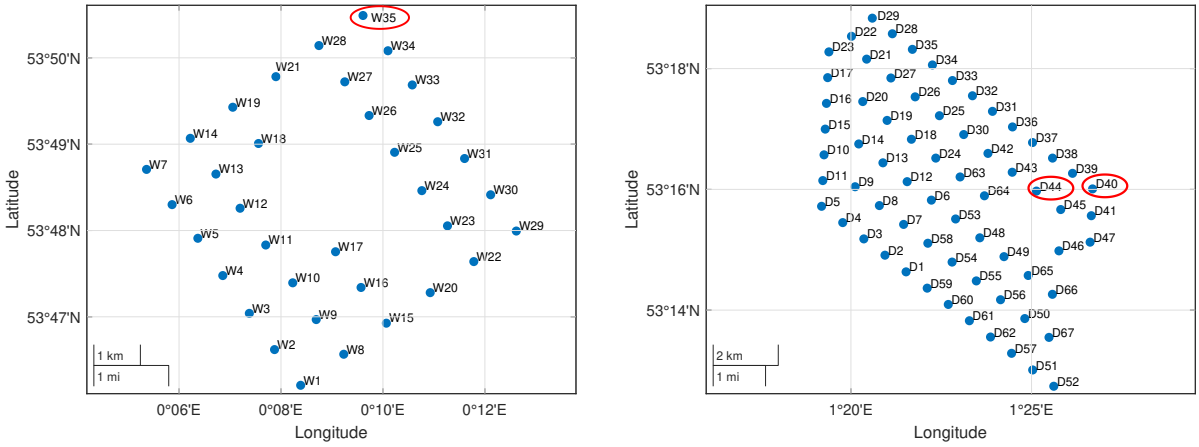

(a) WMR (b) Dudgeon

Figure 4.2: Wind farm layouts of (a) WMR with 35 turbines and (b) Dudgeon with 67 turbines. Turbines highlighted by the red circles are fully instrumented for load measurements.

Both wind farms consist of SWT-6.0-154 pitch-regulated variable speed wind turbines. Their positioning in the corresponding wind farms is shown in Figure 4.2. The additional specifications are provided in Table 4.1. All turbines are equipped with fundamental measuring instruments. For example, cup anemometers are installed for measuring wind speed and wind direction. Besides, the turbine 'W35' in WMR and the turbines 'D40' and 'D44' are fully instrumented turbines, i.e., additional strain gauges are installed for measuring the loads experienced by the OWTs.

Table 4.1: Wind turbine specifications and wind farm information [17, 65].

	WMR	Dudgeon
Number of wind turbines	35	67
Area covered	35 km^2	55 km^2
Wind turbine model	SWT-6.0-154	SWT-6.0-154
Nominal power of an OWT	6 MW	6 MW
Hub Height (msl)	102 m	102 m
Rotor diameter	154 m	154 m

For the detection of wind power ramp events, time series data sets from the Supervisory Control and Data Acquisition (SCADA) system are available. The SCADA system is a computerised system that helps in remotely monitoring and controlling the wind turbines. Typically, it samples the data at a high frequency (nearly 1 Hz) and subsequently stores it on a 10-min basis that can be accessed later [66]. This sampling time may vary depending on the system configuration. Available data signals for this thesis include active power, horizontal wind speed, meteorological wind direction, nacelle side-side and fore-aft accelerations, yaw position, pitch position, active power limit (power limit imposed on individual turbines), and generator rotational speed time series. Each of these time series provides 10-min statistics (average, minimum, maximum, standard deviation values) of the previously mentioned signals at 10-min interval (Figure C.1). Data sets of two years, 2018-2019, are available for detection of ramp events (see section 4.3).

The time series data of individual wind turbines are averaged to analyze the local wind site conditions of the wind farms. The vector averaging method is used for averaging wind directions at each time step. On the other hand, the average horizontal wind speed and turbulence intensity (TI) are estimated using the scalar averaging method. The reasoning and related calculation steps are provided in Appendix A. Following the above approach, both sites show nearly similar average wind speed and wind direction distributions at hub height (see Figures 4.3 and 4.4).

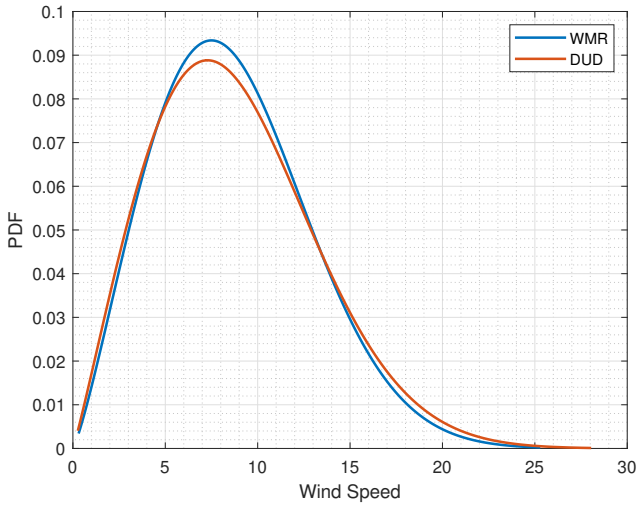

Figure 4.3: Weibull distribution of the average horizontal wind farm wind speeds.

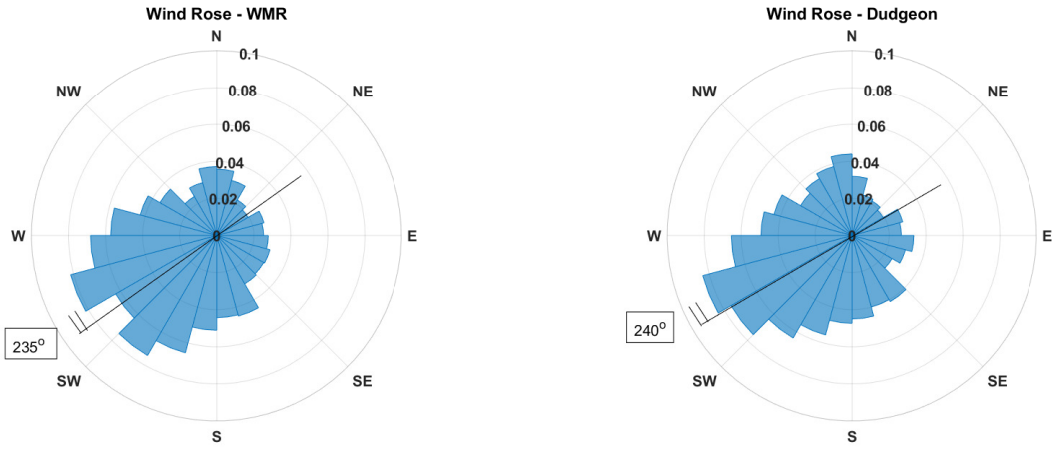

(a) WMR

(b) Dudgeon

Figure 4.4: Wind rose of wind farms WMR and Dudgeon both showing an prevailing west-southwesterly (WSW) wind direction.

Figure 4.5 represents the variation of free-stream TI against the 10-min average wind speed at hub height for turbines W7 and D52, respectively. The free-stream direction of turbine W7 is within the prevailing wind direction. Therefore, it consists of more data points than turbine D52. The selection of the turbine D52 is based on the minimal influence of wake effects from neighbouring wind farms and sufficient data availability of free-stream winds. The comparatively higher average of TI per wind speed bin for W7 is related to the differences in local effects, surface roughness and distance from the coast [67].

The IEC normal turbulence model (NTM) is representative of the 90% quantile of TI measurements observed at the given hub height. Therefore, for comparison with measurements, IEC TI is estimated as $\frac{\sigma_{u90}}{u}$, where σ_{u90} is derived from Equation 4.1 [67].

$$\sigma_{u90} = \frac{u}{\ln \frac{z}{z_0}} + 1.28 * 4 * I_{15} \tag{4.1}$$

where,
σ_{u90} = represens the 90% quantile of the standard deviation of the 10-min horizontal wind speed,

u = 10-min horizontal wind speed at hub height,
z = hub height,
I_{15} = average turbulence intensity at 15 m/s wind speed at hub height,
z_0 = surface roughness parameter estimated from the Charnok equation, which is

$$z_0 = \frac{A_c}{g}\left(\frac{\kappa.u_{hub}}{\ln\frac{z}{z_0}}\right)^2 \tag{4.2}$$

where,
A_c = Charnok's parameter. Its value is taken as 0.011 under the assumption of an open sea condition,
g = acceleration due to gravity, i.e., 9.81 m/s^2,
κ = von Karman's constant, i.e. 0.4,
and z_0 is iterated at each wind speed until its value is identical on the left and right sides (in the DNVGL-ST-0437 [68] standards, the right-hand side z_0 is incorrectly printed as z_o, but they are identical).

The IEC NTM adequately follows the 90% quantile TI measurements before the cut-in wind speed, but afterwards, the measurements show a higher drop followed by an increase in TI in contrast to NTM. The initial decrease in TI at low wind speed could be due to the dominant thermal effects. These thermal effects are suppressed by the increase of the surface roughness parameter, i.e., frictional effects, leading to an increase of TI with increasing wind speed [69]. The discrepancies in TI could also be due to the added blade passing fluctuations. Since the cup anemometer is located behind the rotor, i.e., mounted on the nacelle, its readings are affected by the modified wind speed variability due to the rotation of the rotor. For the three-bladed rotor, the highest fluctuation peak is observed at 3P, indicating three times the rotational frequency. Figure 4.6 illustrates the power spectral density (PSD) plot of the high-frequency (25 Hz) wind speed. The observed peaks at 3P and its multiples indicate the added fluctuations of blade passing frequency. Therefore, it is important to note that the available TI and 10-min average wind speed from SCADA data show some deviation from reality.

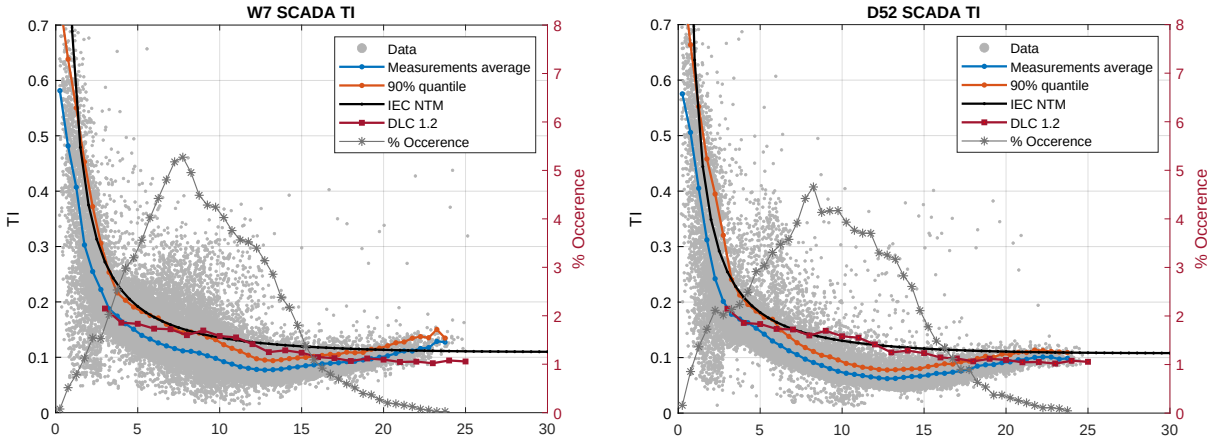

(a) WMR (b) Dudgeon

Figure 4.5: Free stream turbulence intensity at turbines (a) W7 of WMR and (b) D52 of Dudgeon.

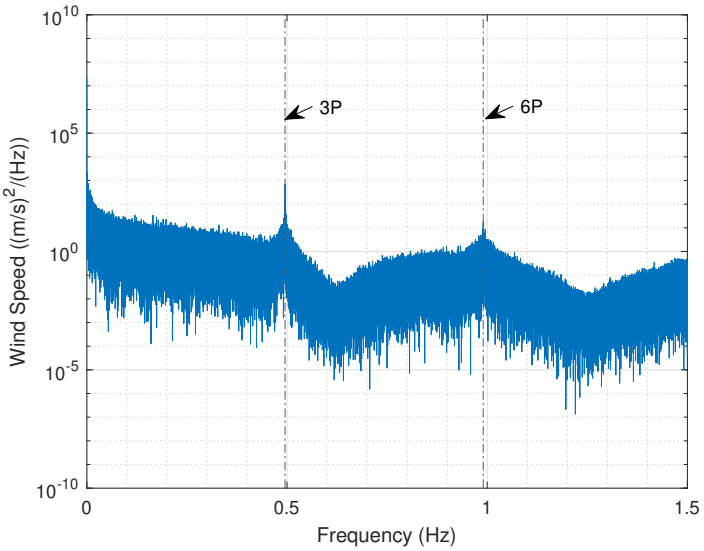

Figure 4.6: Wind speed peaks at 3P and its multiples are induced by blade passing fluctuations.

4.2. Load measurements

For this thesis, the calibrated 10-min statistics and high-frequency (25 Hz) data of the blade root, tower top and tower base moments of a 6 MW pitch-regulated turbine are provided by SGRE, from the Power Load Measurement (PLM) system. PLM acquires load sensor data even under extreme testing conditions. As mentioned in section 4.1, these load sensors are only installed on the turbines W35, D40, and D44 (see Figure 4.2).

The bending moments were obtained from strain gauge readings, which have been calibrated at the sensor locations. Their locations are represented in Figure 4.7. As the blade sensors are placed at edge-wise and flap-wise locations and rotate with the blade while pitching, no more transformations are required in the calibrated moments. However, tower sensors are fixed as the tower. Therefore, the yawing of the wind turbine keeps changing the fore-aft and side-side axes. These moments can be transformed to fore-aft and side-side direction using a simple trigonometric relations given in Equation 4.3 and 4.4 [27].

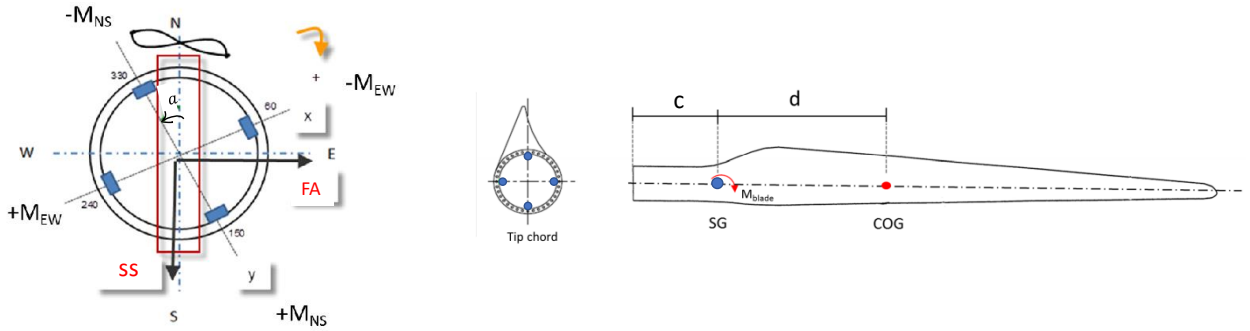

(a) Strain gauge locations for measuring tower bending strains. (b) Strain gauge locations for measuring blade root bending and influence of blade weight .

Figure 4.7: Load measuring sensors location at tower top (or base) and blade root [27].

$$M_{FA} = M_x \cos(a-\psi) - M_y \sin(a-\psi) \tag{4.3}$$

$$M_{SS} = M_x \sin(a-\psi) + M_y \cos(a-\psi) \tag{4.4}$$

where, a is an angle between the sensor location and north direction. Moments M_x and M_y are calibrated at sensor locations (see Figure 4.7(a)), which are used to calculate pure fore-aft (M_{FA}) and side-side (M_{SS}) moments w.r.t. the yaw position (ψ) of the turbine.

Figure 4.8 illustrates the local coordinate system of the tower and blade bending moments. With reference to the turbine positioning shown in Figure 4.8(a), the positive fore-aft moment is considered in a clockwise direction around the x-axis of tower (i.e., x_t in figure), which is in the direction of the thrust force. The side-side moments are positive in the direction of the turbine rotation, i.e., clockwise around the y-axis of the tower (i.e., y_t in figure). However, the blade flap-wise and edge-wise moments are considered positive in the direction opposite to the thrust and tangential forces, respectively. The misaligned axes of forces and moments in Figure 4.8(b), denote that the chord length is not perfectly aligned with the plane of rotation, but it shows some inclination.

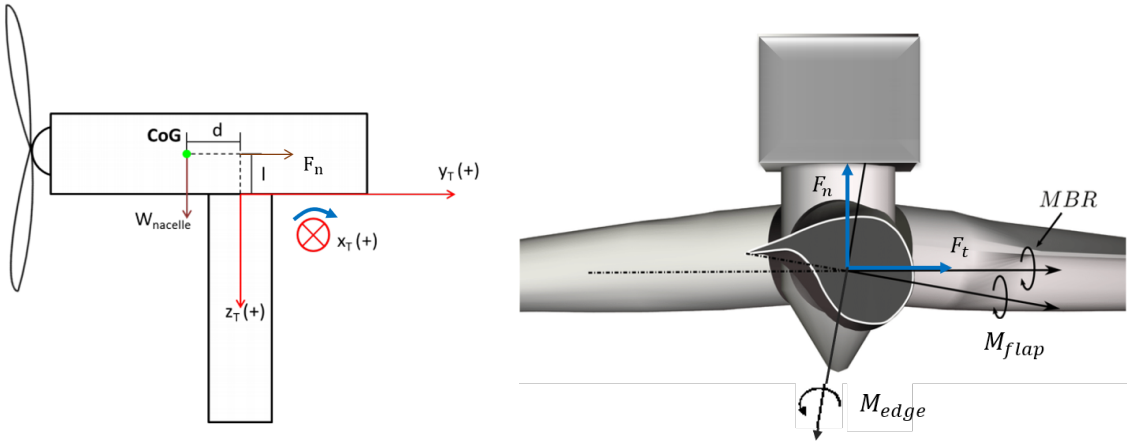

(a) Tower Coordinate system [27]

(b) Blade Coordinate system (modified version of [70])

Figure 4.8: Local coordinate systems of wind turbine tower and blades.

Thus, negative moments denote that the direction of the structural response is opposite to the local coordinate system of that component. For example, a negative tower fore-aft moment indicates that the tower is leaning forward due to the gravity effect in the opposite direction to the thrust force.

4.3. Measurement data availability

The time span of available datasets from different channels are summarised in Figure 4.9. The 10-min SCADA data of all turbines of the two wind farms are available from January 2018 to December 2019. However, the PLM data for turbine W35 is not available at the mentioned period (i.e., 2018-2019). In addition, due to the calibration uncertainty in the available data (before 2017), the W35 turbine is not considered for the ultimate load analysis. Besides, due to brevity, the available blade and tower moments are investigated only for turbine D40.

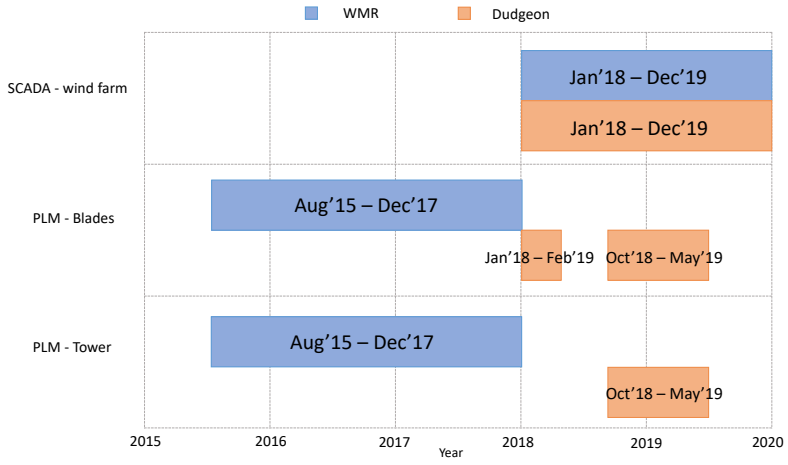

Figure 4.9: Data availability from different channels.

4.4. Simulation data

SGRE simulates the bending moments of OWTs by using the Bonus energy Horizontal axis wind turbine Code (BHawC). It is a non-linear aeroelastic tool used for dynamic analysis and load calculations of horizontal axis wind turbines. For this study, simulations were performed by tuning the structural parameters of the aeroelastic model with the calibrated sensor readings of the turbine D40 from the Dudgeon wind farm (for example, using measured damping coefficient). Moreover, bending moments were simulated at the sections corresponding to the sensor locations on the actual wind turbine, i.e., near the blade root, tower top, and tower base.

As discussed in chapter 3, DLC 1.2 is a good initial check to examine any discrepancies between the model and the measurements. On the other hand, ultimate DLC 1.3 results are required to verify whether the extreme fluctuation events exceed IEC DLC 1.3.

Simulation environment

DLC 1.2: Simulations were performed for six turbulent seeds per wind speed bin indicating six different wind time series with nearly similar statistical values. The average of these values per wind speed bin is indicated in Figure 4.5. The time series had a sampling frequency of 25 Hz and were a duration of 10 minutes, based on the NTM model. For this study, the wind and wave directions were assumed to be perfectly aligned, i.e., 0^o misalignment. Simulations were performed for a single significant wave height using the normal current model (NCM), for the wind speed ranging from cut-in to cut-out in the interval of 1 m/s. Further information is available in the IEC 61400-3 standard [24].

DLC 1.3: The simulations were performed for nine turbulent seeds per wind speed bin, indicating nine different wind time series with nearly similar statistical values and based on the ETM model. The time series had a sampling frequency of 25 Hz and were a duration of 10 minutes. For this study, the wind and wave directions were assumed to be perfectly aligned, i.e., 0^o wind-wave offset. Simulations were performed for a single significant wave height using the normal current model (NCM), for the wind speed ranging from cut-in to cut-out in the interval of 1 m/s. Further information is available in the IEC 61400-3 standard [24].

All analyses of this report are performed in MATLAB 2020b.

4.5. Measured data filtering

Before post-processing the data, filtering out abnormal values is crucial to minimize the possibility of detecting false ramp events and drawing any false conclusions. This section elaborates on the techniques used to filter measured power (subsection 4.5.1) and bending moments (subsection 4.5.2) time series.

4.5.1. Power filtering

The wind power output of each turbine is first normalized w.r.t. the nominal capacity of a turbine to obtain comparable results. Because of the confidentiality of the data, operational wind speeds are not displayed here. To conduct the wind power filtering, the power curve is divided into four regions, as explained before in Figure 2.5

Adhering to the fundamental aim of detecting wind-induced power ramp events, data points other than the normal operational condition are rejected, i.e., when

- the power output is negative
- the power output is limited by a grid operator
- a turbine is shut down in the operational wind speed region (perhaps under maintenance or system fault.)
- the power output is observed at a wind speed higher than the cut-out wind speed

Such data points are visible in an unfiltered power curve, as it is shown in Figure 4.10(a).

Next, negative power output values below cut-in wind speed are taken as 0. It ensures that ramp events starting from (or ending at) the idling condition are not omitted. Further, the normalized power values during the power boost (i.e., power is higher than the nominal capacity) are assigned as 1. Subsequently, the data points of region III are replaced by

$$p_n(t) = \frac{p_n(t)}{P_{limit}(t)} \tag{4.5}$$

Here, P_{limit} denotes a power limit imposed by a grid operator, and in case of power curtailment, P_{limit}<PR. In Equation 4.5, it is assumed that a turbine would have produced the rated power if power was not curtailed. Moreover, this step ensures that the time series has sufficient data points while rejecting only power abnormalities. Because the maximum power output in II is less than the rated power, a similar approach can not be used in that region.

Hereafter, the 'method of bins' is implemented, as described in IEC 61400-12-1, to fit the power curve to the measured data (Figure 4.10(d)). According to this method, the power curve of a single turbine is first divided into wind speed bins of 0.5 m/s and average power is estimated at each wind speed bin. Subsequently, the most representative quantiles are determined per wind speed bins, based on the scattered power in region II. Eventually, the power values lower than the 3% quantile are replaced by Not a Number (NaN). In region III, all power values below 0.98 are replaced by NaN. This power filtering algorithm is summarized using the pictorial flowchart shown in Figure 4.10.

This filtering procedure is repeated to filter the power curve of all other turbines in the two wind farms. Once the power data of all turbines are filtered, inconsistencies within the data points are removed. Here, the inconsistency refers to the missing power values, which could be related to the system downtime for a particular wind turbine. The interpolation method may not generate reliable results when values are unavailable for hours, days, or even months. Therefore, all missing values are filled with NaN.

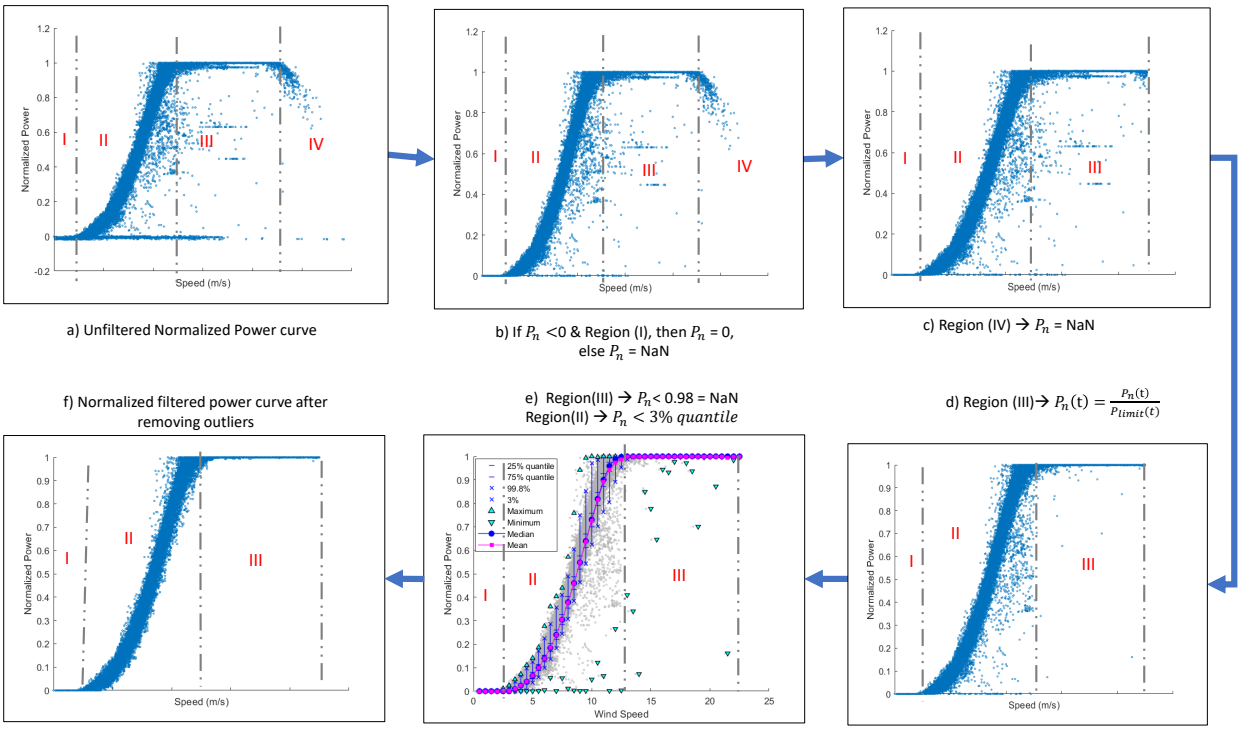

Figure 4.10: Flow chart of power filtering method with an example of turbine D40 of the Dudgeon wind farm. Power is normalized with the rated power.

4.5.2. Load filtering

Figures 4.11 and 4.13 illustrate the stepwise filtering approach used for the blade and tower moments, respectively, for turbine D40. Following the objective of analysing ultimate loads for ramp events, the filtering is performed for 10-min minimum blade moment and 10-min maximum tower moments. The selection of minimum or maximum moments is based on the local coordinate system of the components (see Figure 4.8) in the direction of thrust or tangential force. The moments are first normalized by the absolute maximum (or minimum) moment at the rated wind speed obtained from DLC 1.2 simulations. Moreover, all moments are filtered out when the turbine is not producing power. The filtering steps differ hereafter for blade and tower moments depending on the data availability and the possible causes of errors in the data set.

For blades, the higher (lower in absolute terms) bending moments that deviate from normal behaviour are predominantly related to power curtailment. Since the pitch activity controls power curtailments and load variations, 10-min minimum pitch angles are used to filter the minimum blade root moments. The theoretical operation of pitch control is explained in Figure 2.6. However, in reality, a highly fluctuating wind speed signal compared to the low-frequency response of a controller is responsible for the scatter of the minimum pitch angle in the region 3 (see Figure 4.12). Besides, the 10-min minimum pitch angles (θ_{min}) are plotted against the 10-min average wind speeds, which may not be the actual wind speed at that time step. All of the above uncertainties result in a significant scatter, as it can be seen in the minimum pitch angle plot, from the region $2\frac{1}{2}$ (see Figure 4.12).

Therefore, values above the 99% quantile, i.e., the extreme 1% (θ_{min}) per wind speed bin (for wind speed higher than S m/s) are replaced by NaN. Note that the 99% quantile worked well for turbine D40 but may not be a sufficient constraint for other turbines. It is because the power curtailment data set and the associated pitch responses vary from turbine to turbine. As the tower moments were not available for the corresponding months, this filter was not implemented. It is worth noting that this filter is not necessary for the analysis of ultimate loads since higher pitch values (θ_{min}) than the optimum correspond to higher (lower in the absolute terms) blade bending moments.

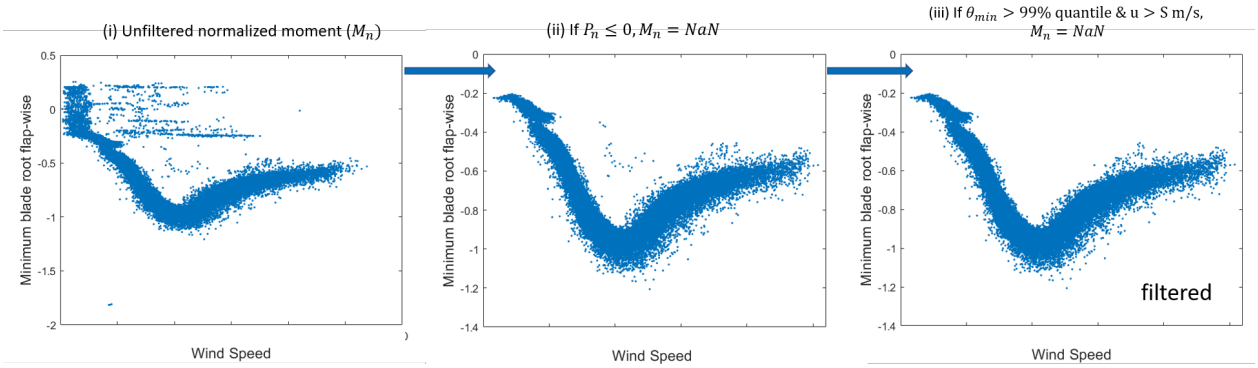

Figure 4.11: Flow chart for filtering blade root moments. Here, the blade root flap-wise moment is normalized with the minimum DLC 1.2 moment at the rated wind speed.

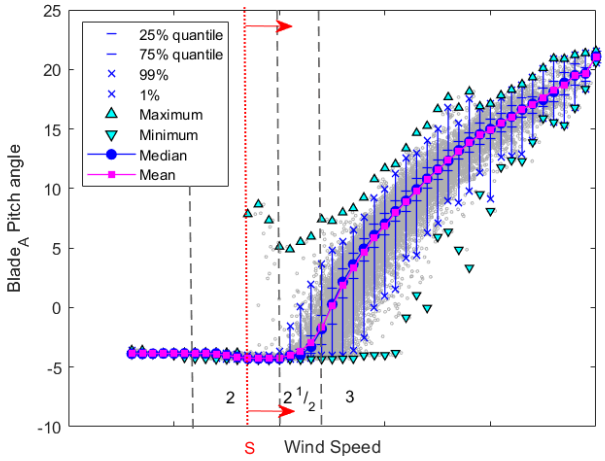

Figure 4.12: Quantiles of 10-min minimum pitch angle against 10-min average wind speed.

Since **the tower** fore-aft and side-side moments are function of a yaw angle (equations 4.3 and 4.4), any error in the yaw angles would also introduce errors in the tower moments. Therefore, filtering is required. Analysis of the high-frequency time series revealed that the highest tower side-side moments (with an order of magnitude equivalent to fore-aft moments), occurred when the yaw angle (ψ) changed by more than 45^o in a period of only 40 ms. As the response time of a yaw controller is much higher, such a fast transition is not possible. Thus, if the difference between the 10-min maximum yaw value (ψ_{max}) and the 10-min minimum yaw value (ψ_{min}) was greater than 45^o, this was considered an error in the data. One could be argue that a higher 10-min algebraic difference in $\psi_{max} - \psi_{min}$ does not necessarily imply a shift in the yaw angle, especially when the turbine is oriented towards the north (e.g., change from 359 to 0). However, the analysis of the high-frequency data showed errors in such situations.

Let us consider an example of Figure 4.14, which depicts the high-frequency time series of tower base moments and yaw angle with a sampling time of 40 ms. The moments are normalized by the corresponding maximum moment of DLC 1.2 at the rated wind speed. As highlighted in the red rectangle, when the turbine was facing north, it yawed by 60^o in 40 ms. At the same time, a sudden spike was observed in the side-side moment and a dip in the fore-aft moment. Thus, when the algebraic difference between the 10-min maximum and minimum yaw angles is greater than 45^o, the corresponding tower moments are replaced by NaN. Such yaw error data accounted for about 0.8% of the available filtered data.

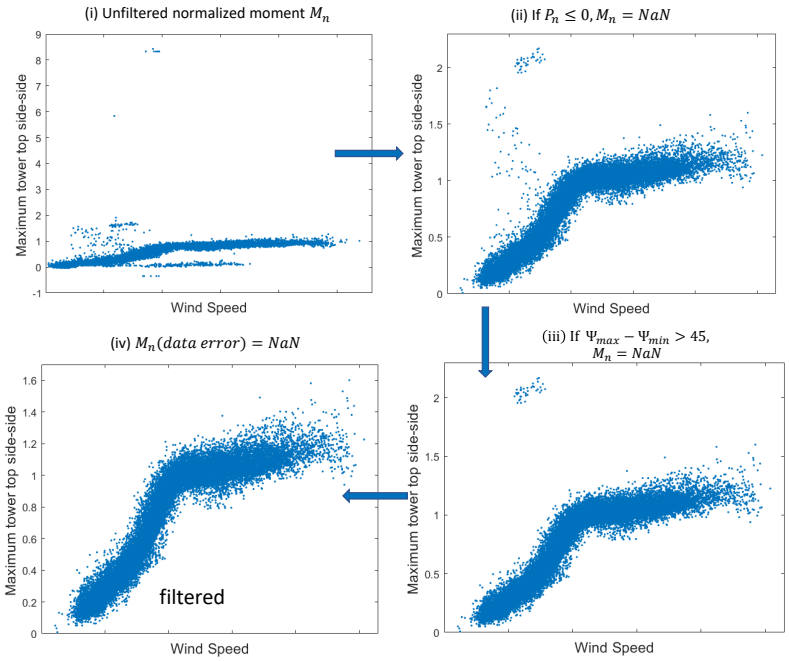

Figure 4.13: Flow chart for filtering tower top and base moments. Here, all moments are normalized with the maximum DLC 1.2 moment at the rated wind speed.

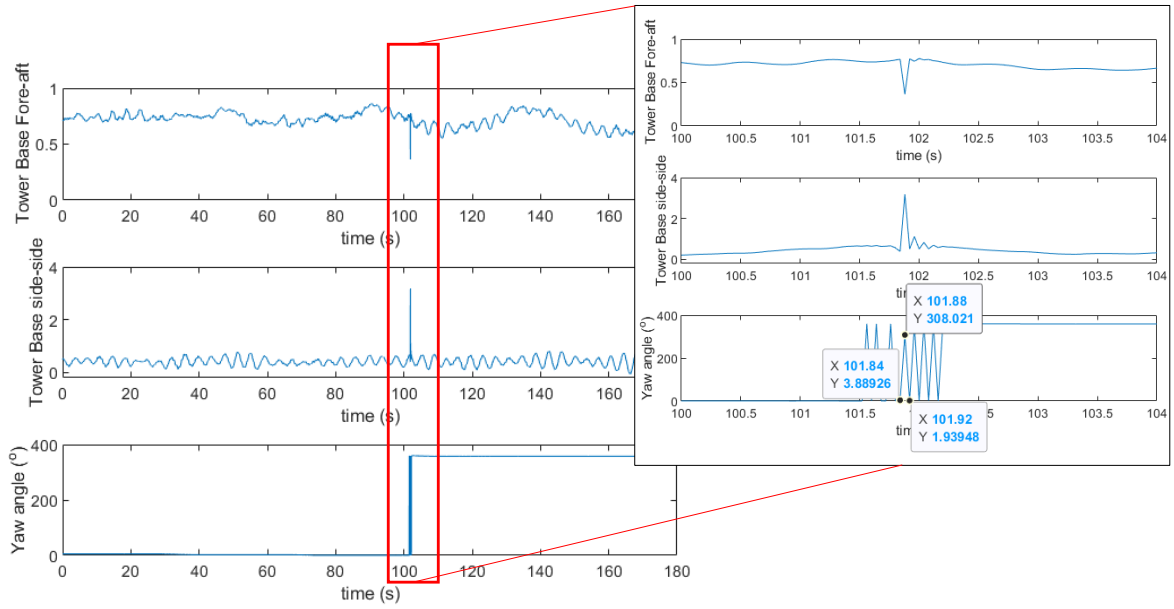

Figure 4.14: An example of significant yaw error inducing a peak in a tower base side-side moment and a dip in a fore-aft moment. Moments are normalized with the maximum DLC 1.2 moment at the rated wind speed.

In addition, a cluster of higher moments (see Figure 4.13(iii)) was observed in the tower side-side moments around the yaw angle of $200^o - 300^o$. Such data points belong to an average of 0.2% of the available filtered data and are also replaced by NaN.

5

Offshore Wind Power Ramps: Detection and Categorization

This chapter aims to provide an insight into the characteristics of the detected ramp events of the WMR and Dudgeon wind farms, and their correlations. In this regard, a suitable ramp detection method is selected by considering the end-user's objective of identifying extreme wind-induced power ramp events. Therefore, this chapter addresses the first research objective in the following three sections:

1. **Ramp detection algorithm:** Firstly, the arguments on the selection of a specific ramp detection method are presented. Secondly, the influence of a technique used to normalize the aggregated wind farm power on the end-users is discussed. Afterwards, attention is drawn towards the effect of power fluctuation smoothing on the threshold and the significance of setting up a criterion of a minimum number of turbines at each time step. Finally, the detection algorithm is presented in combination with the indicator function.

2. **Correlation analysis:** This section examines statistical relationship between wind power, wind speed, wind direction and horizontal turbulence intensity (TI). Furthermore, the correlations and time difference between a few of the large-scale wind power ramp events of two wind farms are investigated.

3. **Categorization of ramp events:** The variation in the number of ramp-up and ramp-down events with regards to change in wind speed, wind direction, turbulence intensity, and ramp duration is reviewed.

5.1. Ramp Detection Algorithm

In this section, the suitable ramp detection method is selected from the reviewed literature in section 3.1. The related arguments are given in subsection 5.1.1. In the next stage, an explanation for the adopted wind farm power normalization technique based on the end-user's objective is provided (subsection 5.1.2). The subsequent subsections focus on the power fluctuation smoothing effect and the criterion of minimum number of turbines' data availability (see subsection 5.1.3). Finally, all criteria are combined with the indicator function to develop a ramp detection algorithm (see subsection 5.1.5).

5.1.1. Definition of a ramp event

As mentioned in section 3.1, there are several ways of detecting ramp events. Yet, the selection of a specific method depends on the characteristics of the available data sets as well as the end-user's objectives. For example, CWT can be an effective tool for high-frequency data, as it can represent the

continuous characteristics of ramp events in the presence of high incoherent noise. This information could be effective for small-scale ramp forecasting (or similar objectives). However, for this report, the data set is available at 10-min intervals. In addition, this thesis aims to investigate the impact of ramp events on wind farm performance and OWT loads, which are also available on a 10-min basis. Therefore, the definition proposed by Wan (see Equation 5.1) is found as a suitable approach for this research.

$$\Delta P_{fn} > 3\sigma(\Delta P_{fn}) \tag{5.1}$$

where, ΔP_{fn} is the successive power differences of the normalized wind farm power. The adopted power normalization technique is explained later in subsection 5.1.2. Moreover, as the threshold $3\sigma(\Delta P_{fn})$ is derived from the statistical properties of the normalized wind farm power, the estimated threshold also includes the smoothing effect of wind farm power differences.

One could argue that the available minimum and maximum values of the 10-min period can also be used to detect the ramps within 10-min intervals. However, because the corresponding time data of these values are unavailable, ramp events cannot be categorised into a ramp-up or a ramp-down category. Additionally, as mentioned in subsection 3.1.1, the difference between minimum and maximum values not necessarily provides a ramp magnitude but may involves the probability of detecting false ramps within that 10-min interval. For better understanding, let us consider two of the possible scenarios presented in Figure 5.1, which illustrates the normalized power time series at two consecutive 10-min periods, t and $t+k$. Here, the 10-min period of the first time step extends from $t - \frac{k}{2}$ to $t + \frac{k}{2}$, where, k is 10 minutes. The dots indicate the power values within 10-min power time series. The red and yellow dots show the maximum and minimum values, respectively, of the specific period. The 10-min average, minimum and maximum power values are assigned to time t. Therefore, as argued, a possible ramp in each 10-min period can be identified as

$$max\_i(t) - min\_i(t) > P_{val} \tag{5.2}$$

From Figure 5.1(a), let us assume that the ramps are identified in each of the successive 10-min intervals. However, because of the unavailability of the respective time data, whether a minimum power event occurred before or after a maximum power event is unknown. Therefore, it is not possible to categorize these events as a ramp up or a ramp down. As a result, successive co-directional ramp events cannot be concatenated to estimate the real ramp amplitude and its duration. On the other hand, in Figure 5.1(b), the detected ramp events, of amplitudes max_1 - min_1 and max_2 - min_2, are not the true ramp events. Therefore, ramp detection by using the minimum and maximum power values of the 10-min interval, leads to the false ramp detection within that 10-min interval.

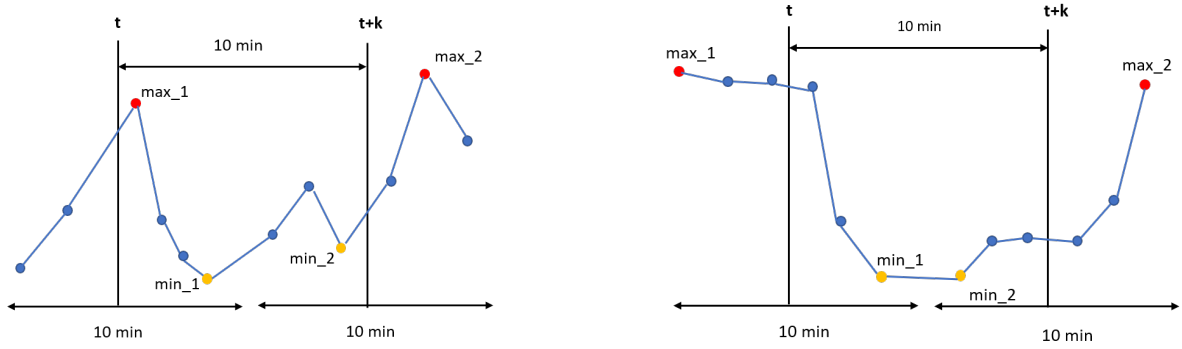

(a) Scenario 1

(b) Scenario 2

Figure 5.1: Examples of power time series for two consecutive period. Blue dots represent the power values. Red and yellow dot highlight the maximum and minimum values in each 10-min time series.

Therefore, only 10-min average power values are used to define wind induced power ramp events. Therefore, it is possible to distinguish between ramp-up and ramp-down periods for a 10-min sample

rate. Moreover, as the Equation 5.1 deals with successive 10-min power data, it does not lead to the detection od ramp events.

5.1.2. Normalization methods

As discussed in chapter 3, there are two possible approaches to normalize the wind farm power (P_f). In this report, they are designated as the variable capacity and the nominal capacity methods.

- **Variable capacity method:** As the name suggests, the aggregated power output is normalized with different capacities at each time step. This eliminates the effect of data unavailability (after filtering) of a few turbines at different time steps. Therefore, in this method, power is normalized by the aggregated nominal power of the available turbines at each time step, which is given as:

$$P_{fn}(t) = \frac{\sum_{i=1}^{N} P_i(t)}{\sum \text{Available wind turbines' capacity(t)}} \tag{5.3}$$

- **Nominal capacity method:** In this method, the aggregated power time series is normalized by the installed capacity of a wind farm. Thus, P_{fn} is calculated using the following equation,

$$P_{fn}(t) = \frac{\sum_{i=1}^{N} P_i(t)}{\text{Nominal farm capacity}} \tag{5.4}$$

Figure 5.2 represents the difference in the normalized wind farm power curve concerning the above power normalization methods.

The suitability of these methods depends on the objectives of end users. For instance, from the perspective of a grid operator, the operator constantly needs to balance supply and demand. Thus, its interest lies in the variation of total wind farm power output, irrespective of its cause. In contrast, wind turbine designer is concerned with the effect of environmental uncertainties on the power output. For a better understanding of its applicability, let us assume a wind farm with 50 turbines. At a time t, all 50 wind turbines are producing nominal power. Later, at time $t+k$ data of 25 turbines is not available, and there is no change in wind speed from t to $t+k$. Thus, now only 25 wind turbines are operating at their nominal capacity. In this case, the normalized wind farm power can be calculated using equations 5.3 and 5.4 as 1 and 0.5, respectively. Therefore, the change in power equals 0.5, when the nominal capacity method is used. This would be useful information for a grid operator, as a 50% drop in overall supply needs to be balanced. On the other hand, because of the constant weather conditions, normalized wind farm power ($\Delta P_{fn} = 0$) did not change with the variable capacity method.

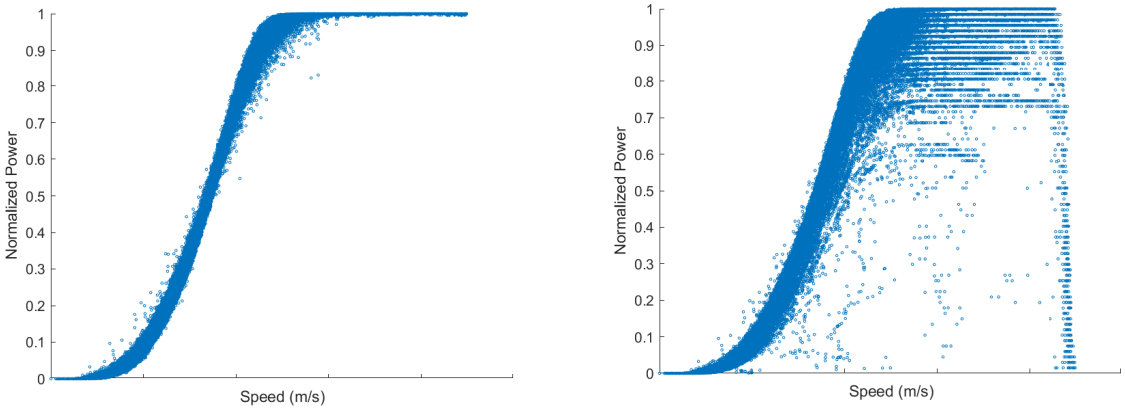

(a) The variable capacity method.

(b) The nominal capacity method.

Figure 5.2: Normalized power of the Dudgeon wind farm by using (a) the variable capacity method and (b) the nominal capacity method.

In summary, when power is normalized using the variable capacity method, the change in the power output is calculated w.r.t the available number of turbines at each time step. On the other hand, the nominal capacity method also considers the effect of wind turbine's availability at each time step. As the objective of this report is to detect extreme wind-induced power ramp events, the variable capacity method is used.

5.1.3. Influence of power differences smoothing on the ramp event threshold

Smoothing of successive power differences

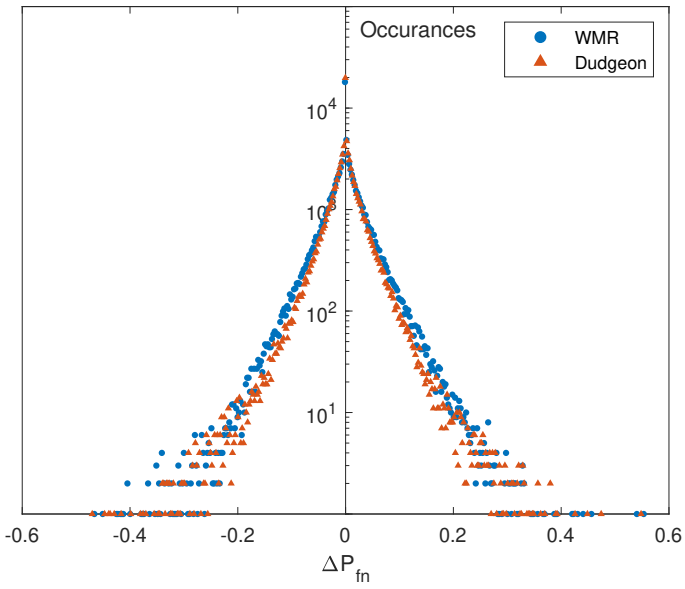

Figure 5.3: Frequency distribution of normalized wind farm power differences of WMR and Dudgeon.

The frequency distribution of successive power differences of the normalized wind farm power can be visualised in Figure 5.3. Both wind farms show a similar distribution pattern. Yet, the magnitude of power differences of the Dudgeon wind farm is slightly smaller than WMR. Therefore, the standard deviation and the threshold value of the Dudgeon wind farm are also smaller. In this case, the thresholds are 13% and 11% of the available capacity for WMR and Dudgeon, respectively.

The reasoning for different thresholds can be the smoothing effect on the power differences. As discussed, the threshold value P_{val} is based on the standard deviation of successive wind farm power differences (3σ method), which is also a measure of their smoothing effect similar to what is observed with power fluctuations (see Appendix B). Moreover, as mentioned earlier in subsection 2.1.2, the intensity of the smoothing effect depends on the wind farm layout, local site conditions, inflow conditions (free or wake), the spanwise distance, and the spatial and temporal scales of the meteorological events [35]. Nonetheless, the influence of a number of wind turbines have not been discussed so far.

Threshold variation with a minimum number of turbines criteria

Figure 5.4 illustrates the behaviour of the threshold ($3\sigma(\Delta P_{fn})$) value with the increasing percentage of data availability, i.e., a decreasing number of turbines. These graphs also compare the aforementioned power normalization methods, i.e. the nominal and the variable capacity method (see subsection 5.1.2). The numbers on the graphs, for example, value '33' in Figure 5.4(a), represents the minimum number of turbines, whose data is available at each time step. For 33 turbines, the time steps with data availability of fewer than 33 turbines are rejected. Therefore, the percentage of

data availability increases with decreasing criterion of the minimum number of turbines.

Although both power normalization methods show nearly similar thresholds, their magnitudes will be the percentage of the installed capacity and the available capacity for the nominal and variable capacity methods, respectively, at each time step. Moreover, a general decrease in the percentage of the threshold value with an increasing number of turbines may imply that the smoothing effect of power differences is lower when fewer turbines are aggregated.

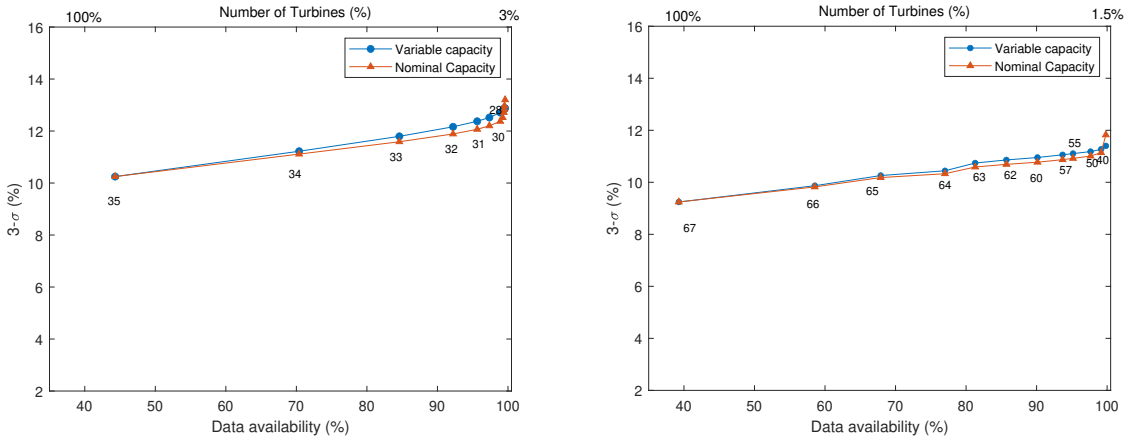

(a) WMR

(b) Dudgeon

Figure 5.4: Variation of threshold with minimum number of turbines criteria using the variable and nominal capacity methods.

However, a significant variation in the threshold values is observed when plotted against the exact number of available turbines (see Figure 5.5). In this case, the x-axis represents the percentage of time periods when the data of the specified number of turbines is available. For instance, value 33 represents the time periods only associated with the data availability of the exact 33 number of wind turbines. Thus, the summation of the fraction of these time periods is nearly 1 (due to the filtered power signals, it will be less than 1). Considering the sufficient time periods, i.e. higher than 5%, the threshold values increase with the decreasing number of turbines, for WMR. On the other hand, for the Dudgeon wind farm, the values first increase and then fluctuate with the decreasing number of turbines (see Figure 5.5(b)). Moreover, the associated increase in the values is not gradual but the thresholds show notable differences. This varying behaviour can also be related to the fraction of time periods for specified turbines. As available fraction of time periods are similar for 64 and 65 turbines of the Dudgeon wind farm (where threshold fluctuates), whereas a notable difference is observed from 67 to 66 turbines (threshold gradually increase).

Therefore, availability of time periods and positioning (inter-turbine spacing) of wind turbines in the wind farm strongly contribute towards the smoothing effect of normalized wind farm power differences than the number of wind turbines. The effect of positioning of wind turbines in a wind farm can be explained from Figure 5.6. Here, the x-axis indicates the selected number of turbines (q) from a wind farm of 35 or 67 turbines. The power signals of these selected turbines are first aggregated, normalized (variable capacity method), and then the standard deviation of successive power differences time series is determined. These standard deviations are shown on the y-axis. The scattered values of the standard deviations (blue '+') indicate the possible number of combinations of selected q turbines in the wind farm of 35 or 67 turbines. The red circles denote the average of these standard deviations.

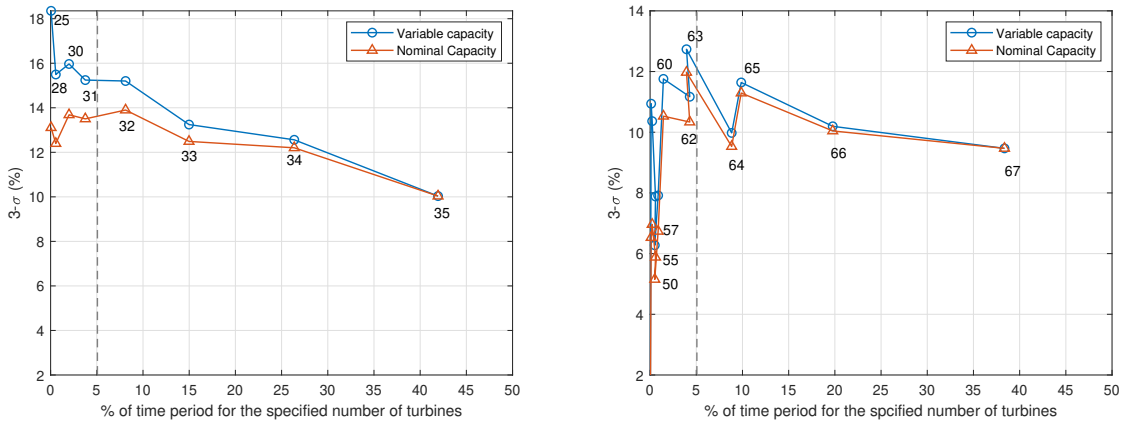

(a) WMR (b) Dudgeon

Figure 5.5: Variation of threshold with exact number of turbines criteria using the variable and nominal capacity methods.

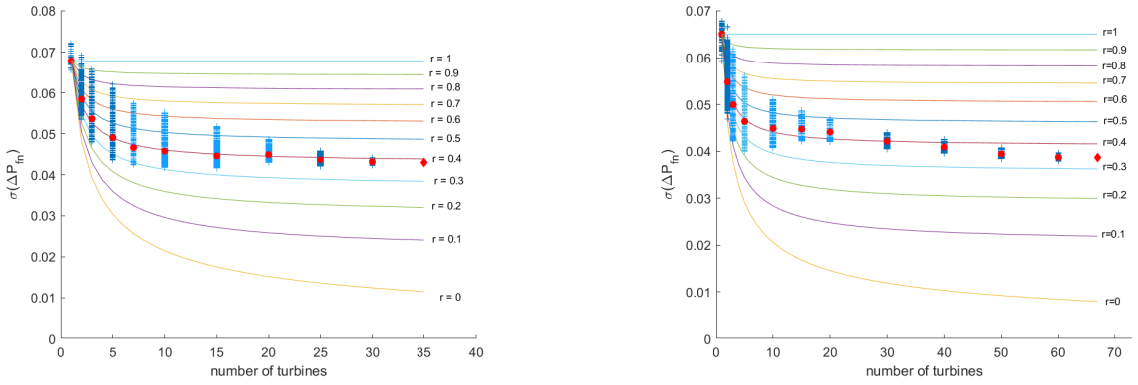

(a) WMR (b) Dudgeon

Figure 5.6: Variation in standard deviations and linear correlation coefficient (lines from r =0 to r =1) with increase in number of wind turbines q (blue '+' show standard deviation of aggregated N turbines power differences; and red circles indicate the average of those standard deviations at each q).

For example, in Figure 5.6(a), blue markers at $q = 1$ indicate the standard deviation of power differences of the individual wind turbines. The adjacent scattered values are the standard deviations of the aggregated and normalized power differences of two turbines of the wind farm of 35 and so on. The possible number of combinations of a selected q turbine can be determined using the well-known combination formula,

$$C(N,q) = \frac{N!}{(N-q)!q!} \tag{5.5}$$

where C is the combination function. This eliminates the possibility of aggregating the power of the same turbines (like $W5-W5$). Therefore, for two turbines the total 595 combinations are possible for WMR (e.g., $W1-W2, W1-W3, ..W1-W35, ...W34-W35$).

$$C(35,2) = \frac{35!}{(35-2)!2!} = 595 \tag{5.6}$$

As the value of q increases, the possible numbers of combinations also increases until q equals $N/2$. For example, in a wind farm of 67 turbines, if 35 turbines are selected (q), the total number of combinations will of order 10^{19}. Due to brevity, a maximum of 10^7 combinations are considered for the selected number of turbines. An error analysis is also conducted for the WMR wind farm for q equals five and 30 turbines, because the possible number of combinations in both cases are the

same, i.e., $3.3x10^5$. The average of standard deviations of all possible combinations (i.e. 100% combination) is presented in the first row of Figure 5.7 and considered as a reference value to estimate the error. The number of examined combinations decreases while going down the fist column. The second column estimates the average of standard deviations of the considered number of combinations of wind turbines. It should be noted that the less number of combinations are selected randomly from all possible combinations. The error between the reference value and estimated average standard deviation of the considered number of combinations is given in the third column. It should be noted that the combinations of turbine clusters are randomly selected for error analysis. As expected, the error is highest when the least number of combinations are considered and higher for five turbines than 30. Yet, in both cases, the percentage errors are small and the maximum observed percentage error is 10%. Thus, it is assumed that the 10^7 number of combinations will give reliable results.

Combinations of 5 turbines from 35

Data points	$\sigma(\Delta P_{fn})$	Error(%)
3.3E+05 = 100%	0.0507	(reference)
1.5E+05 = 46%	0.0505	0.4
1E+05 = 30%	0.0501	1.2
50000 = 15%	0.0500	1.4
10000 = 3%	0.0505	0.4
1000 = 0.3%	0.0525	4.1
100 = 0.03%	0.0548	9.2

Combinations of 30 turbines from 35

Data points	$\sigma(\Delta P_{fn})$	Error(%)
100%	0.0447	(reference)
46%	0.0447	0
30%	0.0446	0.2
15%	0.0447	0
3%	0.0450	0.7
0.3%	0.0452	1.1
0.03%	0.0455	1.8

Figure 5.7: Error analysis in the average standard deviations of 10-min power differences for WMR.

It is interesting to note that for the same number of combinations, the reference standard deviation, as well as percentage errors, are higher for five turbines than 30. This is because the overall spacing involved for the combination of 30 turbines is always higher than the 86% area covered by the wind farm, whereas large variation in the spatial-scale, from 12% to 100% is observed for the selection of five turbines. This can be seen as a spread in the standard deviations in Figure 5.6(a)) (in blue '+'). This ensures the strong dependence of power differences smoothing effect on the inter-turbine spacing as well as the number of wind turbines.

The influence of positioning of wind turbines in a wind farm on the smoothing effect of normalized power differences can be explained using the correlation between a pair of turbines. Pearson's correlation coefficient is widely used to determine the linear correlation between two signals, which is given as

$$r(\Delta P_n)_{ij} = \frac{\mathrm{cov}(\Delta P_{ni}, \Delta P_{nj})}{\sigma(\Delta P_n)_i \sigma(\Delta P_n)_j} \tag{5.7}$$

where $r(\Delta P_n)_{ij}$ represents a correlation coefficient between normalized power differences between a pair of turbines i and j. The value $\mathrm{cov}(\Delta P_{ni}, \Delta P_{nj})$ indicates the statistical relationship between two signals, i.e., either both variables show an increase (or decrease), one increases and the other decreases, or both vary independently. Therefore, the standard deviation of the normalized successive wind farm power differences depends on the average correlation coefficient of all possible wind turbine pairs as shown in Equation 5.8. For the comprehensive derivation, Appendix B can be referred. The effect of correlation coefficient on standard deviation is represented by curves in Figure 5.6 for varying average correlation from 0 to 1 (with r values) and N is replaced by q turbines. Therefore, higher standard deviations indicate a higher correlation between the normalized power differences of aggregated turbines.

$$\sigma(\Delta P_{fn}) = \overline{\sigma(\Delta P_n)}\sqrt{\frac{(1+(N-1)\overline{r(\Delta P)_{ij}})}{N}} \tag{5.8}$$

where $\overline{\sigma(\Delta P_n)}$ and $\overline{r(\Delta P)_{ij}}$ show average standard deviation and average correlation coefficient of normalized successive power differences.

It is interesting to note from the Figure 5.6, the maximum value of standard deviation ($\sigma(\Delta P_{fn})$) decreases with increasing number of turbines. In addition, the spread of the standard deviations increases when the power of fewer turbines are combined, i.e., roughly until 12% of the wind farm size and decreases afterwards. The high standard deviation values are found to be related to the closely spaced turbine clusters and the minimum values are from the turbines which are farther apart. The pattern of average standard deviation values follows an exponential decay in standard deviation with an increasing number of turbines. This analysis validates the strong dependency of successive power differences smoothing on spatial distancing compared to other parameters.
Finally, the average correlation coefficient of all pairs of turbines of the Dudgeon wind farm is 0.31, which is lower than 0.37 of the WMR. This difference in correlation may be associated with the difference in wind farm size, inter-turbine spacing, local weather conditions, and farm layout.

5.1.4. Criterion of a minimum number of turbines

From the figures 5.4(a) and 5.6(a), when the criterion is set such that the data of all 35 turbines are available, the percentage of data availability is low. The data availability increases with decreasing number of turbine criteria, but the threshold value also increases. For power ramps, to better represent ramp events associated with the wind farm, a trade-off between data availability and a lower threshold is needed. As discussed in the previous section, the standard deviation is higher when the inter-turbine spacing is smaller and decreases with increasing distance. Moreover, the standard deviations are more scattered when fewer turbines are considered, representing that the wind farm characteristics are not adequately covered. For example, in Figure 5.6(a), standard deviation values are considerably scattered for fewer than 25 turbines in WMR. One probable reason can be explained with the help of its wind farm layout of WMR. Form Figure 4.2(a), a significant spatial gap is present between the third and the fifth column (from south-west to north-east) of the WMR wind farm. Therefore, a minimum of 23 turbines needs to be considered to account for this gap and sufficiently represent wind farm variability. In this case, 25 wind turbines are selected, which roughly denote 70% of the area covered. As the farm layout of the Dudgeon is more compact, similar 70% criteria are implemented for comparable results, i.e., around 50 turbines.

In summary, the criteria of 25 wind turbines and 12.5% threshold are set for WMR, and 50 turbines with 10.5% threshold value are chosen for Dudgeon.

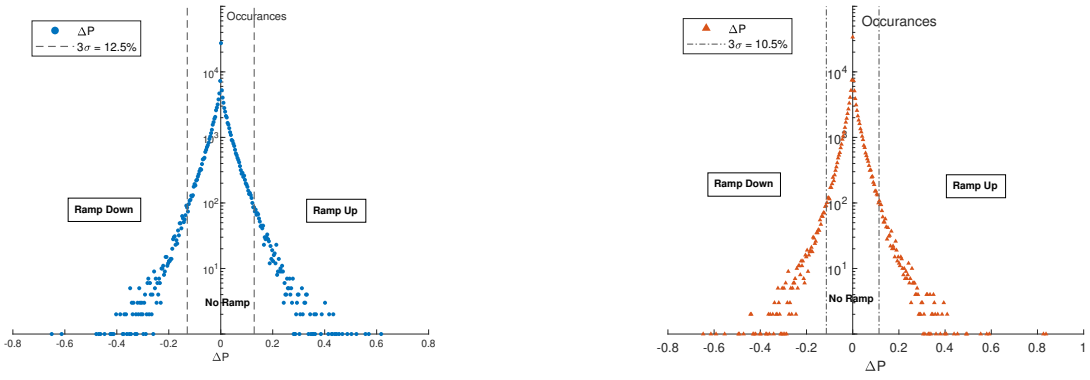

(a) WMR

(b) Dudgeon

Figure 5.8: $3\sigma(\Delta P_{fn})$ and frequency distribution of power differences.

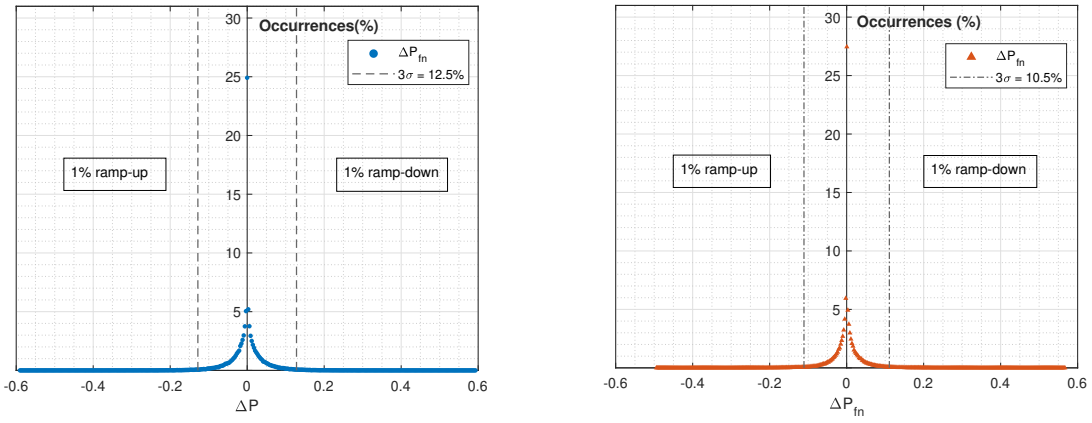

(a) WMR (b) Dudgeon

Figure 5.9: $3\sigma(\Delta P_{fn})$ and frequency distribution of power differences (same as Figure 5.8 but with the linear scale on the y-axis.

The frequency distribution of successive power differences shows elongated tails (see Figure 5.9), which are not present in the Gaussian curve [71]. Therefore, $3\sigma(\Delta P_{fn})$ gives extreme 2% ramp events,i.e 1% ramp-up and 1% ramp-down events, where the well-known Gaussian distribution would have given extreme 0.3% [72] events as the tails decay faster.

5.1.5. The ramp detection algorithm in combination with the indicator function

Once the threshold (P_{val}) and the normalized wind farm power (P_{fn}) are determined, they are given as input to the ramp detection algorithm. The algorithm first estimates the successive differences, i.e., ΔP_{fn} = P_{fn}(i+1) - P_{fn}(i). If it is greater than the threshold value, a ramp event is detected. Otherwise, the algorithm will move to the next iteration. The detected ramp event is further classified into a ramp-up or ramp-down category by using the indicator function (I). The consecutive co-directional ramp events are concatenated to get the ramp amplitude and ramp duration. Moreover, the corresponding start and end time of the events is stored to categorize events on the basis of various parameters.

The value of the indicator function, I(t) equals 1 for a ramp-up event, -1 for a ramp-down event, and 0 when a no-ramp event is detected (see Equation 3.1). Whenever its value changes, there will be start and/or end of a ramp-up or a ramp-down event. The corresponding start (T_s) and end timings (T_E) of ramp-up (T_{s-up} and T_{E-up}) and ramp-down (T_{s-down} and T_{E-down}) events are stored separately.
Let us consider an example in Figure 5.11, until t_2 the values of $T(t_1)$ and $I(t_2)$ equals 0. A ramp event starts at t_3 and $I(t_3)$ changes to 1. Therefore, the start time of ramp-up event is stored in $T_{s-up}(1)$ equals t_3. This event lasts up to t_5 and $I(t_6)$ is zero. Thus, the end time is stored as ($T_{E-up}(1) = t_5$). The corresponding ramp duration (Δ_t) and ramp amplitude (ΔP_{rn}) can be calculated as

$$\Delta_t = T_E(j) - T_s(j) \tag{5.9}$$

where, j varies from one to a length of T_s (or T_E).

$$\Delta P_{rn} = P_{fn}(t = T_E(j)) - P_{fn}(t = T_s(j)) \tag{5.10}$$

where, $t = T_E(j)$ determines the index corresponding to end time of the event.

The corresponding flow chart and an example of output power signal are shown in Figure 5.10 and Figure 5.12, respectively.

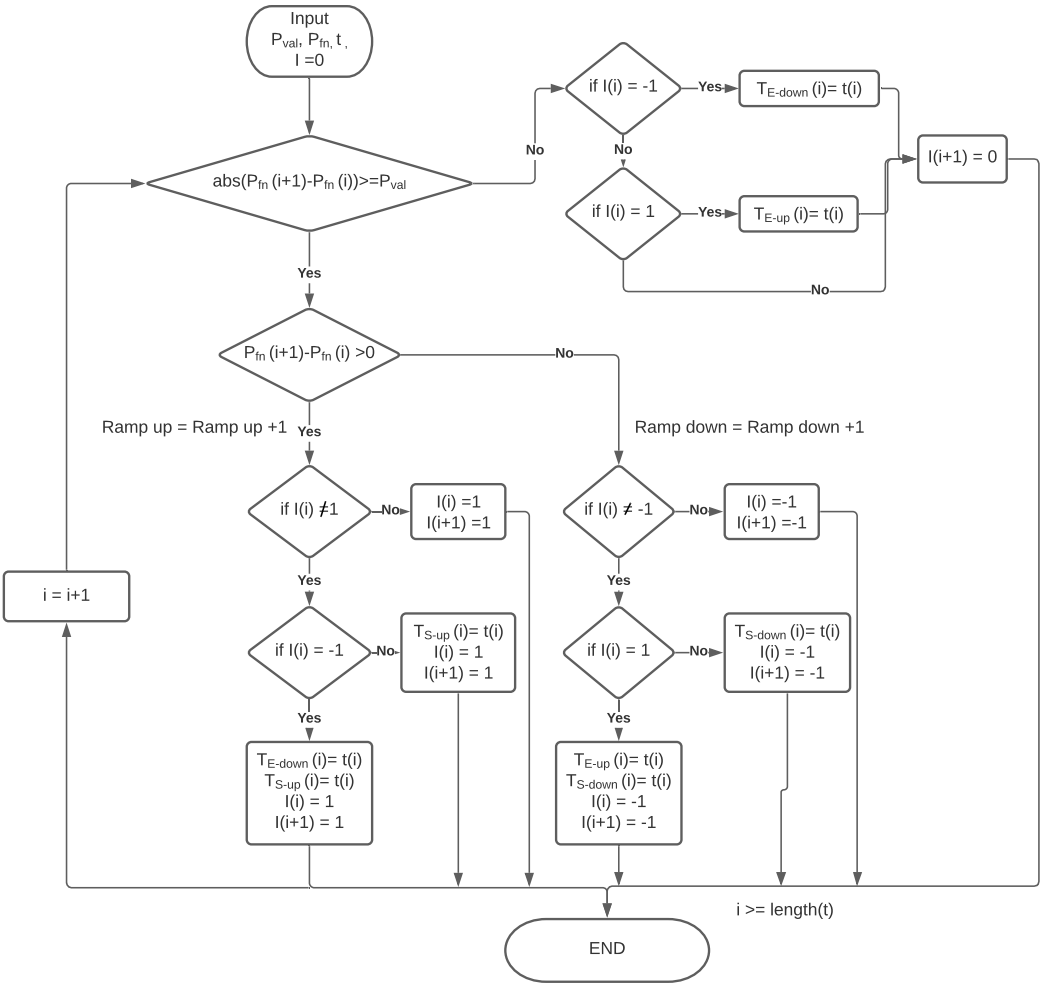

Figure 5.10: Flow chart of the ramp detection algorithm.

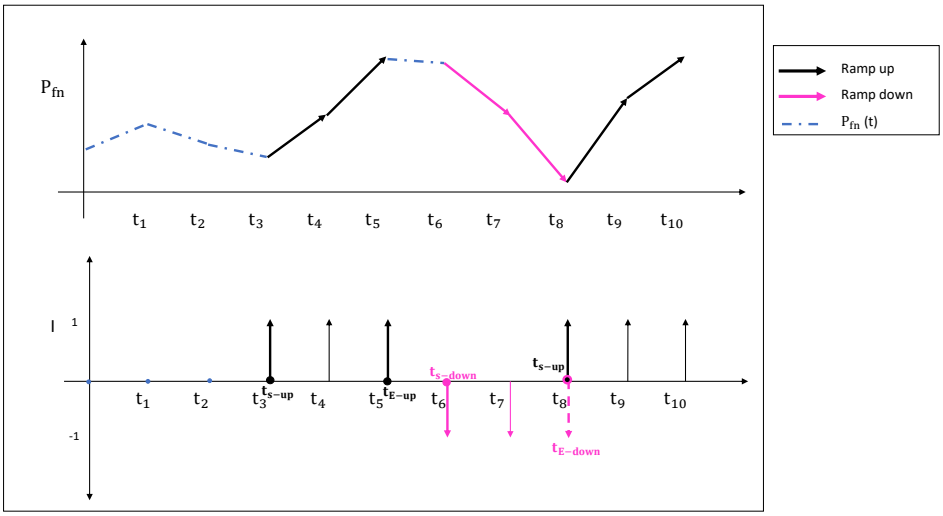

Figure 5.11: An example on application of the indicator function.

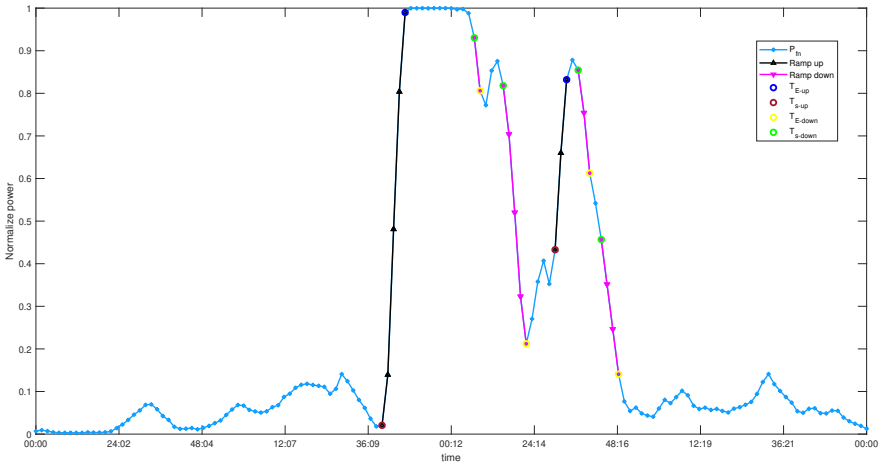

Figure 5.12: An example of the detected ramp events in normalized wind farm power time series by using ramp detection algorithm.

.

5.2. Correlation analysis

In this section, the correlations among various variables of two wind farms are reviewed. Following that, the correlation and time differences between large ramp events of two wind farms and their influencing parameters are discussed.

Figure 5.13(a) and Figure 5.13(b) represent the Pearson's correlation matrix of several wind farm variables for the WMR and the Dudgeon (as DUD) wind farms, respectively. As discussed before in subsection 5.1.3, the Pearson's correlation coefficient provides the magnitude and direction of a linear relationship between two signals. Here, correlations among pairs of signals from power, wind speed, wind direction and turbulence intensity of the same wind farm are estimated, for example: between 'Power' and 'Speed' of WMR farm. In the diagonal, all correlation coefficients are '1', due to correlations in the same signals, e.g., power and power of WMR farm. Thus, the interest lies in the lower triangular correlation coefficients. These linear correlation coefficients are graphically presented in figures 5.14 and 5.15 in lower triangular matrix with a linear fit to data (orange line).

Correlation Matrices

WMR	Power	Speed	Direct	TI
Power	1			
Speed	0.94	1		
Direct	0.04	0.03	1	
TI	-0.86	-0.78	0.07	1

(a)

DUD	Power	Speed	Direct	TI
Power	1			
Speed	0.95	1		
Direct	0.04	0.05	1	
TI	-0.9	-0.83	-0.07	1

WMR / DUD	Power	Speed	Direction	TI
Power	0.73	0.7	0.046	-0.56
Speed	0.71	0.76	0.06	-0.53
Direction	0.011	-0.003	0.73	0.003
TI	-0.62	-0.57	-0.03	0.51

(c)

Figure 5.13: Pearson correlation coefficients between the variables of (a) the WMR wind farm, (b) the Dudgeon wind farm, (c) the WMR and the Dudgen wind farms.

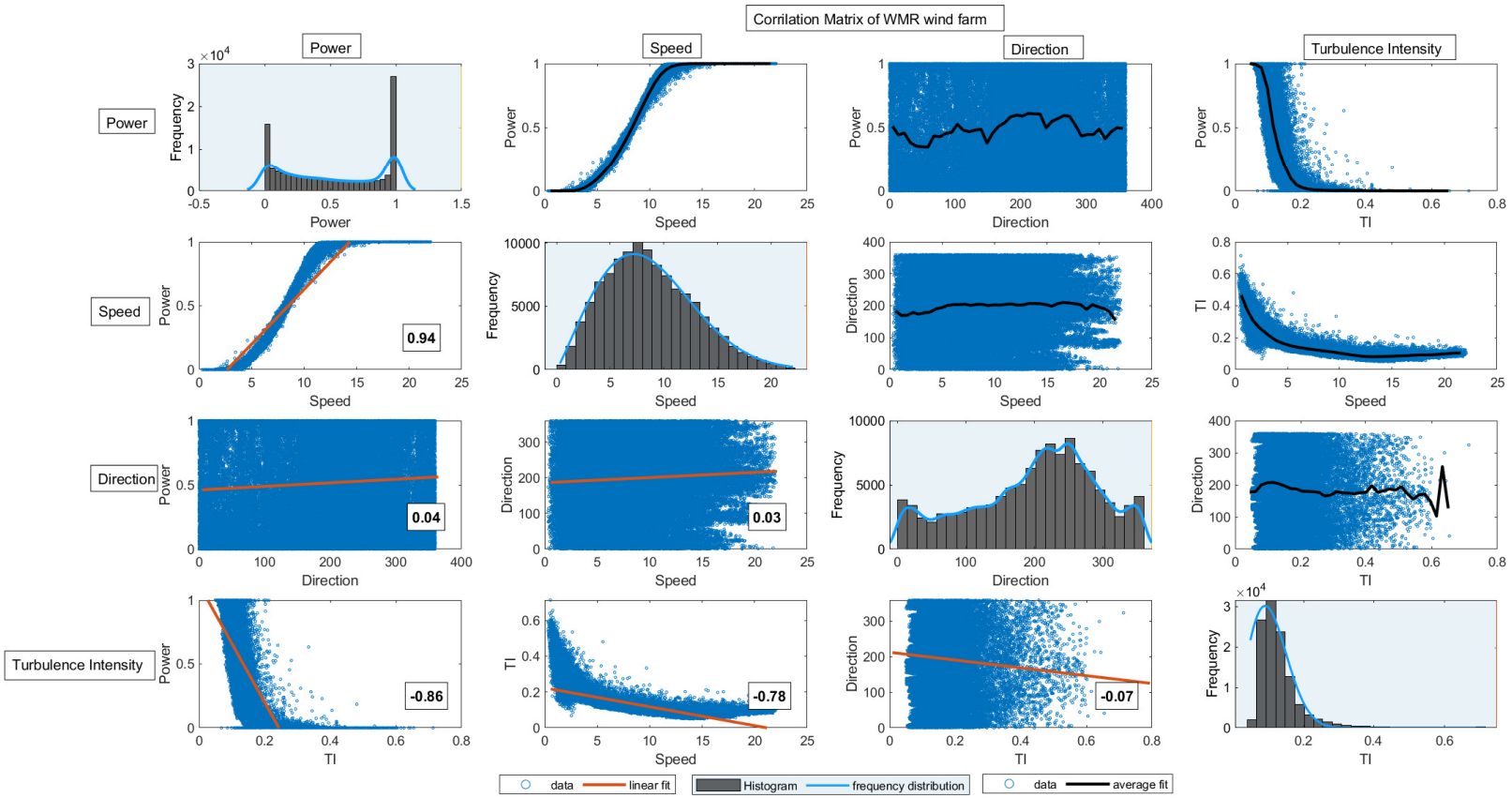

Figure 5.14: Correlation matrix: Scattered plot of WMR wind farm parameters with linear correlation (lower triangular), histograms(diagonal), nonlinear relation between parameters(upper triangular).

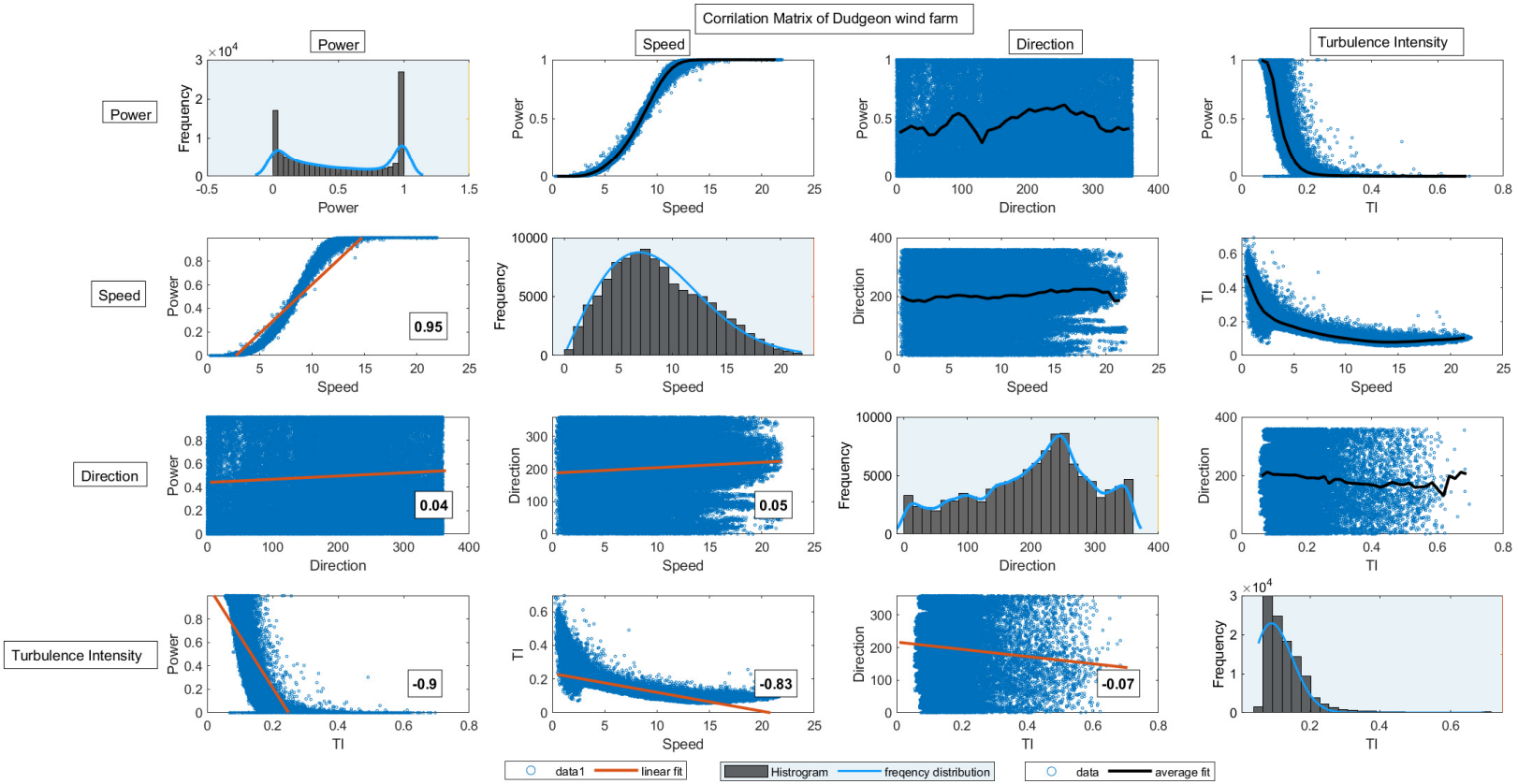

Figure 5.15: Correlation matrix: scattered plot of Dudgeon wind farm parameters with linear correlation (lower triangular), histograms(diagonal), nonlinear relation between parameters(upper triangular).

The linear correlation coefficient between the different variables is illustrated in lower triangular of Figures 5.14 and 5.15). The correlation coefficients between power and wind speed signals are 0.94 and 0.95 for WMR and Dudgeon, respectively, which are close to 1. This indicates a nearly perfect positive linear correlation between the power and wind speed signals, i.e. they vary in the same direction. This is true until rated wind speed (represented by a linear fit in the lower triangular graphs - first column and second row). Above rated wind speed, power is constant for increase or decrease in the wind speed. This non-linear relation (i.e. power curve) is shown in the upper triangular graphs (second column and first row). Conversely, the turbulence intensity (TI) and power show a negative correlation of around -0.9 , i.e. predominantly TI decreases (increases) with the increase (decrease) in power. The linear fit comprises TI (bottom left plot) values less than 0.25 because the power values show non-linear relation (Top right plot) until TI equals 0.25 and nearly constant afterwards. As expected wind speed and TI show similar behavior. However, the variations in power, wind speed, and TI are independent of the wind direction i.e. uncorrelated, as the correlation coefficients are close to 0 and the non-linear fit is also nearly a horizontal line.

The evaluated correlation coefficients between the signals of two wind farm are presented in Figure 5.13(c). The top row indicates the signals of WMR wind farm and the first column consists of Dudgeon wind farm's signals. The diagonal correlation coefficients illustrate the linear correlation between similar signals of two wind farms, i.e., the power signal of WMR and Dudgeon. These signals show fairly good positive correlation, i.e. 0.7, except for turbulence intensity. Ideally, turbulence is a short-scale event, thus uncorrelated. Yet, turbulence dissipates relatively slowly in an offshore environment. Besides, the fraction of wake added turbulence is higher than the free stream, hence upon aggregation, these turbulence intensities show some correlation on 10-min scale. Since the correlation between various parameters of two farms depends on the spatial distance between them, their size, local site condition, wind direction, and temporal and spatial length scale of the events, ramps at the two wind farms show some degree of correlation.

Considering the correlation coefficient of 0.7, during the occurrence of large-scale meteorological events, wind farms within its spatial scale will get affected simultaneously. Yet, depending upon the mean wind direction, the mean wind speed and the geographical location of wind farms, a time difference equivalent to the travel time is observed between the events that are caused by similar weather conditions.

An example of a large coherent structure that influences ramps in both wind farms is given in figures 5.16 and 5.17. In Figure 5.16, approximately at 10:00 AM a sudden increase in power ($\approx$ 100%), wind speed ($\approx$ $10 m/s$) and direction ($\approx$ 90^o) is observed. The condition resembles to the identification steps of frontal systems (subsection 2.2.1). Moreover, on the same day ramp-up event is also observed at the WMR wind farm (Figure 5.17), roughly three hours prior to Dudgeon. The event starts around 6:45 AM with westerly winds of approximately 5 m/s. These two wind farms are approximately 60 km apart in the west direction, which gives travel time of about 3 h and 15 min from WMR to Dudgeon. Besides, the vertical spacing between two wind farms is 78 km, indicating that this ramp event has a spatial scale of 78 km or higher. The WMR wind farm experiences a higher average wind speed of 20 m/s than Dudgeon (15 m/s). This could be due to the difference in local conditions, wind farm size, and farm layout. During the highest mean wind speed in WMR, around 14:30, the average incoming wind direction changes suddenly to easterly for Dudgeon. Ramps of both wind farms relax around a similar time, i.e., 16:48, with northerly winds at WMR and easterly at Dudgeon. This indicates the incoming wind direction influences the duration of a weather event.

However, analysing the correlation and time difference between ramp events of the wind farms using 10-min data set is not always straightforward. Figure 5.18 illustrates an example of such event. A ramp is observed in Dudgeon wind farm in July around 22:10 (highlighted in the black box), which is later observed at WMR around 23:30. The correlation between these power curves for the given period was found to be 0.76. However, when the power curve of WMR advanced in time by 80 min, the correlation coefficient increased to 0.92. As the events showed a similar characteristics at both wind farms, it indicates the spatial-scale of a weather event is greater than the distance of separation of the two farms (>60 km). Difference intensities of the events can be relate to the

different local effects. However, from Figure 4.1, a ramp event caused by northerly winds, was expected to first occur at WMR and later at Dudgeon. But, in Figure 5.18, the ramp is first observed at Dudgeon and then at WMR. Therefore, it is necessary to analyse weather charts to understand the true dependence of ramps characteristics of two wind farms.

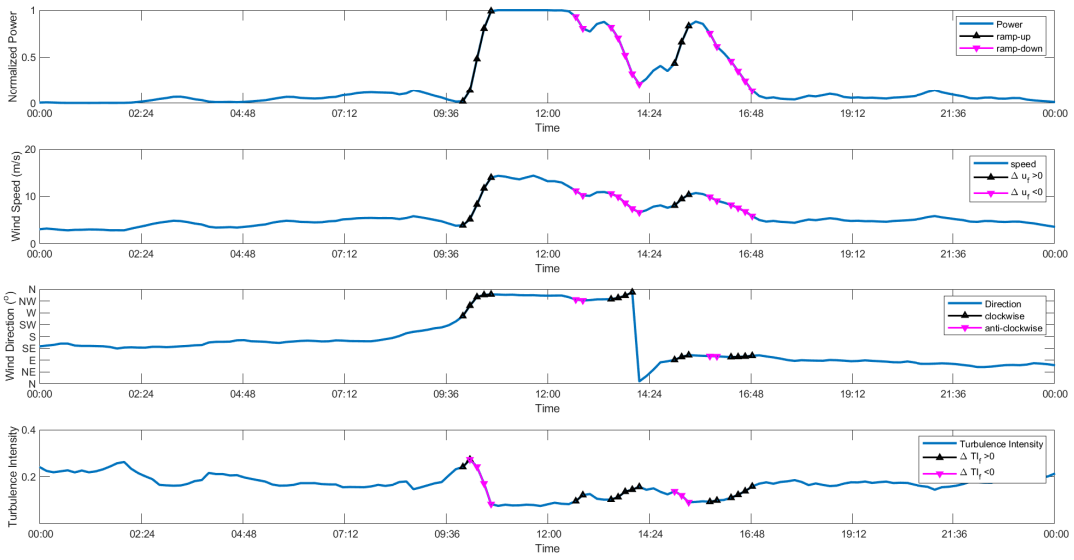

Figure 5.16: Variation in power, wind speed, wind direction and TI on a day of February of Dudgeon wind farm.

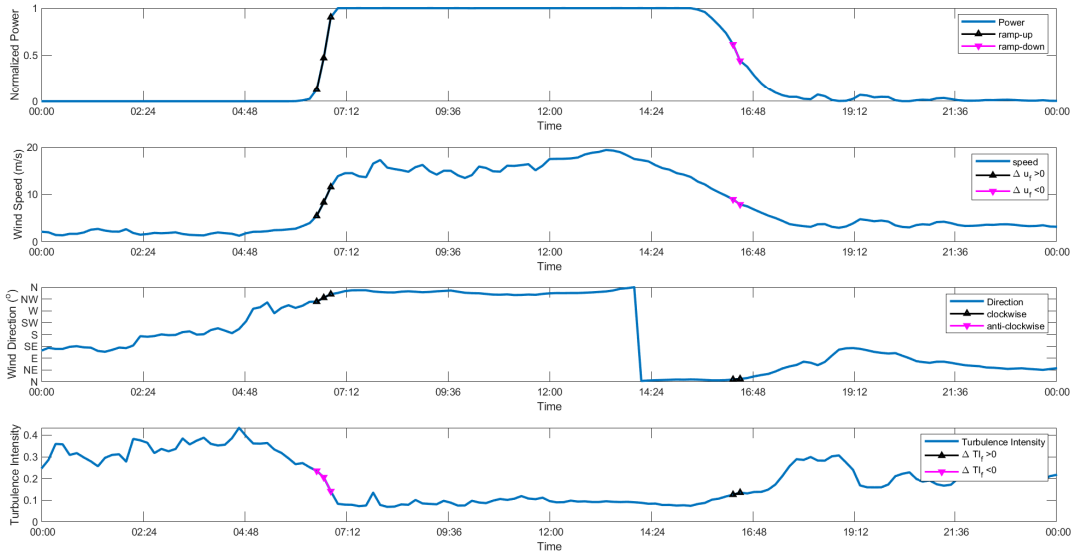

Figure 5.17: Variation in power, wind speed, wind direction and TI on a day of February of WMR wind farm.

Figure 5.19 illustrates the surface pressure chart of UK for the above-mentioned event at 00:00 UTC. In the chart, the triangles symbolise cold fronts, the semicircles represent warm fronts, combination of triangles and semicircles show occluded fronts, and small black lines are the troughs. Trough indicates the area where air is unstable. The locations of the wind farms WMR and Dudgeon are

marked as 'W' and 'D', respectively. From the chart, it can be deduced that frontal activities and unstable weather condition have given rise to ramp events. Besides, the northerly wind direction can be explained using isobars. Regions that are marked as L represent the low pressure regions. In the northern hemisphere, wind blows in the counter-clockwise direction around low pressure region, which is depicted by blue arrows near the wind farm. Therefore, both with farms experience northerly winds. However, the northerly winds are the result of a sudden change in wind direction to north. This could be the reason behind observing a ramp event first at Dudgeon than WMR. However, detailed information from upstream metorological masts or high-resolution weather data is necessary for the detail analysis.

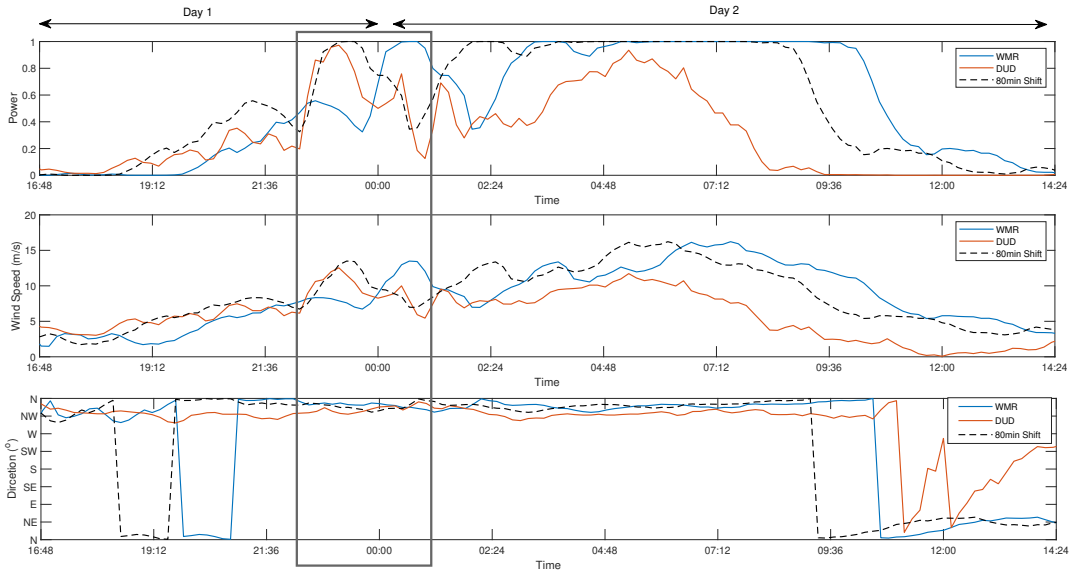

Figure 5.18: Example of ramp event observed on a two days of July, 2019 and the observed time shift between two wind farms.

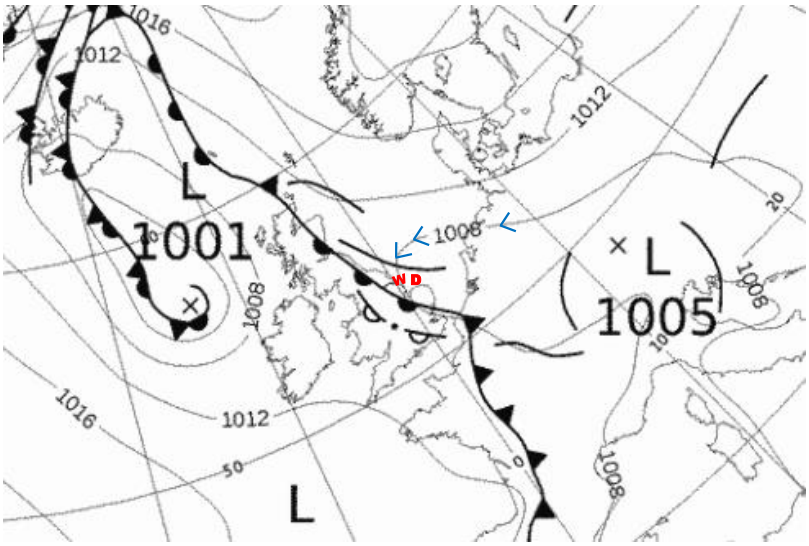

Figure 5.19: Surface Pressure chart of UK at 0:00 UTC. 'W' and 'D' represents the location of wind farm WMR and Dudgeon, respectively [73].

5.3. Categorization of ramp events

This section examines the variation in the characteristics of the detected ramp-up and ramp-down events in accordant with change in speed, direction, turbulence intensity, and ramp duration. The associated characteristics across the ramp amplitude are calculated as a difference between start and end time of the events. For example, a change in the average wind speed of a wind farm across a detected ramp amplitude is calculated using the start and end time of a ramp event as:

$$\Delta u_f = u_f(t = T_E) - u_f(t = T_S) \tag{5.11}$$

Seasonal variation

Figure 5.20 illustrates the average monthly variations of ramp-up and ramp-down events. From 2018-2019, all months have data availability with an average higher than 99%, except December 2018 and January 2019 for Dudgeon wind farm, i.e., lower than 70%. Therefore, these two months are not considered while taking the average of same month in 2018-19. In other words, the average of January and December months are represented by the number of observed ramp events in January 2018 and December 2019.

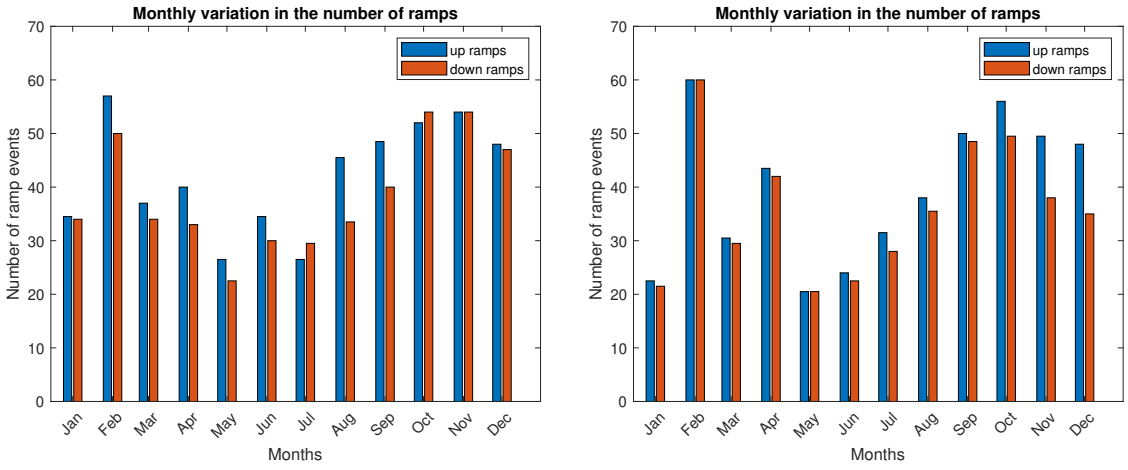

(a) WMR (b) Dudgeon

Figure 5.20: Monthly variation in number of ramp-up and ramp-down events.

As expected, more ramps occurred in the cold weather (October to April) than in warm weather (May to September). This can be because of strong winds and unstable atmosphere during winter [2]. For both wind farms, the highest number of ramp-up events were observed in February month (see Figure 5.20). A comparable number of ramp-up and ramp-down events were observed from October to December in WMR farms. Conversely, for the same months, ramp-down events showed a notable decreasing trend in the Dudgeon wind farm.

Wind speed variation

For the identified ramp-up and ramp-down events, the change in wind speed (Δu_f) showed a perfect positive statistical relationship (covariance) with the change in power (ΔP_f), i.e., wind speed changes are always positive for ramp-up events and negative for ramp-down events. In Figure 5.21, x-axis represents the absolute change in wind speeds. A similar number of ramp-up and ramp-down events were detected in both wind farms. A possible reason can be that the threshold gives percentage of ramp-up and ramp-down events, i.e. 1% see Figure 5.9). In addition, data availability, after implication of all criteria, is similar for both wind farm.

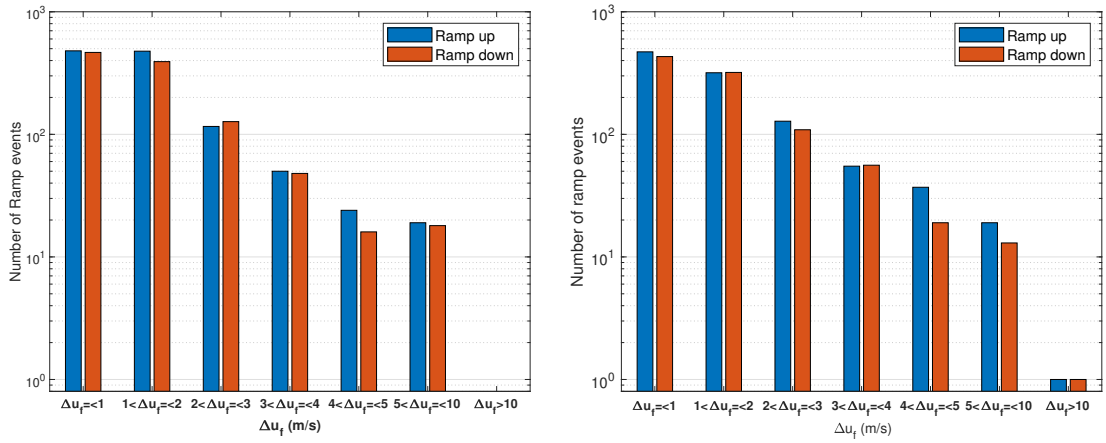

(a) WMR

(b) Dudgeon

Figure 5.21: Variation in number of ramp-up and ramp-down events with change in speed.

In addition, a decreasing trend in the of number of ramp events is observed with increasing values of wind speed difference. One reason for this is the non-linearity of the power curve. As explained in Figure 2.5, the ramp events are mainly identified in the partial load region, where power changes with the third power of the wind speed. Thus, a minor change in the wind speed gives rise to a significant variation in power output, and higher changes in wind speeds that occur near or above-rated do not have such an impact on ramp events.This effect of power non-linearity can be visualised in Figure C.7 of Appendix C. Besides, the higher wind speed changes are generally associated with the mesoscale events which are rare in the atmosphere [32].

A slightly more number of ramp events were detected in WMR farm at the lower Δu_f in contrast to the higher Δu_f for Dudgeon farm. For instance, for wind speed changes ranging from 1 to 2 m/s nearly 300 more ramps were identified at WMR. On the other hand, for Δu_f bin ranging from 4 to 5 m/s, approximately 20 more ramp events were observed at Dudgeon. Besides, the Dudgeon wind farm also experienced ramp events with Δu_f higher than 10 m/s, unlike WMR. This may be because of the comparatively large wind farm size, i.e., more number of turbines in the Dudgeon farm. The wind turbines extract kinetic energy from the mean wind flow. As a result of which, mean wind speed reduces in the downstream. The more the number of turbines in a wind farm, the more will be the energy yield, which lead to a higher average decrease in mean wind speed of Dudgeon [74]. This can be observed from figures 5.16 and 5.17, where average wind speed is higher in WMR wind farm and considerably lower in the Dudgeon. This could also be due to the wake effects of surrounding wind farms to the Dudgeon. However, it is worth noting that the wind speed differences are taken across the detected power ramp events. Thus, more ramp events are associated with wind speeds below-rated. Moreover, the thresholds (thus, smoothing effect of power differences), ramp rate, and the ramp amplitudes differ for the wind farm. For example, in the same figures, for a similar change in power, the detected amplitude of ramp-up event of WMR was smaller, and thus the wind speed change.

Turbulence intensity variation

A similar variation in number of ramp events with change in TI values is observed at both wind farms (see Figure 5.22). As the change in TI, in this section is associated with power ramp events, non-linear relation between power and TI plays a key role (see figures 5.14 and 5.15). As explained in section 4.1, TI generally decreases with increase in wind speed till transition value due to the dominant thermal effect. After the transition wind speed, TI increases with increasing wind speed as thermal effects are overcome by friction. However this transition value is close to the rated power. As a result of non-linearity of power curve, more than ≈90% ramp-up events are associated with a negative differences in TI (ΔTI_f) (see Figure 5.22). The positive changes in TI (for ramp up) could be related to the higher wind speed above transition value.

The influence of non-linear relation between power and TI on the ramp events can be better understood by the average turbulence intensity variation. The average of all 10-min TI values between the start and end time of the event represents the average TI. A similar decreasing trend in the number of ramp events is observed with an increase in average TI due to non-linear relation. Besides, 99% of the events correspond to average TI values less than 0.2. This is because, for higher TI values, power is almost constant, which can be seen in figures 5.14 and 5.15. Higher TI values are mainly related to higher 10-min standard deviation and mostly treated as extreme events. The probability of occurrence of such extreme TI events is rare in the environment. This can be also visualised from the turbulence intensity histograms, where TI occurrences are considerably low after 0.2. Therefore, a similar decreasing trend in ramp numbers is observed with increasing ΔTI_f.

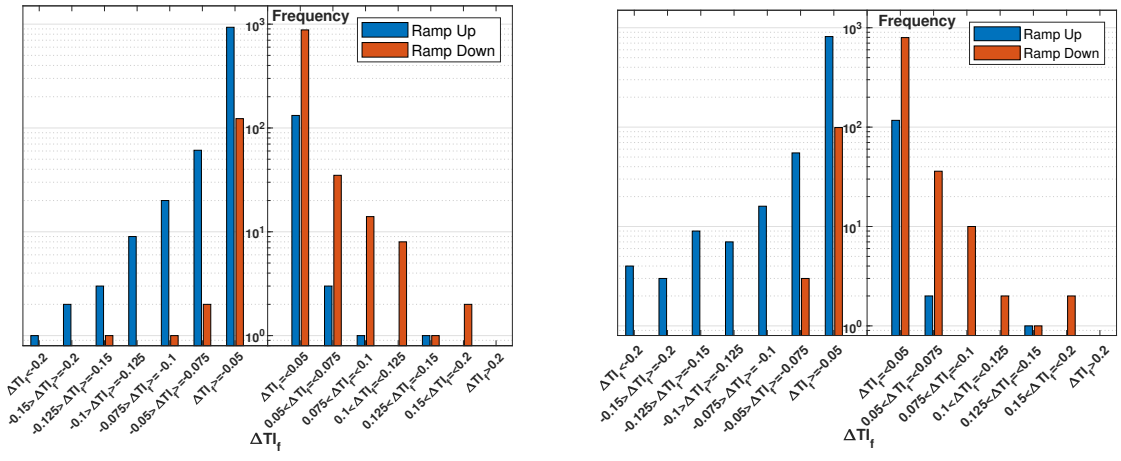

(a) WMR (b) Dudgeon

Figure 5.22: Variation in number of ramp-up and ramp-down events with change in turbulence intensity.

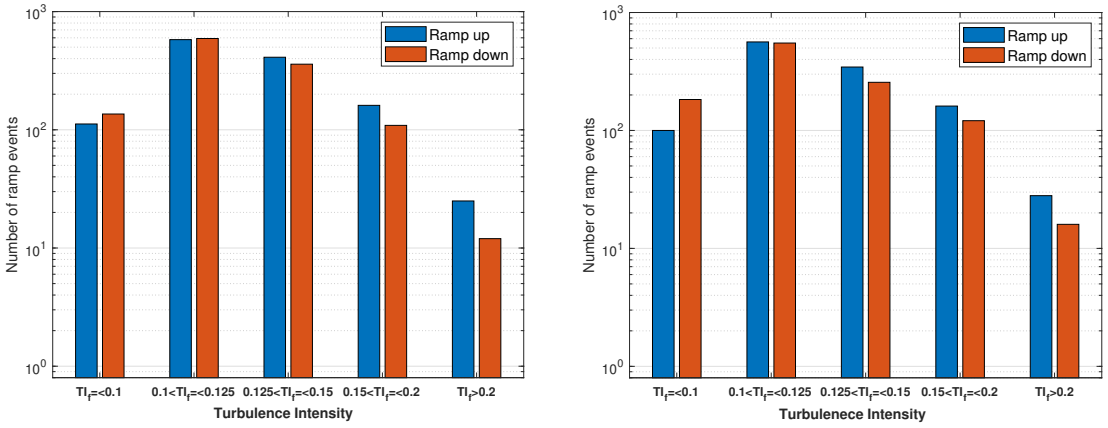

(a) WMR (b) Dudgeon

Figure 5.23: Variation in the number of ramp-up and ramp-down events with the mean turbulence intensity.

Besides the non-linearity of power curve and the probability of occurrence, wind farm size, number of wind turbines, farm layout, incoming wind direction, surface roughness, and distance from the coast also affect the change in TI of the wind farm [69, 74, 75]. As discussed earlier, extracting kinetic energy results in wind speed deficit for downstream turbines. This wind speed deficit is recovered by increased turbulence activity. Therefore, the higher the number of turbines, the higher will be the change in TI. However, the influence of inter-spatial distancing is not studied in this report.

Wind direction variation

As the name suggests, the North Sea is located in the northern hemisphere. As a result of the Coriolis effect, turbulent drag, and pressure gradient, the incoming wind direction gets deflected towards left [74]. In this region wind blows in counter-clockwise direction around low pressure region and clock-wise around high pressure region [76]. As can be seen from Figure 5.24, relatively more number of large directional change ramp events show clockwise direction change. The surface pressure chart analysis of a few of the interesting events showed high pressure region around the wind farm. This can be a reason behind detection of higher number of ramp events with clockwise changes in wind direction. Here, the clockwise direction is from south to west to north.

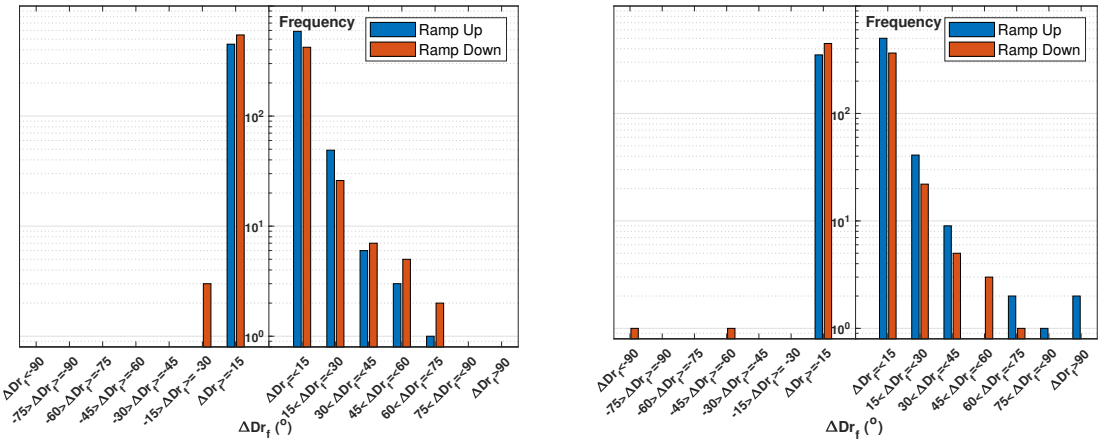

(a) WMR

(b) Dudgeon

Figure 5.24: Variation in number of ramp-up and ramp-down events with change in direction.

Similar to other parameters, the number of ramp events also decreases with increasing absolute wind directional changes (ΔDr_f). Wind directional variation mainly depends on the pressure and temperature gradient in the region. As it can be seen from Figure 5.14, wind direction is not correlated with wind power, wind speed or TI. Thus, as explained in subsection 2.2.1 the substantial changes in the wind direction could result from synoptic-scale events like cold fronts, which are rare. From figure 5.24(b), the Dudgeon wind farm experienced ramp events with wind direction changes up to 90^o, whereas no such significant shift in the wind direction was observed in WMR. The event is depicted in Figure 5.16. From the figure, the significant wind directional change is associated with a sudden wind speed increase or a large change in TI. However, based on the fluctuating wind direction around WMR wind farm at the same time (see Figure 5.17), the large directional shift could be due to the difference in local pressure and temperature distribution across the wind farm.

Variation with ramp duration

A decreasing trend in the number of ramps is also observed with increasing ramp duration values (see Figure 5.25). As explained before, the period of ramp duration depends on the wind farm size, mean wind speed, mean wind direction, length and time scale of weather events. Thus, for similar weather conditions, ramp events will take more time to pass through the Dudgeon than the WMR. Besides, the higher ramp duration also indicates a large-scale weather event has passed through the wind farm, which is rare. Figure 5.26 shows an example of a large-scale event. The black line represents the normalized average farm power (P_{fn}), where other colours show the individual turbine's power. The average wind farm power is started from zero and reached the rated wind farm capacity when the event passed through the last wind turbine.

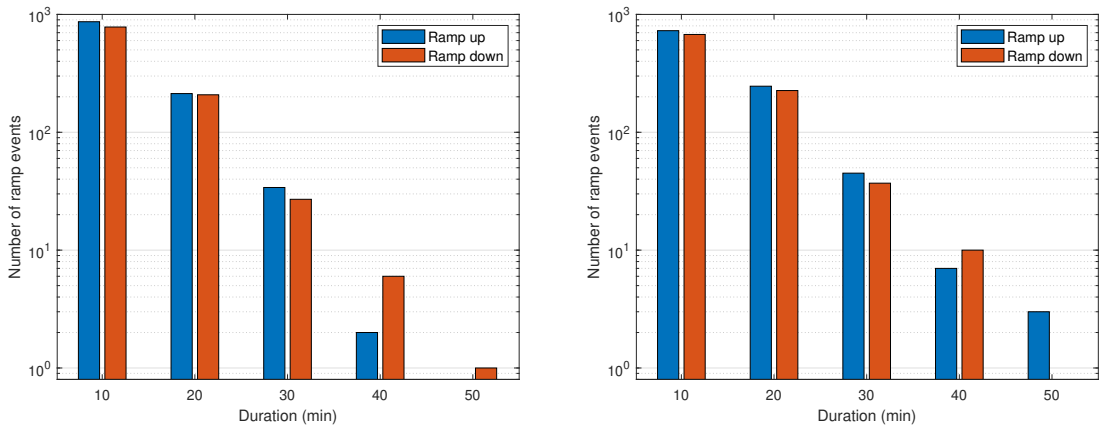

(a) WMR (b) Dudgeon

Figure 5.25: Variation in number of ramp-up and ramp-down events with change in ramp duration.

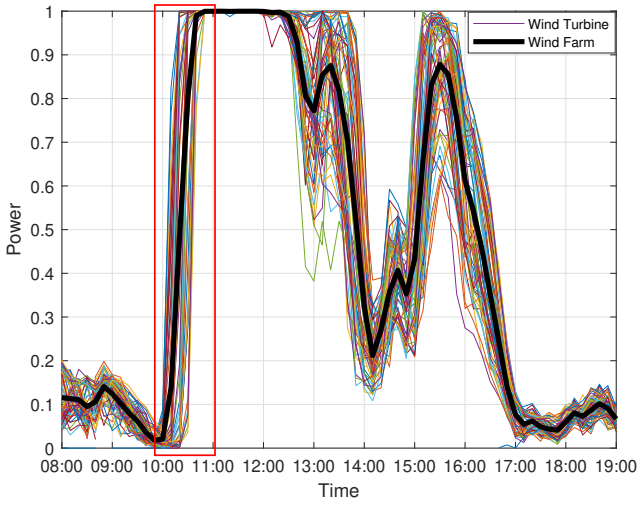

Figure 5.26: An example of large-scale ramp event (ΔP_{fn} = 95%) observed at the Dudgeon wind farm.

5.4. Summary

In this chapter, ramp events were detected and their characteristics were deeply examined using the 10-min average SCADA time series of power, wind speed (and TI), and wind direction. The analysis was conducted for WMR and Dudgeon wind farms of different sizes with different number of wind turbines.

At first, the ramp detection algorithm was developed by addressing end user's objective. For this, the ramp detection definition, i.e, ΔP_{fn}>3$\sigma(\Delta P_{fn})$ was found suitable based on the specification of the available data sets, the objective of identifying extreme wind-induced power ramp events and the smoothing effect of the normalized wind farm power difference. This chapter also addressed the influence of the techniques used to normalize aggregated wind farm power on different end-users. In order to account for wind variability and eliminate the effect of data availability at each time step, the variable capacity method was used to normalize the wind farm power. Afterwards, Therefore, the criterion was selected such that the minimum number of turbines are representative of the area covered by the wind farm, and the possible combination of their positioning doesn't lead to a large variation in the threshold. Finally, all above-mentioned criteria were implemented and by using the indicator function, ramp events were detected, categorised (ramp-up and ramp-down) and the

corresponding timings were stored.

The correlation analysis was conducted to understand the influence of various signals on the power and the relationship between the detected ramp events of two wind farms. A good degree of correlation was observed between the two wind farm variables and ramp events. Ramp events, which were approximately simultaneously observed at the two wind farms, showed some time lag. It was generally based on the average wind speed and direction of the wind farm. However, the investigation disclosed that it is not always possible to predict the weather characteristics of the events based on the SCADA data. The detailed information from upstream met masts, LiADAR or high spatial and temporal resolution weather charts are needed.

Finally, the variations in the number of ramp-up and ramp-down events w.r.t. the change in wind speed, wind direction, turbulence intensity, and ramp duration was observed. Both wind farms experienced ramps of nearly similar characteristics. However, because of the comparatively large wind farm size and more wind turbines, Dudgeon wind farm faced events of longer duration, higher wind speed, and direction changes than WMR. Moreover, both wind farms showed a decreasing trend in the number of ramp events with increasing characteristics. The primary reason could be the non-linearity of the power curve. The high changes could also be associated with the large length and temporal scale weather phenomena, which are less frequent in the atmosphere.

6

Ultimate Load Validation for Ramp Events

Before investigating the influence of ramp events on extreme loads of an OWT, validation of aeroelastic simulations with measurements is crucial to ensure the reliability of the results. In this regard, the simulations were obtained by tuning the parameters of the aeroelastic model with the measurements. This can also verify against any large uncertainties involved in the calibration. The goal of this chapter is to validate the simulation results of DLC 1.2 and DLC 1.3 against the measured 10-min minimum blade root, maximum tower top and base moments (see Figure C.1 for 10-min statistics of high-frequency time series). The selection of 10-min extreme moments as either minimum or maximum moments is, as explained in 4.2, based on the local coordinate system of the component and the direction of the wind-induced forces (i.e., direction of thrust and tangential force). For, this thesis, the load analysis is only performed for turbine D40 (see section 4.3).

IEC DLC 1.2 embodies the loads experienced by an OWT due to normal atmospheric turbulence during its operational lifetime. Therefore, section 6.1, compares the average of the 10-min maximum (or minimum) DLC 1.2 results to the average of the maximum (or minimum) measurements. The validation of 10-min average simulations with the measurements is given in section C.5 of Appendix C. Since DLC 1.3 simulates the loads caused by the extreme turbulence, the average of its maximum (or minimum) results is validated with the extreme measurements in section 6.2.

6.1. DLC 1.2

In this section, all moments are normalised by the corresponding maximum (minimum for blades) DLC 1.2 moment at rated wind speed. In this section, "average" refers to the average of the 10-min maximum (or minimum) moments. Measurement data points are significantly scattered, which could be due to turbulence, wake effect, inertia, or control response of an OWT. Moreover, 10-min maximum (or minimum) moments are plotted against the 10-min average wind speed, which can differ from the wind speed at which extreme moments occurs.

Figures 6.1 and 6.2 show sufficient agreement between the average measurements and the simulations. The simulations satisfactorily match the measurements for all wind speed bins for blade root edge-wise, tower top side-side, and tower top fore-aft. For the flap-wise (see Figure 6.1(a)) and tower base fore-aft (see Figure 6.2(c)) moments, the simulation model slightly overestimates the moments after reaching rated speed. On the other hand, it is observed that the average of measured tower base side-side moment (Figure 6.2(d)) is higher than the simulations up to the rated speed. Overall, a maximum of 10% discrepancies was observed in the simulations and the measured averages. The discrepancy in the tower base side-side moment might be caused by the available simulations correspond to the unidirectional wind-wave conditions, while an average of 45^o wind-wave misalignment was observed in the measurement data. Another possibility is that

the aerodynamic damping effect is not well predicted above rated wind speed. Or NTM is perhaps the ultimate load driver after rated wind speed. In order to discover the root cause, an analysis of high-frequency time series is needed.

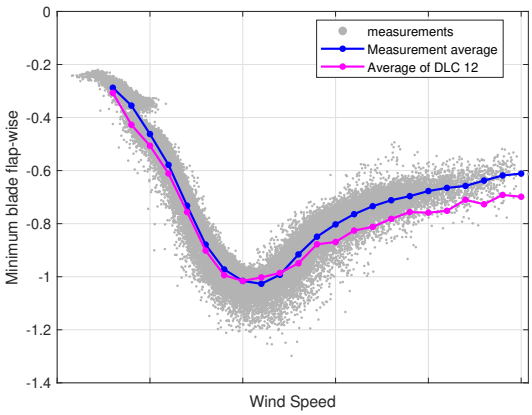

(a) Minimum Blade root flap-wise moment

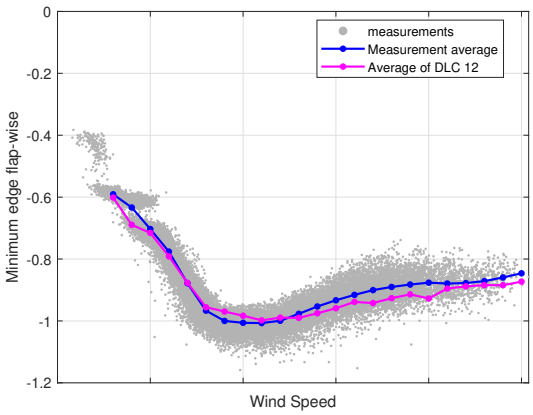

(b) Minimum Blade root edge-wise moment

Figure 6.1: Minimum blade root flap-wise and edge-wise moment of one blade. All values are normalized with the minimum DLC 1.2 bending moment at rated wind speed.

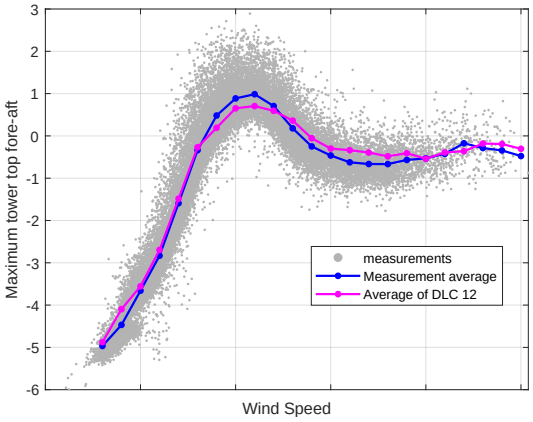

(a) Maximum Tower top fore-aft moment

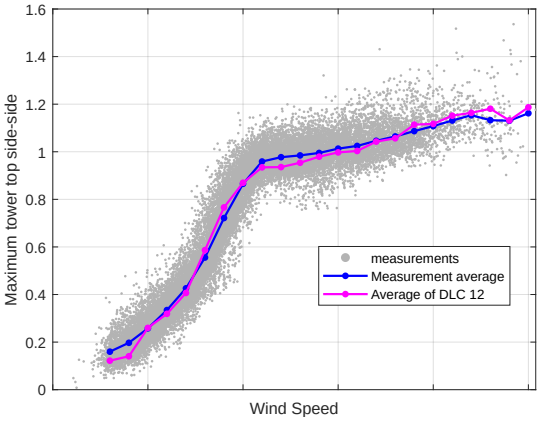

(b) Maximum Tower top side-side moment

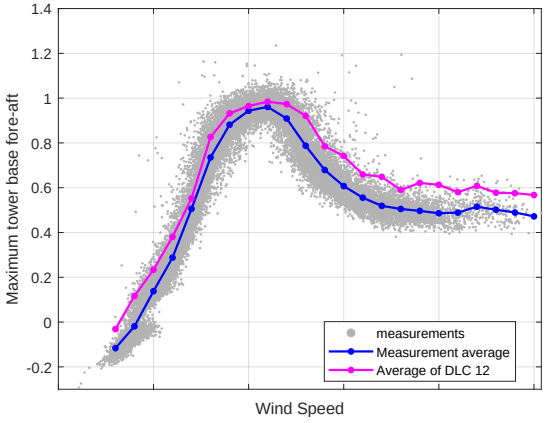

(c) Maximum Tower base fore-aft moment

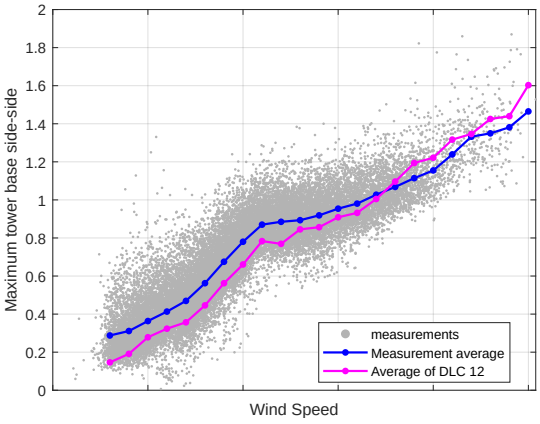

(d) Maximum Tower base side-side moment

Figure 6.2: Maximum tower top and tower base bending moments. All values are normalized with the maximum DLC 1.2 bending moment at rated wind speed.

6.2. DLC 1.3

Since DLC 1.3 simulations provide the ultimate bending moments that occur due to normal and extreme horizontal turbulence (see chapter 2), extreme 1% measurements are considered here to obtain comparable results. The value '1%' is derived using a trial-and-error method. Another possible approach would have been to use extreme nine events per wind speed bin because DLC 1.3 moments are estimated using nine different wind speed seeds. All moments are normalised by the corresponding maximum (minimum for blades) loads in DLC 1.3 at rated wind speed. Here, the term "average" refers to the average of maximum (minimum for blades) DLC 1.3 moments.

The average DLC 1.3 moments show good agreement with the extreme 1% average of the measured moments. The bars in graph 6.3 and 6.4 represent the standard deviation of the selected extreme moments per wind speed bin. It is interesting to observe that all simulations closely follow the pattern of the extreme measurements. Both minimum moments at the blade root (Figure 6.3) are higher (lower in absolute terms) than in DLC 1.3, except around rated wind speed. This can be related to the increased controller activity in this region. Similar behaviour was observed in the tower fore-aft moments. Besides, a small dip was observed in the extreme measured tower top fore-aft moment after rated wind speed, which is not present in the simulations. Moreover, the measured tower side-side moments (Figure 6.4(b) and (d)) are almost always greater than the simulations. For the tower base side-side moment, this can be caused by the higher wind-wave misalignment of measured data than 0^o of available simulation (as mentioned before in (section 6.1).

6.3. Discussions

In general **DLC 1.2** satisfactorily matches the average of the 10-min maximum (or minimum) measured moments. Thus, it can be concluded that the model is a good representative of the measured loads and that there is no significant calibration uncertainty. The minor errors may be related to the wind speed errors due to the blade passing fluctuations (see chapter 4).

Yet, the discrepancies in tower fore-aft and blade root flap-wise moments could be due to the slightly high prediction of thrust force in the simulation model. In addition, the downsizing of the turbine in the simulation can change the aerodynamic properties [27]. As the IEC NTM is representative of the 90% turbulence levels [24], the higher simulation results might be related to these values. On the other hand, the higher average of tower base side-side than DLC 1.2 can be associated with the wind-wave misalignment. Measurements showed an average wind-wave misalignment of 45^o, while only simulations of unidirectional wind-wave alignment are available for this thesis.

DLC 1.3 satisfactorily matches the extreme 1% moments. In general, the absolute measured moments are generally lower than the simulations, except around rated wind speed. This can be related to the increased controller activity near rated wind speed. The higher average tower base side-side moments than simulations might be related to the higher wind-wave misalignment. However, the maximum DLC 1.3 results can be higher than the measurements because the bars indicate the standard deviations of the moments in each bin rather than the maximum (or minimum).

It is interesting to see how do ramp events affect the extreme loads, which will be dealt with in the next chapter.

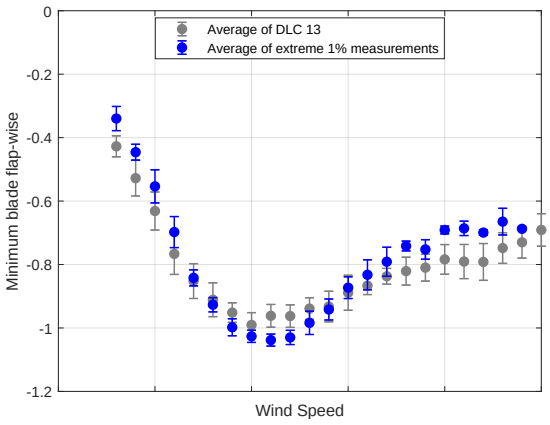

(a) Minimum Blade root flap-wise moment

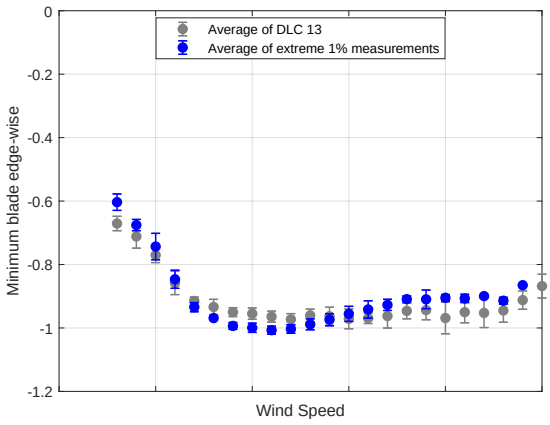

(b) Minimum Blade root edge-wise moment

Figure 6.3: Comparison of average extreme 1% blade root moments with extreme average DLC 1.3. The bars indicate the standard deviation of the selected moments per wind speed bin. Measurements are normalized by the minimum DLC 1.3 bending moment at rated wind speed.

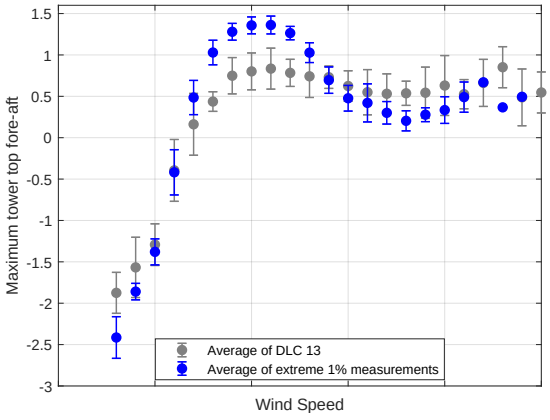

(a) Maximum Tower top fore-aft moment

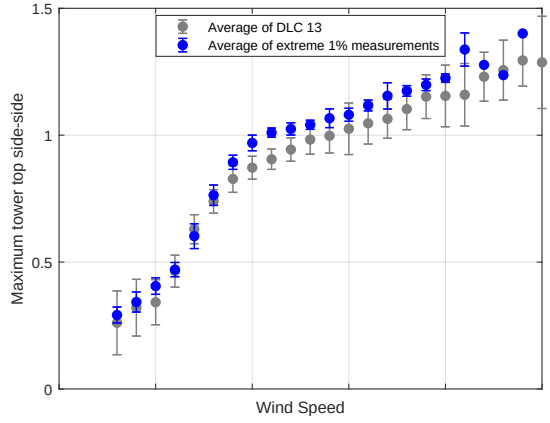

(b) Maximum Tower top side-side moment

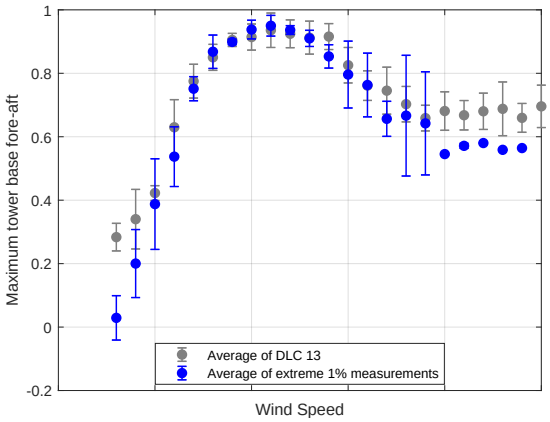

(c) Maximum Tower base fore-aft moment

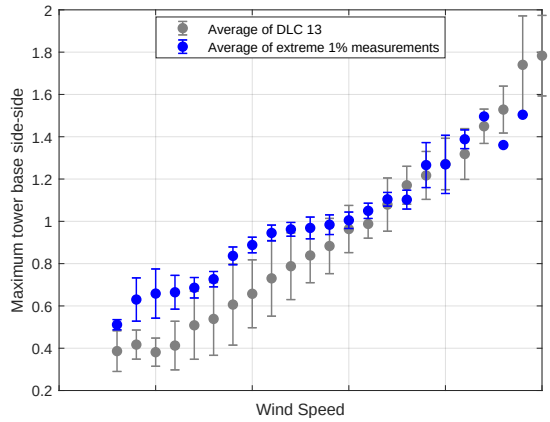

(d) Maximum Tower base side-side moment

Figure 6.4: Comparison of average extreme 1% blade root moments with extreme average DLC 1.3. The bars indicate the standard deviation of the selected moments per wind speed bin. All moments are normalized with the absolute maximum DLC 1.3 moment at rated wind speed.

7

Impact of Ramp Events on Ultimate Wind Turbine Loads

This chapter addresses the primary research objective of this thesis, i.e., the investigation of the influence of ramp events on the ultimate wind turbine loads. The impact of wind power and wind speed ramp events is analysed in the first section 7.1. The subsequent section 7.2 examines the effect of ramp-like extreme wind speed fluctuations on ultimate loads and compares with DLC 1.3 simulations. High-frequency data of a couple of interesting events are scrutinised in section 7.3 to discover the underlying cause.

Adhering to confidentiality and for the better understanding of results, the bending moment curves are divided based on the controller regions, which were shown in Figure 2.6.

7.1. Wind power and wind speed ramp events

At first, wind power ramp events in the normalized power time series of a single turbine D40 are detected using the ramp detection algorithm (see Figure 5.10) with 18% threshold ($3\sigma(\Delta P_n)$). This threshold, as expected, is higher than the overall wind farm threshold of 10.5% due to the smoothing effect of wind farm power differences (see subsection 5.1.4). These events were further categorised into a ramp-up or a ramp-down category. The events were not concatenated to get the ramp amplitude and duration, but their influence on the loads is observed on the 10-min basis.

Since the wind power ramp events are majorly associated with the non-linearity of the power curve and Hannesdóttir et al. [13] found that extreme wind speed ramps affect the ultimate wind turbine loads, the ramp detection algorithm (see Figure 5.10) is also run for identifying wind speed ramps. In this case, input was a 10-min average wind speed signal and the threshold was set to 2.1 m/s, i.e., $3\sigma(\Delta u)$.

Once wind power and wind speed ramps are identified, their influence on extreme wind turbine loads is analyzed. For instance, Figure 7.1 compares their impact on the 10-min minimum blade root flap-wise moment. The bending moments associated with ramp events are highlighted in purple and orange colours according to the ramp direction. In Figure 7.1(a), as expected, the loads associated with the wind power ramps related loads are mainly concentrated in the region 2, due to the non-linearity of the power curve (see Figure 2.5). This can be seen by a peak representing the highest percentage of the occurrence. The average of these loads per wind speed bin is approximately similar to the overall measurement average. In contrast, the loads related to the wind speed ramps are uniformly scattered and show a distribution similar to Gaussian, with a relatively higher percentage of data points at rated wind speed (see Figure 7.1(b)). The average of these moments per wind speed bin is slightly lower (higher in absolute terms) than the average of the total measurements. Before the region, $2\frac{1}{2}$, the average per wind speed bin approximately

represents the extreme loads. However, from the region $2\frac{1}{2}$ onwards, it closely follows the overall measurement average per wind speed bin. The other bending moments show nearly similar behaviour, which is given in section C.6 of Appendix C.

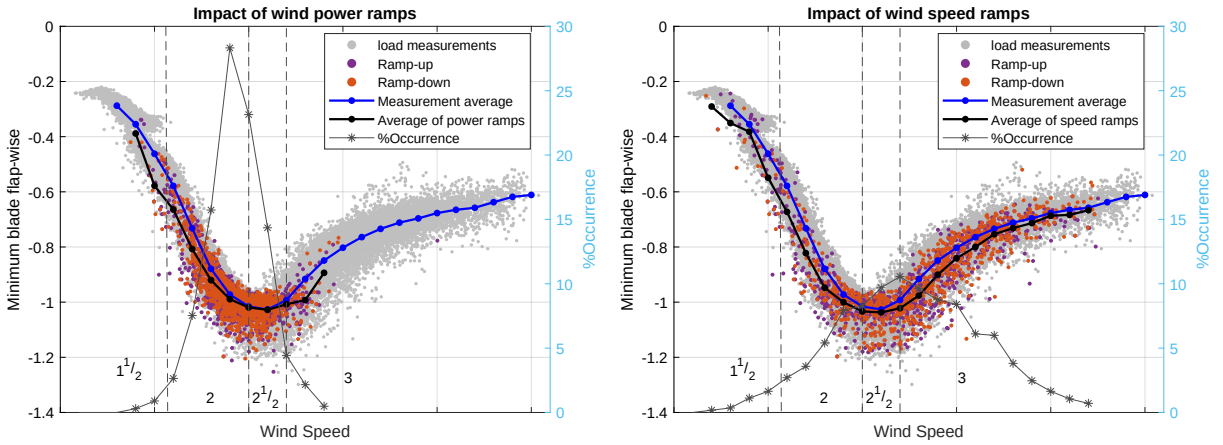

(a) Influence of wind power ramps on the minimum blade root flap-wise moment.

(b) Influence of wind speed ramps on the minimum blade root flap-wise moment.

Figure 7.1: Coloured markers indicate loads associated with power ramps. Blue line represents average of all measurements, whereas black line denotes the average of loads associated with ramp events. Measurements are normalized with absolute minimum DLC 1.2 moment at rated wind speed.

7.2. Extreme wind speed fluctuations

Hannesdóttir et al. [13] found the extreme horizontal wind speed fluctuations that exceed the prescribed IEC 61400-1 standard (edition 3) [77] are wind speed ramps and influence extreme loads on a wind turbine. The site conditions of the Dudgeon wind farm fall under IEC turbulence class C, which is similar to the aforementioned literature. Therefore, to determine the extreme fluctuation events, at first, 10-min standard deviations (σ_u) of the horizontal wind speeds are plotted against 10-min mean wind speed (u), as depicted in Figure 7.2. Afterwards, by using the IEC ETM class C Equation 7.1, standard deviations are estimated over the wind speed range.

$$\sigma_u = cI_{ref}(0.072(\frac{u_{ave}}{c}+3)(\frac{u}{c}-4)+10) \tag{7.1}$$

where c = 2 m/s, I_{ref} is 0.12 and 0.14 for class C and B, respectively [77]. u_{ave} is taken as average of entire available wind speed data set.

Figure 7.2(a) represents the variation in horizontal wind speed standard deviation when wind speed signal is unfiltered. The values higher than 6 m/s of standard deviation value are not presented in the graph for comparison with filtered signal. The number of extreme fluctuation events dropped drastically after filtering the wind speed data (see Figure 7.2(b)) w.r.t. availability of bending moments. Therefore, to draw substantial conclusions, events with standard deviations higher than 90% standard deviation of IEC ETM C are considered as extreme wind speed fluctuations. It should be noted that, in Hannesdóttir et al. [13], the author only considered events higher than the ETM class B, which is due to the higher data availability of 10 years.

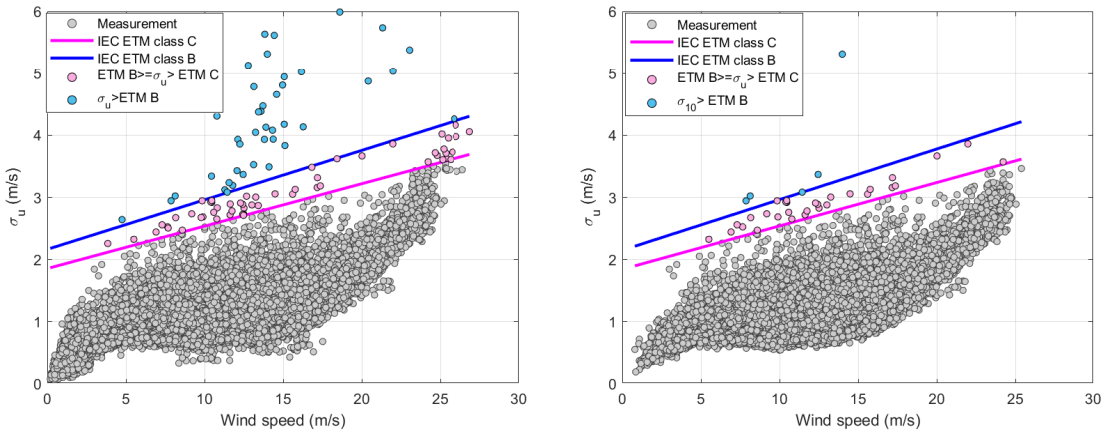

(a) Unfiltered (b) Filtered

Figure 7.2: Extreme observed horizontal wind speed standard deviations (σ_u) compared to IEC ETM class C and class B. Grey scatters correspond to raw measurements, pink dots denote standard deviations higher IEC ETM class C and blue dots indicate their values greater than class B.

In figures 7.3 and 7.4, extreme fluctuation events are highlighted with black markers. The comparatively lower frequency of these events for the tower bending moments is due to the lower availability of the tower data than blades (see section 4.3). The blue and orange lines represent the average of measured and DLC 1.3 loads, respectively, per wind speed bin. The triangles indicates the maximum (or minimum) value of DLC 1.3 per wind speed bin. All graphs are divided as per control regions (Figure 2.6).

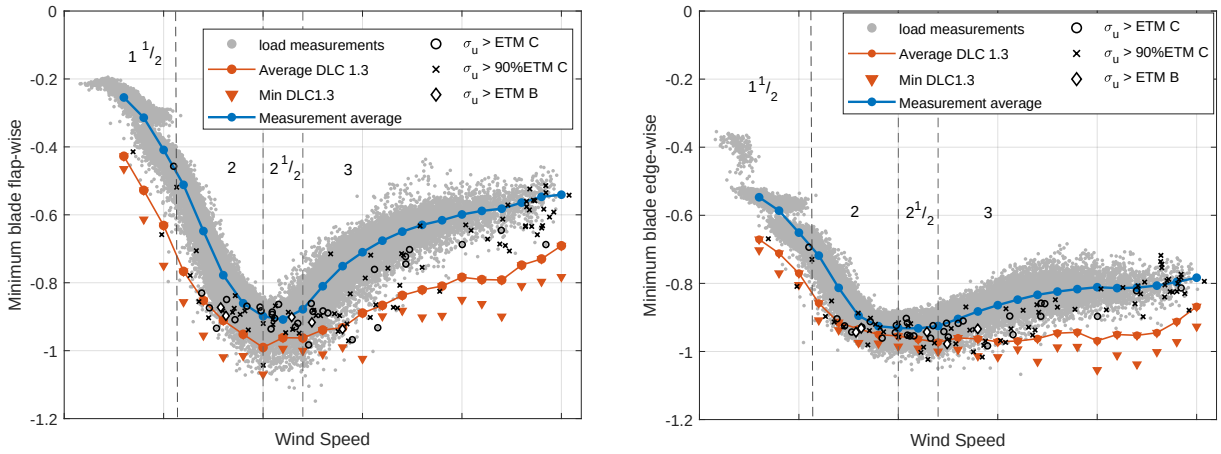

(a) Minimum Blade root flap-wise moment (b) Minimum Blade root edge-wise moment

Figure 7.3: Influence of extreme fluctuations on the minimum blade root flap-wise and edge-wise moments. All moments are normalized with the absolute minimum DLC 1.3 moment at rated wind speed.

In general, these events are likely to govern higher loads in regions 2 and 3, whereas in the region $2\frac{1}{2}$, extreme fluctuations mainly fall near average loads. The lower loads could be related to the increased pitch activity near the rated region. On comparing with simulations, loads associated with extreme fluctuations events, in general showed lower values than the respective maximum (or above minimum) moments of DLC 1.3, except for tower side-side moments. These higher values of tower side-side moments could be related to the wind-wave misalignment or yaw error (see section C.7). In contrast, constrained simulations of extreme fluctuation events in Hannesdóttir et al. [13] exceeded DLC 1.3 results for blade root flap-wise and tower base fore-aft moments in region 2 and 3. All other moments were well within the DLC 1.3 results.

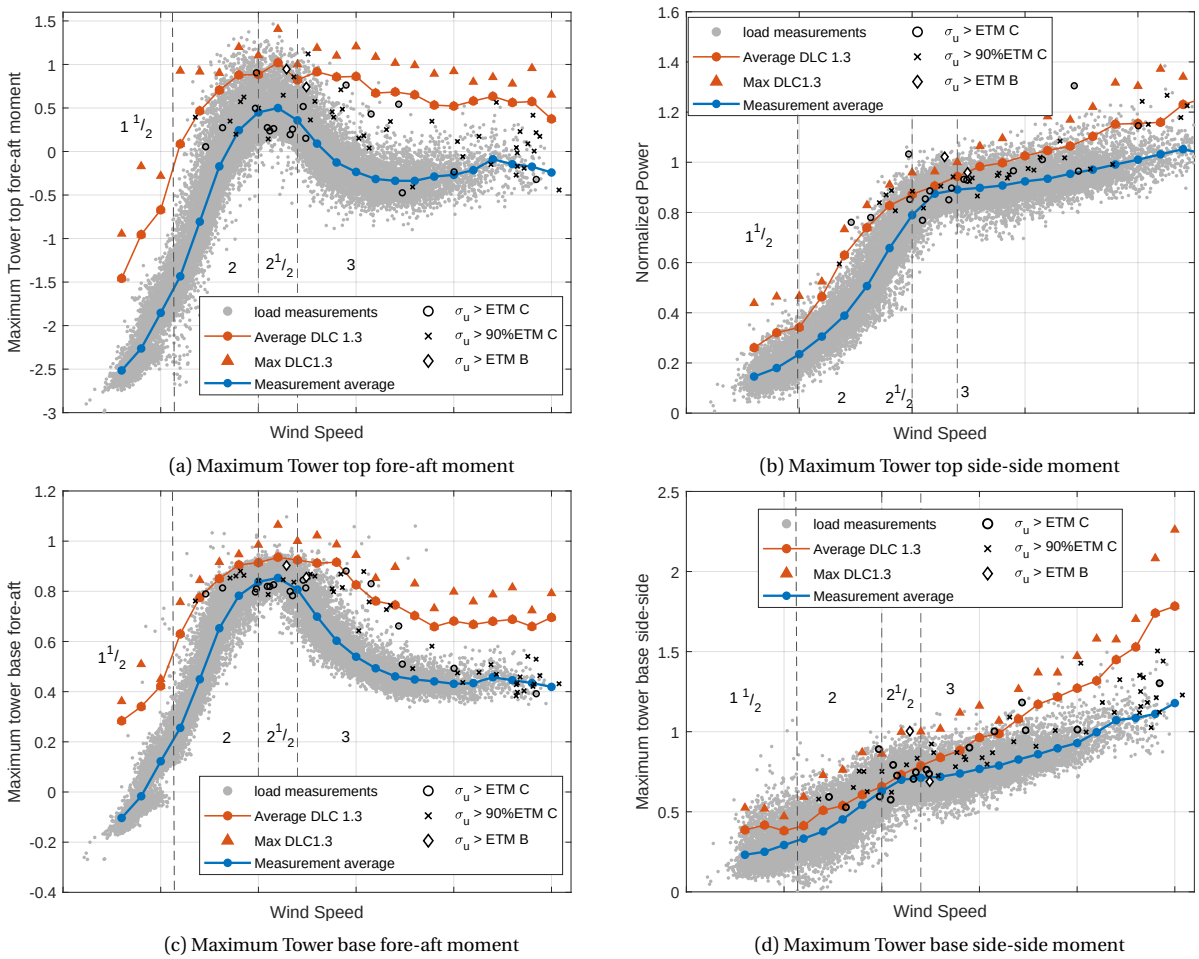

(a) Maximum Tower top fore-aft moment

(b) Maximum Tower top side-side moment

(c) Maximum Tower base fore-aft moment

(d) Maximum Tower base side-side moment

Figure 7.4: Influence of extreme fluctuations on the maximum tower top and base moments. All moments are normalized with the absolute maximum DLC 1.3 moment at rated wind speed. The graph is divided as per the control regions.

Aside from extreme fluctuations, some of the measured loads near the regions $2\frac{1}{2}$ and 3 exceed the extreme loads predicted by the DLC 1.3. To determine the plausible cause of higher or lower loads in each region, a few interesting events are selected for high-frequency analysis based on their intensity such as, fluctuations higher than IEC ETM B, higher than IEC ETM C, higher than 90% IEC ETM C and near the rated region with extreme loads higher than DLC 1.3. The high-frequency data of such events are investigated in the next section.

7.3. Analysis of high-frequency time series

Figure 7.5 illustrates the high-frequency (25 Hz) wind speed time series of four selected events as per their turbulence class. Similar to Hannesdóttir et al. [13], wind time series of extreme fluctuation events, i.e., standard deviations higher than ETM class C show a ramp-like increase or decrease. A sudden increase in wind speed with an average rise time of 100 s is observed for the event having standard deviation higher than IEC ETM class B (see Figure 7.5(a)). Approximately at the same time, a ramp-up event is observed at D44, which is at a 1.8 km distance from D40. With decreasing standard deviations, the rise (or fall) time of events increases and amplitude decreases. For instance, in Figure 7.5(b), an event with standard deviation IEC ETM B$\geq \sigma_u >$IEC ETM C, showed a fall time of around 300 s. With the further decrease in the σ_u, events start transforming to turbulent. Further, Figure 7.5(d) illustrates the time series of the minimum blade flap-wise moment. This event shows a lower value of $\sigma_u \approx 1.6$ m/s. The associated time series of the generator rotational speed,

pitch angle, yaw angle, blade and tower bending moments are examined further in this section.

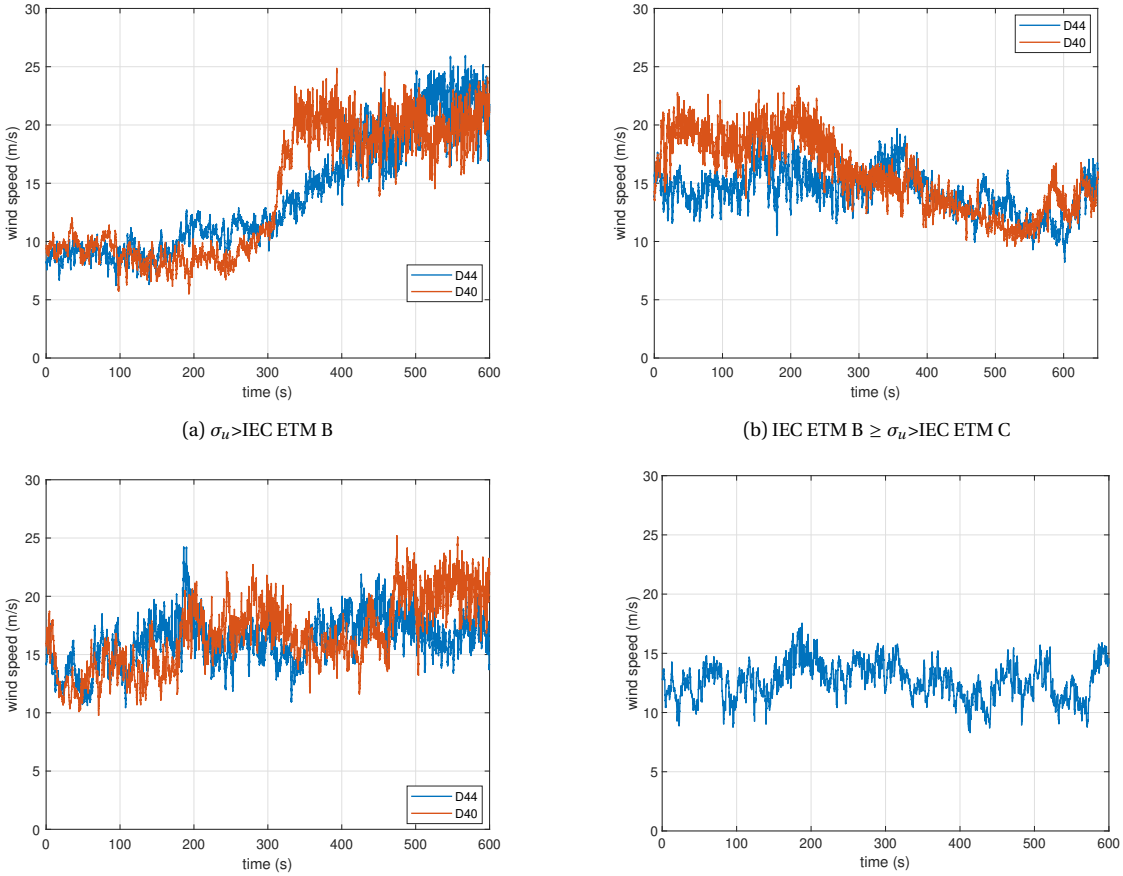

(a) σ_u>IEC ETM B

(b) IEC ETM B $\geq \sigma_u$>IEC ETM C

(c) IEC ETM C $\geq \sigma_u$>90% IEC ETM C

(d) at extreme blade flap-wise moment

Figure 7.5: Comparison of wind speed time series of turbines D40 and D44, which are ≈ 1.8 km apart.

An event of σ_u>IEC ETM B

For the selected event, an explicit ramp-like increase (or decrease) is observed in all presented time series, and it is highlighted by the red box in Figure 7.6. The wind speed time series initially showed a gradual increase around 300 s followed by a sudden increase. Also, the intensity of wind speed fluctuations is observed lower around the ramp-like structure compared to a no-ramp region (see Figure 7.6(a)). Interestingly, the tower top side-side moment showed a similar pattern (see Figure 7.6(f)), but with a shorter rise time as power reaches the rated capacity (see subsection 2.1.3). The ramp-like increase is also observed in other bending moments and pitch angle around the same time, indicating coherent structure across the length of the turbine. When a blade starts pitching (see Figure 7.6(d)), a sudden peak in the tower fore-aft and blade root flap-wise moments is observed before the reduction in absolute values (see Figure 7.6(b), (e) and (h)). Yet, the moments are not extreme because of the faster pitch response to a comparatively long duration of the ramp. In other words, as explained in Bierbooms [78], as the rise time of ramp events is much longer than the time constant of controller activity, the ramp related variation in were handled by the controller. Moreover, approximately 90% drop in the blade root flap-wise moment, 80% rise in tower base side-side moment and 60% drop (or rise) in the other moments is observed in less than 50 s, except blade edge-wise moment.

Figure 7.7 compares time series of this event at turbine D40 and D44 for the same 10-min duration. A ramp event at D44 showed a longer time duration to reach the same wind speed level as the turbine D40 (see Figure 7.7), which could be a result of wake effects (see Figure 4.2). Despite the slower

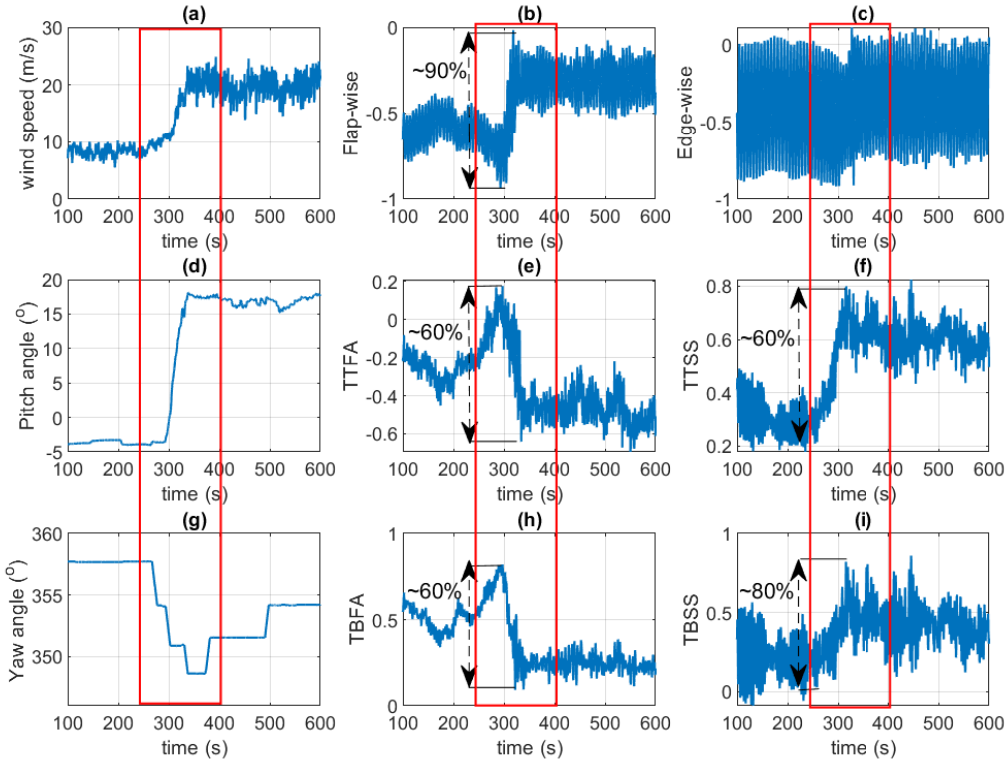

Figure 7.6: The time series of various parameters for an event of σ_u > IEC ETM B. The associated period of a wind speed ramp is highlighted in the red box. All moments are normalized with the absolute maximum DLC 1.3 moment at rated wind speed.

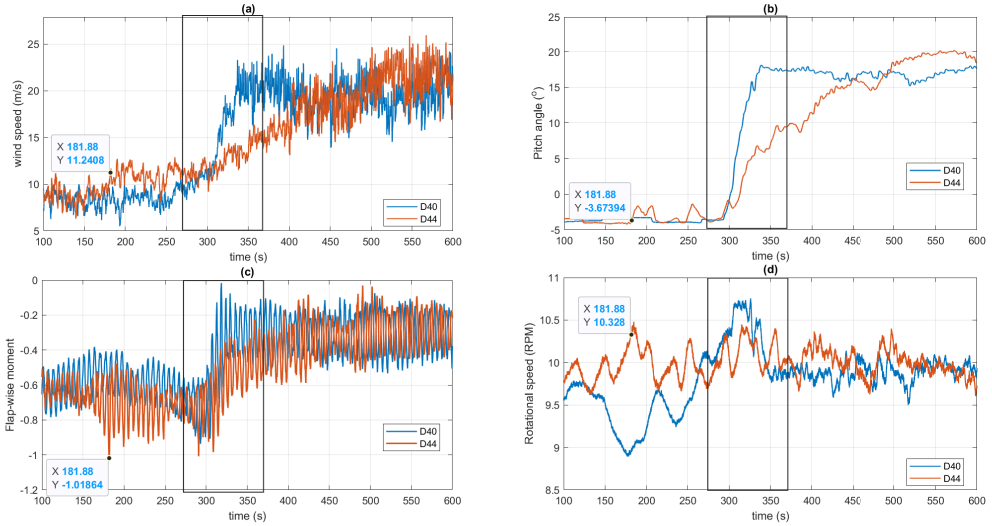

Figure 7.7: Comparison in time series of D40 and D44. The black box highlights the ramp event observed in D40. X and Y coordinates show the time and other signals value at the local minimum blade root flap-wise moment, respectively. All moments are normalized with the absolute maximum DLC 1.3 moment at rated wind speed.

transition, the blade root flap-wise bending moment is lower (higher in absolute terms) for turbine D44 than D40. Moreover, the local minimum value in the specified 10-min duration is not associated with a ramp event, but, wind speed fluctuations near rated wind speed. This leads to a sudden pitch

transition from inactive to active, which can be observed in the pitch curve around the minimum blade root bending moment (see Figure 7.7(b) in orange). The rotational speed time series of D44 showed fluctuation around 10 rpm, whereas ramp-like variations is observed in the time series of D40. The comparative higher turbulence at turbine D44 may be associated with the wake added turbulence, as D44 is in the wakes of turbines D37 and D38 (see Figure 4.2(b)) for northerly winds (assuming no yaw misalignment). In Kelly et al. [79], the author also found the higher extreme loads for downstream wind turbines than upstream based on constrained simulations with ramp-like wind speeds. Thus, if a no-ramp region is near rated wind speed and involves sudden fluctuations demanding pitch activation, this can result in higher loads than DLC 1.3 in the wind speed bin.

An event of σ_u>IEC ETM C

For the selected event, 10-min minimum flap-wise moment is observed close to the minimum DLC 1.3 moment for that specific wind speed bin. In the 10-min wind speed time series, ramp-like decrease is observed with a fall time of around 300 seconds. Figure 7.8 shows the high frequency time series different, where local maximum (or minimum) loads are highlighted in the red box. The wind speed dropped close to rated wind speed, followed by sudden increase resulted in a peak in the blade flap-wise moment (see Figure 7.8(a) and (b)). However, because of the ramp-like decrease in 10-min time series, from 20 m/s to 10 m/s, the average of the event falls under the 15 m/s bin. Therefore, it could be said that extreme moments are mainly associated with the pitch transition from inactive to active region (see Figure 7.8(d)).

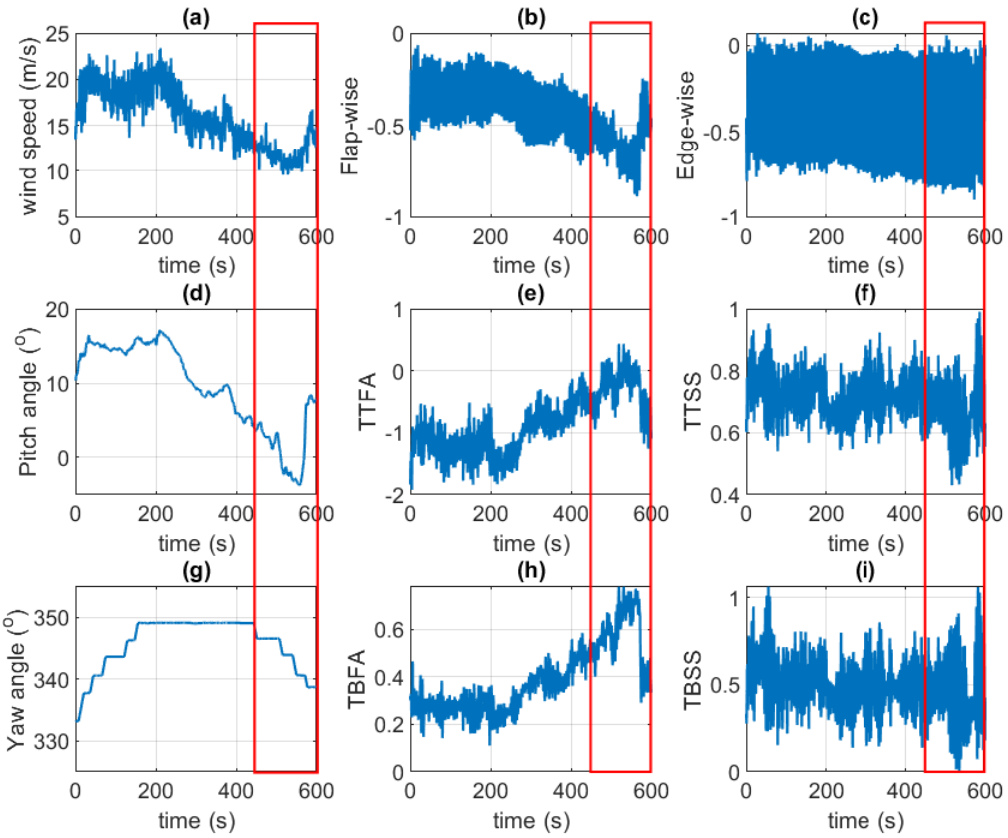

Figure 7.8: Time series plot of various parameters for IEC ETM B $\geq \sigma_u >$ IEC ETM C. All moments are normalized with the absolute maximum DLC 1.3 moment at rated wind speed.

An ETM time series of similar wind speed statistics, i.e., mean and standard deviation, showed an analogous ramp-like decrease approximately at the same time as the measurements (see

Figure 7.9(a)). However, simulation time series consists of comparatively higher fluctuations than measurements (focused in black box). Moreover, minimum blade root flap-wise moment also occurred as a result of transition from region pitch inactive to active (see Figure 7.9(b)). The resulted blade root flap-wise bending moment from DLC 1.3 simulations showed lower minimum value than measurements, as the wind speed fluctuations were significantly higher (see Figure 7.9(c)). Thus, it could be said that the DLC 1.3 satisfactorily predicts the moments related to such time series.

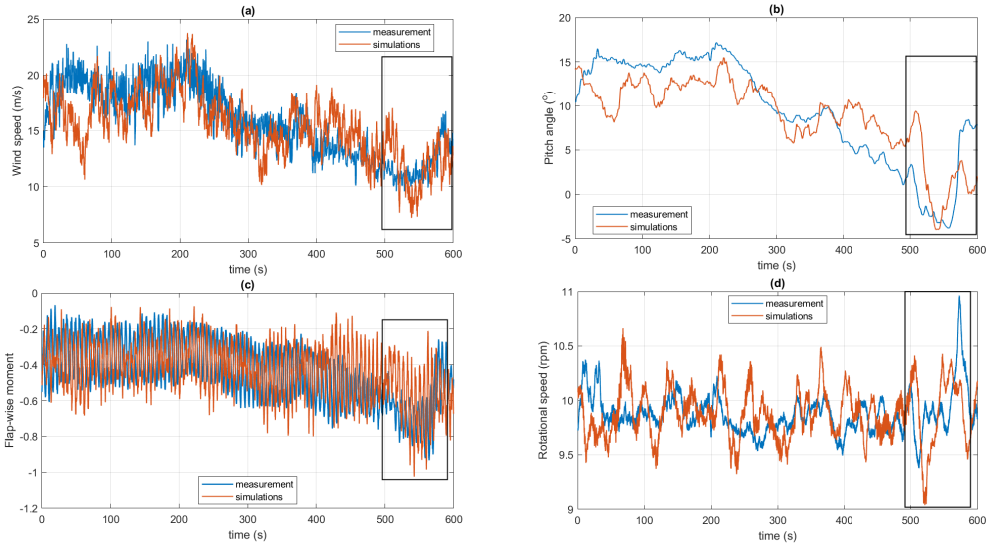

Figure 7.9: Comparison of measurement and simulation time series of similar wind speed statistics.

An event of the minimum blade root flap-wise moment

The Figure 7.10 represents high-frequency time series of different measurements at the lowest (highest in absolute terms) measured blade root flap-wise moment (highlighted in the red box). The corresponding event showed a lower turbulence than DLC 1.3 and the 10-min average wind speed is close to the rated. Therefore, any slight fluctuations in the wind speeds leads to the transition from inactive to active region within a few seconds (Figure 7.10(d)).

Figure 7.11 highlights the exact timing and corresponding signal values in that 10-min time series. Similar to aforementioned events, pitch was inactive (optimum angle at -4^o) before the occurrence of this event (see Figure 7.11(b)). In addition, rotational speed was also observed close to the rated speed of 9.9 rpm. Also, as expected, the extreme flap-wise moment corresponds to the 1P rotational frequency (see Figure 7.12), which could be due to the tower shadow, wind shear, or turbulence of the equivalent time scale [39]. The dominant time period of consecutive peaks is estimated from Figure 7.11(c) as 6 sec, which is as expected same as 1P.

One could argue that the exceeding blade root flap-wise moments should be compared with 10-min minimum DLC 1.1 moments, because DLC 1.1 yields ultimate loads experienced by normal turbulence in 50-years recurring time. However, IEC DLC 1.3 is designed such that the ultimate loads from DLC 1.1 should not exceed DLC 1.3 [77], i.e. DLC 1.3 includes the ultimate loads from DLC 1.1.

Comparison of the measured wind speed time series with the simulation of similar statistics shows that the NTM model has relatively smaller fluctuation intensity than measurements (see Figure 7.13(a)). However, one could argue that the measured wind speed time series may include added blade passing fluctuations (see section 4.1). As the measured rotational speed time series is given input to the control system, the power spectrum density (PSD) graphs of measured and simulated rotational speeds are compared Figure 7.14. For better understanding, the PSDs are smoothed out. For higher frequencies than 3.5 Hz, fluctuation amplitudes (energy) of the measured rotational speed were observed higher than the simulation. Therefore, the increased fluctuations

around near rated wind speed region (region 2 and $2\frac{1}{2}$) and observed higher energy in the high-frequency region can be the probable reasons for higher loads.

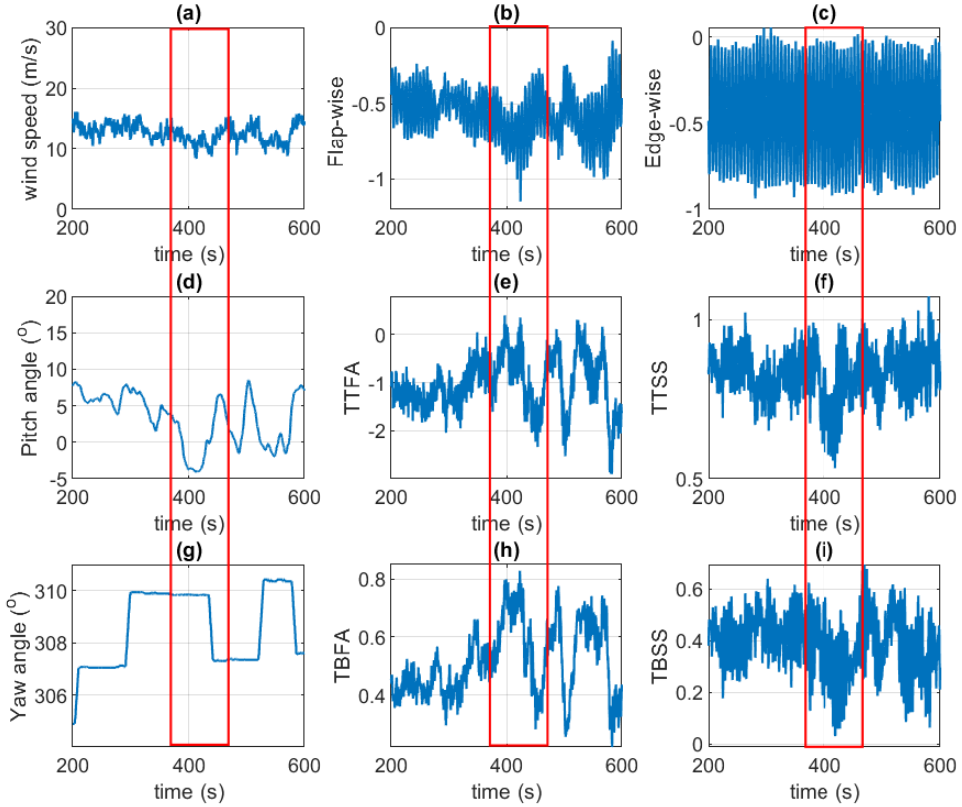

Figure 7.10: Time series plot of various parameters at minimum observed blade root flap-wise moment. All moments are normalized with the absolute maximum DLC 1.3 moment at rated wind speed.

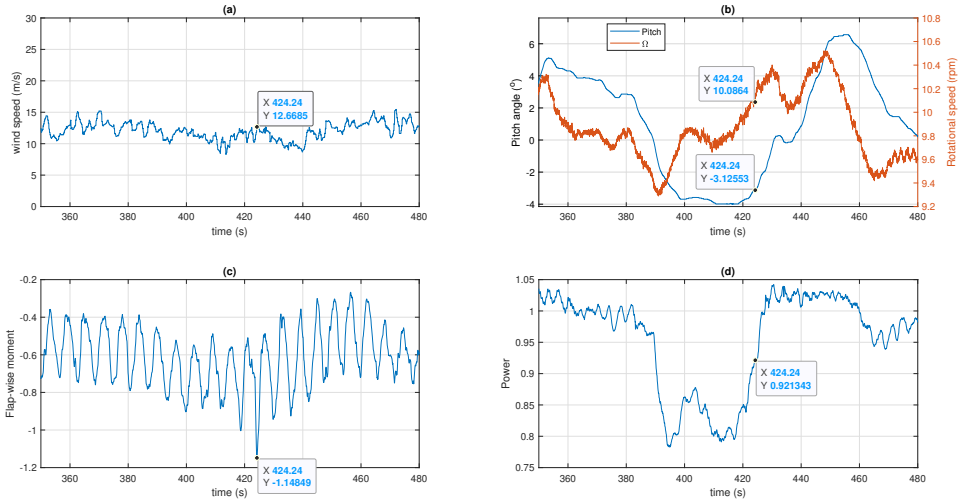

Figure 7.11: Variation in wind speed, rotor speed, pitch angle, power, and normalized blade root flap-wise moment. X coordinate shows the time of lowest load and Y represents other signal values at corresponding time.

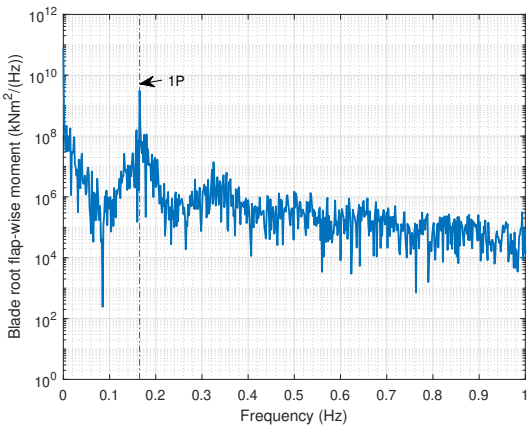

Figure 7.12: Power spectral density of blade root flap-wise moment.

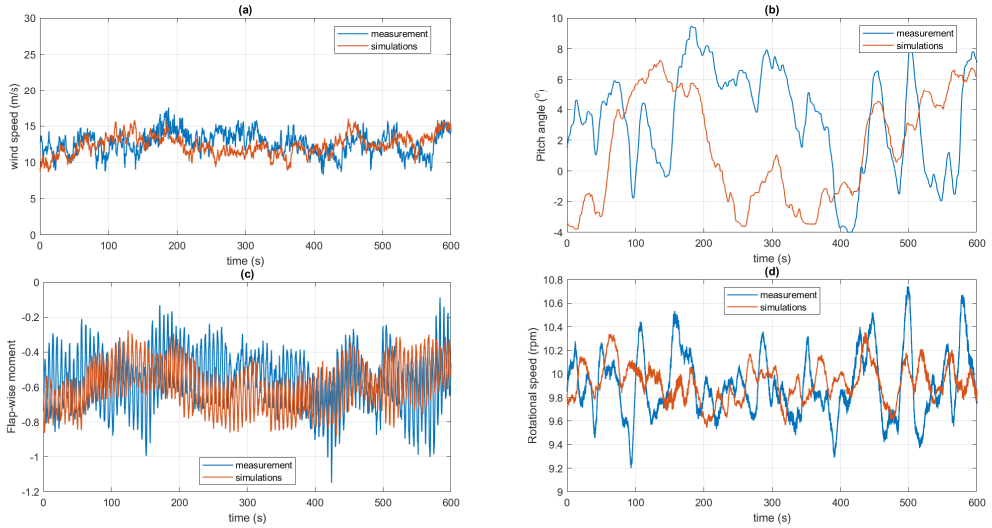

Figure 7.13: Comparison of measurement and NTM simulation time series of similar wind speed statistics.

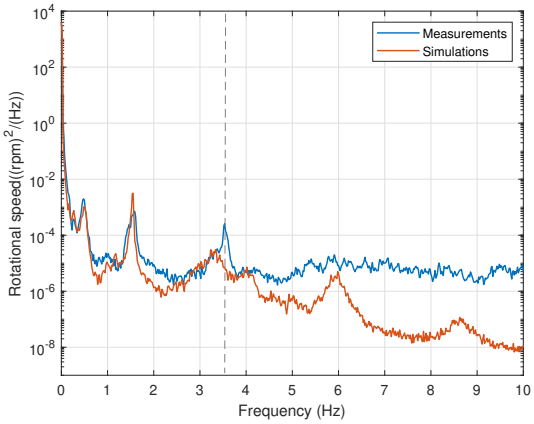

Figure 7.14: Comparison of measured and simulated power spectrum density of rotational speed.

An event of maximum tower base fore-aft moment

The data points corresponding to the maximum tower base fore-aft moment were found to be errors in the data set. They can be observed as sharp peaks in the tower base fore-aft, and side-side moments Figure 7.15. To remove such errors, the 10-min time series is discarded if the difference between 10-min maximum and average is higher than 3-4 times the standard deviation of series. While obtaining 10-min statistics, it is recommended to add an additional check, i.e., if the difference between the two highest maxima in 10-min time series is larger than the standard deviation, the second highest maximum value is stored.

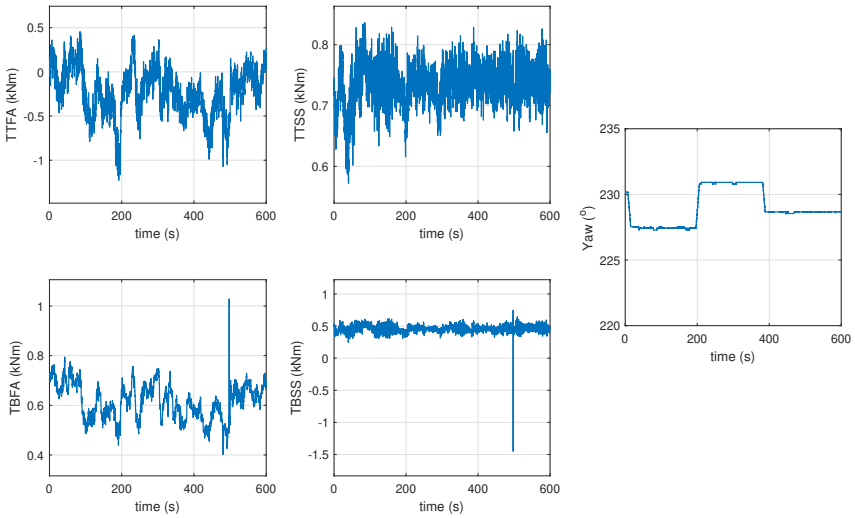

Figure 7.15: Tower moment time series - an error in maximum observed tower base fore-aft moment. All moments are normalized with the absolute maximum DLC 1.3 moment at rated wind speed.

In the available data set, the nearest found maximum value shows a peak in tower base fore-aft as well as the tower top fore-aft (Figure 7.16). This maximum tower base fore-aft moment does not exceed DLC 1.3 results. Because of the unavailability of the other time series, no further analysis is performed.

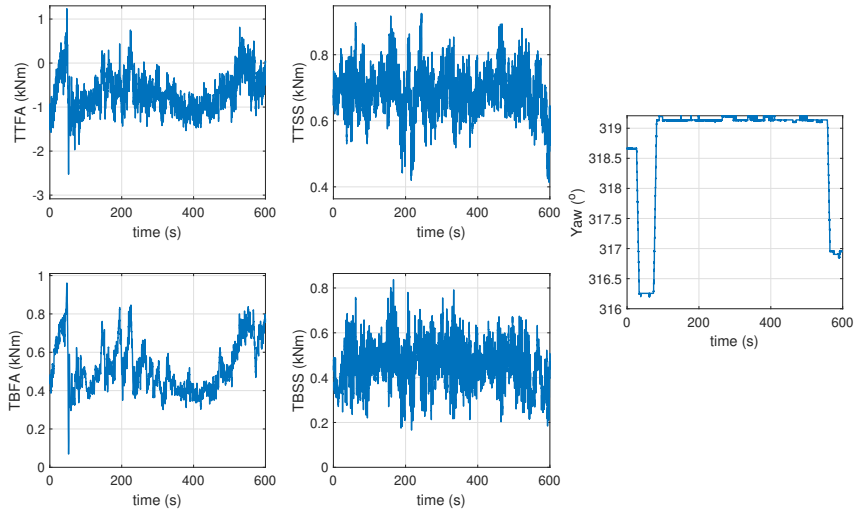

Figure 7.16: Tower moments and yaw angle time series. All moments are normalized with the absolute maximum DLC 1.3 moment at rated wind speed.

7.4. Discussions

In this chapter, the influence of wind power and wind speed ramp events on the ultimate loads were analysed and compared with DLC 1.3. Then, high-frequency (25 Hz) time series of various parameters in the selected time interval were examined, and some of them were also compared with the simulation time series to understand the reason for the discrepancies. The findings from the above results are summarised as follows:

- **Wind speed and wind power ramp events on 10-min basis**
  The loads associated with **power ramps** were clustered in region 2, mainly due to the non-linearity of the power curve (see Figure 2.5). It is observed that the average of these loads per wind speed bin is almost equal to the average of the whole measurements. It can be concluded that the power ramps do not affect the ultimate wind turbine loads.

  On the other hand, the loads related to **wind speed ramps** were more evenly distributed and could be an extreme load inducing factor in the region 2. This also suggests that the **wind power ramps** associated with large wind speed changes also influence the maximum loads in the region 2. However, for the higher wind speed bins, the average of measurements and the ramp-related load closely followed.

  Wind turbines, however, are designed to withstand the maximum loads during their lifetime. Therefore, it could be deduced from the Figure 7.1 that neither speed nor speed ramps affect the ultimate blade moments. In both cases, moments were relatively low around the rated speed. It could be due to the longer duration of ramp events that can be dealt with pitch controller. It should be noted that the above conclusions are based on the comparison of the average load profiles.

- **Extreme wind speed fluctuations**
  Ramp structures related to the extreme 10-min horizontal wind speed standard deviations, exceeding IEC ETM guidelines showed a significant impact on the maximum (minimum for blades) bending moments in the regions 2 and 3, yet, not in the region $2\frac{1}{2}$, which could also be due to the increased controller activities.

  The tower side-side moments, induced by the extreme fluctuation events exceeding IEC ETM Class B, outperformed DLC 1.3 simulations. In contrast, the constrained simulations of Hannesdóttir et al. [13] lead to tower base fore-aft and blade root flap-wise moments.It should be noted that the site conditions, simulation environment, turbine parameters, and designed controller may be different and lead to different results. Also, in Hannesdóttir et al. [13], the author used six seeds representing extreme 10-year standard deviations of met mast readings, whereas only 8-10 months of SCADA data is available for this report.

- **High-frequency** The high-frequency analysis of the **blade root flap-wise moments** time series revealed that the extreme bending moments per wind speed bin are mainly caused by the sudden transition of pitch angle from inactive to active region. Therefore, extreme loads over the wind speed range, except in region $2\frac{1}{2}$ (and close to it), were governed by ETM or ramp events that lead to pitch transition. In region $2\frac{1}{2}$, extreme loads have resulted from lower fluctuations, but are higher than NTM. Moreover, the increased fluctuations which occurred when the pitch was active did not result in high loads. Therefore, for the ultimate load analysis, the wind speed time series of the simulation model should involve a sudden transition of a pitch from inactive to active region.

  The DLC 1.3 model showed a similar response for these conditions, yet further analysis of other wind speed bins is required. Moreover, the NTM model may needs to be improved for representing high fluctuations in the wind time series, especially near the $2\frac{1}{2}$ transition region.

8

Conclusions and Recommendations

Understanding the impact of unexpected extreme changes in wind speed on the OWT components and wind farm performance is of paramount importance for the growth of the offshore wind industry. One of the extreme conditions are ramp events in power and wind speed. Based on the comprehensive literature review, this report has worked towards the following primary objective:

"to investigate the impact of wind-induced ramp events on offshore wind farm power and ultimate wind turbine loads - a measurement-based approach"

For this thesis, the required data sets were provided by SGRE. Two years of 10-min SCADA data of the two wind farms, WMR and Dudgeon, were analysed for the detection and categorisation of wind power ramp events. However, because of the limited data availability and shortness of time, the ultimate load analysis was conducted only for turbine D40 of the Dudgeon wind farm. In addition, aeroelastic simulation results of normal and extreme turbulence load cases were available from BHawC.

This chapter summarises the research findings of this report. Subsequently, some recommendations are proposed based on the data processing during this thesis. Finally, the probable scope of future research is discussed.

8.1. Concluding remarks

After a comprehensive literature review of existing research work and the analysis of the available datasets, the results are summarised in the following steps:

Detection and categorization of wind power ramp events of two wind farms

With the objective of detecting and categorizing wind-induced ramp events on two offshore wind farms, a comprehensive investigation of the ramp detection algorithm, based on the end-user's objective, was conducted. A suitable ramp detection definition was selected based on the available dataset and by considering the smoothing effect of power differences. In addition, the influence of power using two and the objective of identifying wind-induced power ramp events. The following questions were addressed while normalizing wind farm power:

- **"What is the effect of power normalization technique on the objective of an end-user ?"**
  As the variable capacity (available capacity) method eliminates the influence of wind turbine (or its data) availability, this would be an useful approach for wind turbine designers or other end users with a similar objective. On the other hand, for storage system designers, grid operators, or energy traders, the overall variation in power, irrespective of its cause would be more important. Thus, the nominal capacity method could be more appropriate. As the goal of this thesis was to analyse extreme wind-induced power ramp events, the variable capacity method was used.

- **"How does the criterion of the minimum number of turbines, i.e., data availability at each time step influences the ramp detection method?"**
  The smoothing effect of normalized wind farm power differences showed its depends on the minimum number of wind turbines and their positioning in the wind farm. Therefore, the criterion was selected such that the minimum number of turbines are representative of the area covered by the wind farm, and the possible combination of their positioning doesn't lead to a large variation in the threshold.

- **"How are the characteristics of detected wind power ramp events at two wind farms correlated?"**
  A good degree of correlation was observed between the signals of the two wind farms and in the detected large-scale ramp events. The time lag (or advance) between the observed ramp events was close to the calculated value form mean wind speed and direction at each wind farm. However, it is not always possible to predict the characteristics of the events based on SCADA data. Detailed meteorological information from Numerical Weather Prediction models, weather charts, nearby upstream meteorological masts or LiDAR is needed for thorough analysis.

  Both wind farms experienced ramps of nearly similar characteristics. The variation of ramp-up and ramp-down events w.r.t. the change in speed, direction, turbulence, and ramp duration showed decreasing trend with increasing characteristic changes. The primary reason could be the non-linearity of the power curve. The large changes could be associated with the large length and temporal scale weather phenomena, which are less frequent in the atmosphere. However, because the Dudgeon wind farm is larger than WMR in size and consists of more wind turbines, it has faced events of longer duration, higher speed, and direction changes.

Analysis of the impact of wind power and wind speed ramp events on the maximum wind turbine loads

Regarding the influence of wind-induced ramp events on OWT loads, a detailed investigation is conduced on the blade and tower moments of turbine D40 of the Dudgeon wind farm. It is worth mentioning that the initial comparison of BHawC simulation results showed a good agreement with the measurements. Therefore, the obtained results do not involve any significant uncertainties. The deductions of the analysis are listed as follows:

- **Wind speed and wind power ramps on 10-min basis:**
  The loads associated with wind **power ramps** were clustered in the partial load region due to the non-linearity of the power curve. The average of these loads was found similar to the average of all measurements per wind speed bin. Based on the analysis of average loads, wind power ramps do not affect the ultimate wind turbine loads.

  Conversely, the loads related to **wind speed ramps** were distributed over the wind speed range. Moreover, they could be extreme load drivers in the partial load region before the activation of pitch controller. Yet, not at high wind speed bins. It also implies that the **wind power ramps** associated with large wind speed changes also influence the maximum loads in the same region.

- **Extreme wind speed fluctuations:**
  The extreme fluctuations are the events that exceed the prescribed IEC extreme turbulence model per wind speed bin. These events were found to be the extreme load drivers in the partial load region (when the pitch was inactive) and after rated wind speed. Yet, not near rated wind speed region, which could be due to the longer time duration of events that could be dealt by the controller.

Validation of Hannesdóttir *et al.* [13] findings by comparing measured loads associated with extreme fluctuations to DLC 1.3:

In Hannesdóttir et al. [13], constrained simulations of tower base fore-aft and blade root flap-wise moments exceeded the DLC 1.3 simulations. In contrast, the measured tower side-side moments, caused by the extreme fluctuation events exceeding the IEC ETM Class B, outperformed the DLC 1.3 results. This can be due to the wind-wave misalignment. However, the associated blade root flap-wise and tower base fore-aft moments were well under the prediction of DLC 1.3. Since these ramp events involved comparatively longer duration and lower fluctuations, the controller could handle these events. Moreover, based on the findings of this report, if the no-ramp region in the ramp-like wind speed time series involves high stationary turbulence (but close to NTM), demanding a sudden activation of the pitch controller, it could exceed DLC 1.3 loads per wind speed bin.

It should be noted that the site conditions, simulation environment, turbine parameters, and designed controller may be different and lead to different results. Also, in Hannesdóttir et al. [13], the author used six seeds representing extreme 10-year standard deviations of met mast readings, whereas only 8-10 months of SCADA data is available for this report.

Analysis of high-frequency time series:

The investigation of high-frequency time series of **blade root flap-wise moments** revealed that the extreme bending moments per wind speed bin were mainly caused by a sudden transition of pitch angle from inactive to the active region. Therefore, extreme loads over the wind speed range, except near rated wind speed region, were governed by ETM or ramp events which lead to the pitch transition. Near rated wind speed, extreme loads have resulted from lower fluctuations with standard deviation close to NTM but relatively higher fluctuation frequency and amplitude. Moreover, the higher fluctuations that occurred during the active pitch did not result in large loads. Thus, for the ultimate load analysis, the wind speed time series of the simulation model must involve a sudden transition of a pitch controller from inactive to the active region or vice versa.

An analysis of one of the ETM wind speed time series showed a similar response to the measurement. Yet, further investigation of time series in other wind speed bins is required. Moreover, the NTM model needs to be improved for representing high fluctuations in the wind time series, especially near the $2\frac{1}{2}$ transition region.

8.2. Recommendations

- **Meteorological information:**
  Local effect of the detected weather event were difficult to analyse from the weather charts and provided SCADA data. Detailed meteorological information from the numerical weather prediction models, high resolution weather charts, nearby upstream meteorological masts or LiDAR is needed for thorough analysis. The information is vital to obtain the relation between the observed ramp events at two wind farms or to examine any deviation from the expected norm.

- **Analysis of extreme characteristics events:**
  In chapter 7, the influence of wind power and wind speed ramps are analysed on a 10-min basis. However, the indicator function shows ramps of unique characteristics as similar. Therefore, the influence of different characteristics of ramps events, such as higher wind speed, direction changes or large-scale events, should be analysed. One could also examine the characteristics of loads associated with the extreme 1% ramp events per wind speed bin.

- **Data filtering:**
  Most of the time has been spent on filtering the data set, yet maximum tower moments showed some errors. Thus, it is recommended to use an additional filter, i.e, if the difference between 10-min maximum (or minimum) and the 10-min average is higher than four or five times the 10-min standard deviation, that data could be rejected.

Moreover, additional checks can be executed while storing the 10-min statistics from high-frequency data. For instance, if the difference between the two highest maxima in the 10-min interval is higher than the standard deviation, the lower maximum value should be stored. This ensures that not too much data is removed. Moreover, due to the high storage requirement, usually, high-frequency data is not available for all time periods. In such cases, it will not be possible to determine the underlying cause. Thus, the proposed filtering check would be useful.

8.3. Possible uncertainties in the results

Wind speed measurements:
The wind speed SCADA data was available from the cup anemometer measurements, which is mounted behind the rotor. Thus, the readings include added turbulence due to the blades passing in front of the tower. Thus, the analysis associated with standard deviation and turbulence intensity may deviate from reality.
Data availability:
The results are based on only 8-10 months of load measurements. Thus, the results do not even consider the seasonal variations. Besides, wind fluctuations are unpredictable, thus more years of data set would give better results.

8.4. Future scopes

- **Analysis of high-frequency events:**
  It is crucial to review the high-frequency time series of other bending moments, as this report has mainly focused on the blade root flap-wise moment. In order to identify the extreme load governing parameters in each wind speed bin, high-frequency data of extreme 2-3 events per wind speed bin could be analysed and the influencing parameters can be determined.

- **Modification of ETM:**
  Based on the findings, a sudden transition of pitch control from inactive to the active region and vice versa caused extreme loads in the below and above-rated wind speed regions. For this purpose, a simulation time series similar to the one presented in Figure 7.9 could be a good estimate. Nonetheless, other simulation time series should be analysed to understand the possible deviation and necessary modification.

- **Introduction of a new wind speed time series:**
  The extreme loads around rated wind speed that exceeded the DLC 1.3 loads were associated with a wind speed standard deviation close to the one from IEC NTM, but with higher fluctuation frequency. These loads also involved pitch transitions. Ramp-like wind speeds in combination with such turbulence (involving pitch transition) showed higher loads than the DLC 1.3 loads. An example of an observed event is shown in Figure 7.7. Therefore, such time series can be included in the DLC 1.3 simulations to estimate the possible extreme moments per wind speed bin.

- **Analysis of extreme blade root flap-wise moments:**
  The minimum blade root flap-wise moments was found to be influenced by a sudden wind speed fluctuation near rated wind speed causing the transition of the pitch controller from inactive to the active region. The comparison of PSD of measured and simulated generator rotational speed showed higher energy content in high frequency region.

  However, this also brings to the question of "why are these loads not driven by ETM?". Therefore, it is crucial to conduct thorough analyse on more of such events recommended to identify the primary reason. One-to-one simulations using the measured high-frequency time series may give useful results.

Bibliography

[1] Gwec: Offshore wind is estimated to surge to 234 gw by 2030. last accessed: 31/01/21. [Online]. Available: https://www.renewableenergyworld.com/wind-power/gwec-offshore-wind-is-estimated-to-surge-to-234-gw-by-2030/#gref.

[2] P. C. Kalverla, G.-J. Steeneveld, R. J. Ronda, and A. A. Holtslag, "An observational climatology of anomalous wind events at offshore meteomast ijmuiden (north sea)," Journal of Wind Engineering and Industrial Aerodynamics, vol. 165, pp. 86–99, 2017, ISSN: 0167-6105. DOI: https://doi.org/10.1016/j.jweia.2017.03.008. [Online]. Available: https://www.sciencedirect.com/science/article/pii/S0167610516307061.

[3] S. Sánchez, J.-S. López-Gutiérrez, V. Negro, and M. D. Esteban, "Foundations in offshore wind farms: Evolution, characteristics and range of use. analysis of main dimensional parameters in monopile foundations," Journal of Marine Science and Engineering, vol. 7, no. 12, p. 441, 2019.

[4] Working towards the world's first subsidy-free offshore wind farm, 2020. [Online]. Available: https://vattenfall-hollandsekust.nl/en/blog/2020/07/28/working-towards-the-worlds-first-subsidy-free-offshore-wind-farm/.

[5] A. B. Wilson, Offshore wind energy in europe, Nov. 2020.

[6] B. Consultancy, I. M. van den Brink, and M. de la Vieter, "Pathways to potential cost reductions for offshore wind energy," 2021.

[7] J. Carroll, A. McDonald, and D. McMillan, "Failure rate, repair time and unscheduled o&m cost analysis of offshore wind turbines," Wind Energy, vol. 19, no. 6, pp. 1107–1119, 2016. DOI: https://doi.org/10.1002/we.1887. eprint: https://onlinelibrary.wiley.com/doi/pdf/10.1002/we.1887. [Online]. Available: https://onlinelibrary.wiley.com/doi/abs/10.1002/we.1887.

[8] A. C. Way and G. Van Zijl, "A study on the design and material costs of tall wind turbine towers in south africa," Journal of the South African Institution of Civil Engineering, vol. 57, no. 4, pp. 45–54, 2015.

[9] P. Pinson, C. Chevallier, and G. N. Kariniotakis, "Trading wind generation from short-term probabilistic forecasts of wind power," IEEE Transactions on Power Systems, vol. 22, no. 3, pp. 1148–1156, 2007. DOI: 10.1109/TPWRS.2007.901117.

[10] Y. Gong, Q. Jiang, and R. Baldick, "Ramp event forecast based wind power ramp control with energy storage system," IEEE Transactions on Power Systems, vol. 31, no. 3, pp. 1831–1844, 2016. DOI: 10.1109/TPWRS.2015.2445382.

[11] R. Sevlian and R. Rajagopal, "Detection and statistics of wind power ramps," Power Systems, IEEE Transactions on, vol. 28, pp. 3610–3620, Nov. 2013. DOI: 10.1109/TPWRS.2013.2266378.

[12] C. Gallego-Castillo, A. Cuerva-Tejero, and O. Lopez-Garcia, "A review on the recent history of wind power ramp forecasting," Renewable and Sustainable Energy Reviews, vol. 52, pp. 1148–1157, 2015, ISSN: 1364-0321. DOI: https://doi.org/10.1016/j.rser.2015.07.154. [Online]. Available: http://www.sciencedirect.com/science/article/pii/S1364032115008011.

[13] Á. Hannesdóttir, M. Kelly, and N. Dimitrov, "Extreme wind fluctuations: Joint statistics, extreme turbulence, and impact on wind turbine loads. last accessed on 2/11/2020," Wind Energy Science, vol. 4, no. 2, pp. 325–342, 2019. DOI: 10.5194/wes-4-325-2019. [Online]. Available: https://wes.copernicus.org/articles/4/325/2019/.

[14] Y. H. Wan, "Analysis of wind power ramping behavior in ercot- nrel. last visited 16/11/2020," Mar. 2011. DOI: 10.2172/1009681.

[15] L. Bianco, I. V. Djalalova, J. M. Wilczak, J. Cline, S. Calvert, E. Konopleva-Akish, C. Finley, and J. Freedman, "A Wind Energy Ramp Tool and Metric for Measuring the Skill of Numerical Weather Prediction Models," Weather and Forecasting, vol. 31, no. 4, pp. 1137–1156, Aug. 2016. DOI: 10.1175/WAF-D-15-0144.1.

[16] N. Cutler, M. Kay, K. Jacka, and T. S. Nielsen, "Detecting, categorizing and forecasting large ramps in wind farm power output using meteorological observations and wppt. last visited 20/11/2020," Wind Energy, vol. 10, no. 5, pp. 453–470, 2007. DOI: https://doi.org/10.1002/we.235. eprint: https://www.onlinelibrary.wiley.com/doi/pdf/10.1002/we.235. [Online]. Available: https://www.onlinelibrary.wiley.com/doi/abs/10.1002/we.235.

[17] L. Valldecabres, L. von Bremen, and M. Kühn, "Minute-scale detection and probabilistic prediction of offshore wind turbine power ramps using dual-doppler radar," Wind Energy, vol. 23, no. 12, pp. 2202–2224, 2020. DOI: https://doi.org/10.1002/we.2553. eprint: https://onlinelibrary.wiley.com/doi/pdf/10.1002/we.2553. [Online]. Available: https://onlinelibrary.wiley.com/doi/abs/10.1002/we.2553.

[18] Y. Gong, Q. Jiang, and R. Baldick, "Ramp event forecast based wind power ramp control with energy storage system," IEEE Transactions on Power Systems, vol. 31, no. 3, pp. 1831–1844, 2016. DOI: 10.1109/TPWRS.2015.2445382.

[19] C. Kamath, Understanding wind ramp events through analysis of historical data. 2010, pp. 1–6.

[20] F. Vorpahl, H. Schwarze, T. Fischer, M. Seidel, and J. Jonkman, "Offshore wind turbine environment, loads, simulation, and design," Wiley Interdisciplinary Reviews: Energy and Environment, vol. 2, Sep. 2013. DOI: 10.1002/wene.52.

[21] J. Van Der Tempel, N. Diepeveen, W. De Vries, and D. Cerda Salzmann, "15 - offshore environmental loads and wind turbine design: Impact of wind, wave, currents and ice," in Wind Energy Systems, ser. Woodhead Publishing Series in Energy, J. D. Sørensen and J. N. Sørensen, Eds., Woodhead Publishing, 2011, pp. 463–478, ISBN: 978-1-84569-580-4. DOI: https://doi.org/10.1533/9780857090638.4.463. [Online]. Available: https://www.sciencedirect.com/science/article/pii/B9781845695804500156.

[22] B. He, S. Yang, and K. H. Andersen, "Soil parameters for offshore wind farm foundation design: A case study of zhuanghe wind farm," Engineering Geology, vol. 285, p. 106 055, 2021, ISSN: 0013-7952. DOI: https://doi.org/10.1016/j.enggeo.2021.106055. [Online]. Available: https://www.sciencedirect.com/science/article/pii/S0013795221000661.

[23] R. Stull, Meteorology for Scientists and Engineers. 2015. [Online]. Available: https://www.thoughtco.com/why-wind-gusts-3444339.

[24] I. E. Commission et al., Iec standards 61400-3, wind turbines part 3:design requirements for offshore wind turbines. edition 1, 2009.

[25] L. H. Holthuijsen, Waves in oceanic and coastal waters. Cambridge university press, 2010.

[26] T. Fischer, P. Rainey, E. Bossanyi, and M. Kühn, "Study on control concepts suitable for mitigation of loads from misaligned wind and waves on offshore wind turbines supported on monopiles," Wind Engineering, vol. 35, no. 5, pp. 561–573, 2011. DOI: 10.1260/0309-524X.35.5.561. [Online]. Available: https://doi.org/10.1260/0309-524X.35.5.561.

[27] C. Koukoura, "Validated loads prediction models for offshore wind turbines for enhanced component reliability," English, Ph.D. dissertation, 2014, ISBN: 978-87-92896-88-9.

[28] V. Sohoni, S. Gupta, and R. Nema, "A critical review on wind turbine power curve modelling techniques and their applications in wind based energy systems," Journal of Energy, vol. 2016, pp. 1–18, Jan. 2016. DOI: 10.1155/2016/8519785.

[29] C. B. E. Muljadi and B. Parsons, Characteristics of wind turbines under normal and fault conditions, Feb. 2007. [Online]. Available: https://www.nrel.gov/docs/fy07osti/41051.pdf.

[30] J. Jonkman, S. Butterfield, W. Musial, and G. Scott, "Definition of a 5-mw reference wind turbine for offshore system development," National Renewable Energy Lab.(NREL), Golden, CO (United States), Tech. Rep., 2009.

[31] A. Hwas and R. Katebi, "Wind turbine control using pi pitch angle controller," IFAC Proceedings Volumes, vol. 45, no. 3, pp. 241–246, 2012, 2nd IFAC Conference on Advances in PID Control, ISSN: 1474-6670. DOI: https://doi.org/10.3182/20120328-3-IT-3014.00041. [Online]. Available: https://www.sciencedirect.com/science/article/pii/S147466701631031X.

[32] M. Pichault, C. Vincent, G. Skidmore, and J. Monty, "Characterisation of intra-hourly wind power ramps at the wind farm scale and associated processes," Wind Energy Science, vol. 6, no. 1, pp. 131–147, Jan. 2021. DOI: 10.5194/wes-6-131-2021.

[33] V. Petrović and C. L. Bottasso, "Wind turbine envelope protection control over the full wind speed range," Renewable Energy, vol. 111, pp. 836–848, 2017, ISSN: 0960-1481. DOI: https://doi.org/10.1016/j.renene.2017.04.021. [Online]. Available: https://www.sciencedirect.com/science/article/pii/S0960148117303269.

[34] N. Lipman, E. Bossanyi, P. Dunn, P. Musgrove, G. Whittle, and C. Maclean, "Fluctuations in output from wind turbine clusters," Wind Engineering, vol. 4, no. 1, pp. 1–7, 1980, ISSN: 0309524X, 2048402X. [Online]. Available: http://www.jstor.org/stable/43749791.

[35] J. K. Seifert, M. Kraft, M. Kühn, and L. J. Lukassen, "Correlations of power output fluctuations in an offshore wind farm using high-resolution scada data," Wind Energy Science Discussions, vol. 2020, pp. 1–22, 2020. DOI: 10.5194/wes-2020-96. [Online]. Available: https://wes.copernicus.org/preprints/wes-2020-96/.

[36] A. R. Mehrens, A. N. Hahmann, X. G. Larsén, and L. von Bremen, "Correlation and coherence of mesoscale wind speeds over the sea," Quarterly Journal of the Royal Meteorological Society, vol. 142, no. 701, pp. 3186–3194, 2016. DOI: https://doi.org/10.1002/qj.2900. eprint: https://rmets.onlinelibrary.wiley.com/doi/pdf/10.1002/qj.2900. [Online]. Available: https://rmets.onlinelibrary.wiley.com/doi/abs/10.1002/qj.2900.

[37] H. Meng, F.-S. Lien, and L. Li, "Elastic actuator line modelling for wake-induced fatigue analysis of horizontal axis wind turbine blade," Renewable Energy, vol. 116, pp. 423–437, 2018, ISSN: 0960-1481. DOI: https://doi.org/10.1016/j.renene.2017.08.074. [Online]. Available: https://www.sciencedirect.com/science/article/pii/S0960148117308364.

[38] T. Knudsen, T. Bak, and S. Tabatabaeipour, "Detection of excessive wind turbine tower oscillations fore-aft and sideways," 2012 American Control Conference (ACC), pp. 5795–5800, 2012.

[39] M. Zaaijer and A. Viré, Introduction to wind turbines:physics and technology, 2019.

[40] A. N. Robertson, K. Shaler, L. Sethuraman, and J. Jonkman, "Sensitivity analysis of the effect of wind characteristics and turbine properties on wind turbine loads," Wind Energy Science, vol. 4, no. 3, pp. 479–513, 2019. DOI: 10.5194/wes-4-479-2019. [Online]. Available: https://wes.copernicus.org/articles/4/479/2019/.

[41] I. ISO, "2394: 2015_ general principles on reliability of structures," International Organization for Standardiz: Geneva, Switzerland, vol. 2019, 2015.

[42] B. R. Cheneka, S. J. Watson, and S. Basu, "A simple methodology to detect and quantify wind power ramps," Wind Energy Science, vol. 5, no. 4, pp. 1731–1741, 2020. DOI: 10.5194/wes-5-1731-2020. [Online]. Available: https://wes.copernicus.org/articles/5/1731/2020/.

[43] Á. Hannesdóttir and M. Kelly, "Detection and characterization of extreme wind speed ramps," Wind Energy Science last accessed 26/09/2020, vol. 4, no. 3, pp. 385–396, 2019. DOI: 10.5194/wes-4-385-2019. [Online]. Available: https://wes.copernicus.org/articles/4/385/2019/.

[44] C. Ferreira, J. Gama, L. Moreira-Matias, A. Botterud, and J. Wang, A survey on wind power ramp forecasting. last accessed on 15/09/2020, Jan. 2011. [Online]. Available: https://www.researchgate.net/publication/255041385_A_survey_on_wind_power_ramp_forecasting?enrichId=rgreq-e137626988bc159794c725d076629c77-XXX&enrichSource=Y292ZXJQYWdlOzI1NTA0MTM4NTtBUzoxODIzOTc4MzIyNzgwMTZAMTQyMDQ5ODQ0MDY0MA%5C%3D%5C%3D&el=1_x_2&_esc=publicationCoverPdf.

[45] L. Mahrt, "Eddy asymmetry in the sheared heated boundary layer. last accessed 31/10/2020," Journal of the Atmospheric Sciences, vol. 48, no. 3, pp. 472–492, Feb. 1991, ISSN: 0022-4928. DOI: 10.1175/1520-0469(1991)048<0472:EAITSH>2.0.CO;2. eprint: https://journals.ametsoc.org/jas/article-pdf/48/3/472/3425808/1520-0469(1991)048_0472_eaitsh_2_0_co_2.pdf. [Online]. Available: https://doi.org/10.1175/1520-0469(1991)048%3C0472:EAITSH%3E2.0.CO;2.

[46] P. Drobinski, R. a. Brown, P. H. Flamant, and J. Pelon, "Evidence of organized large eddies by ground-based doppler lidar, sonic anemometer and sodar. last accessed 31/10/2020," Boundary-Layer Meteorology, vol. 88, 1998, ISSN: 1573-1472. DOI: 10.1023/A:1001167212584. [Online]. Available: https://doi.org/10.1023/A:1001167212584.

[47] R. C. Foster, F. Vianey, P. Drobinski, and P. Carlotti, "Near-surface coherent structures and the vertical momentum flux in a large-eddy simulation of the neutrally-stratified boundary layer. last accessed on 30/10/2020," Boundary-Layer Meteorology, vol. 120, 2006, ISSN: 1573-1472. DOI: 10.1007/s10546-006-9054-8. [Online]. Available: https://doi.org/10.1007/s10546-006-9054-8.

[48] S. Wharton and J. K. Lundquist, "Assessing atmospheric stability and its impacts on rotor-disk wind characteristics at an onshore windfarm," Wind Energy, vol. 15, no. 4, pp. 525–546, DOI: https://doi.org/10.1002/we.483. eprint: https://onlinelibrary.wiley.com/doi/pdf/10.1002/we.483. [Online]. Available: https://onlinelibrary.wiley.com/doi/abs/10.1002/we.483.

[49] J. W. Zack, Optimization of wind power production forecast performance during critical periods for grid management, 2007. [Online]. Available: https://aws-dewi.ul.com/assets/AWEA_Windpower_2007_Forecasting.pdf.

[50] R. Oblack, What's a warm occlusion weather front? 2020. [Online]. Available: https://www.thoughtco.com/warm-occlusion-weather-front-3444337.

[51] I. Simmonds, K. Keay, and J. A. T. Bye, "Identification and climatology of southern hemisphere mobile fronts in a modern reanalysis," Journal of Climate, vol. 25, no. 6, pp. 1945–1962, 15 Mar. 2012. DOI: 10.1175/JCLI-D-11-00100.1. [Online]. Available: https://journals.ametsoc.org/view/journals/clim/25/6/jcli-d-11-00100.1.xml.

[52] Smitty, A frontal passage to remember. last accessed 12/10/2020, 2016. [Online]. Available: http://smittyswxupdate.blogspot.com/2016/11/a-frontal-passage-to-remember.html.

[53] D. K. Kwon, A. Kareem, and K. Butler, "Gust-front loading effects on wind turbine tower systems," Journal of Wind Engineering and Industrial Aerodynamics, vol. 104-106, pp. 109–115, 2012, 13th International Conference on Wind Engineering, ISSN: 0167-6105. DOI: https://doi.org/10.1016/j.jweia.2012.03.030. [Online]. Available: http://www.sciencedirect.com/science/article/pii/S0167610512000876.

[54] J. Yang, L. Fang, D. Song, M. Su, X. Yang, L. Huang, and Y. H. Joo, "Review of control strategy of large horizontal-axis wind turbines yaw system," Wind Energy, vol. 24, no. 2, pp. 97–115, DOI: https://doi.org/10.1002/we.2564. eprint: https://onlinelibrary.wiley.com/doi/pdf/10.1002/we.2564. [Online]. Available: https://onlinelibrary.wiley.com/doi/abs/10.1002/we.2564.

[55] J. Freedman and J. Zack, Identifying ramp events, 2012. [Online]. Available: https://www.wind-watch.org/documents/identifying-ramp-events/.

[56] C. Gallego, A. Costa, and A. Cuerva, "Improving short-term forecasting during ramp events by means of regime-switching artificial neural networks," Advances in Science and Research, vol. 6, no. 1, pp. 55–58, 2011. DOI: 10.5194/asr-6-55-2011. [Online]. Available: https://asr.copernicus.org/articles/6/55/2011/.

[57] H. Zheng and A. Kusiak, "Prediction of wind farm power ramp rates: A data-mining approach," Journal of Solar Energy Engineering last accessed 25/09/2020, vol. 131, no. 3, Jul. 2009, 031011, ISSN: 0199-6231. DOI: 10.1115/1.3142727. eprint: https://asmedigitalcollection.asme.org/solarenergyengineering/article-pdf/131/3/031011/5714033/031011_1.pdf. [Online]. Available: https://doi.org/10.1115/1.3142727.

[58] A. Bossavy, R. Girard, G. Kariniotakis, and S. A. France, "Forecasting uncertainty related to ramps of wind power production.," Journal of Climate and Applied Meteorology, pp. 1184–1195, 2010. [Online]. Available: https://hal-mines-paristech.archives-ouvertes.fr/hal-00765885/document.

[59] C. Gallego, A. Costa, Á. Cuerva, L. Landberg, B. Greaves, and J. Collins, "A wavelet-based approach for large wind power ramp characterisation," Wind Energy, vol. 16, no. 2, pp. 257–278, 2013. DOI: https://doi.org/10.1002/we.550. eprint: https://onlinelibrary.wiley.com/doi/pdf/10.1002/we.550. [Online]. Available: https://onlinelibrary.wiley.com/doi/abs/10.1002/we.550.

[60] B. R. Cheneka, S. J. Watson, and S. Basu, "A simple methodology to detect and quantify wind power ramps. last accessed 3/11/2020," Wind Energy Science Discussions, vol. 2020, pp. 1–12, 2020. DOI: 10.5194/wes-2020-64. [Online]. Available: https://wes.copernicus.org/preprints/wes-2020-64/.

[61] J. Zhang, M. Cui, B.-M. Hodge, A. Florita, and J. Freedman, "Ramp forecasting performance from improved short-term wind power forecasting over multiple spatial and temporal scales," Energy, vol. 122, pp. 528–541, 2017, ISSN: 0360-5442. DOI: https://doi.org/10.1016/j.energy.2017.01.104. [Online]. Available: https://www.sciencedirect.com/science/article/pii/S0360544217301111.

[62] D. Gan and D. P. Ke, "Wind power ramp forecasting based on least-square support vector machine," in Energy Engineering and Environment Engineering, ser. Applied Mechanics and Materials, vol. 535, Trans Tech Publications Ltd, May 2014, pp. 162–166. DOI: 10.4028/www.scientific.net/AMM.535.162.

[63] C. Gallego, A. Costa, and A. Cuerva, "Improving short-term forecasting during ramp events by means of regime-switching artificial neural networks," Advances in Science and Research, vol. 6, no. 1, pp. 55–58, 2011. DOI: 10.5194/asr-6-55-2011. [Online]. Available: https://asr.copernicus.org/articles/6/55/2011/.

[64] N. Dimitrov, A. Natarajan, and J. Mann, "Effects of normal and extreme turbulence spectral parameters on wind turbine loads," Renewable Energy, vol. 101, pp. 1180–1193, 2017, ISSN: 0960-1481. DOI: https://doi.org/10.1016/j.renene.2016.10.001. [Online]. Available: https://www.sciencedirect.com/science/article/pii/S0960148116308655.

[65] 4coffshore, Global offshore wind farm database. last accessed on 20 dec 2020. [Online]. Available: https://www.4coffshore.com/windfarms/.

[66] E. Gonzalez, B. Stephen, D. Infield, and J. J. Melero, "Using high-frequency scada data for wind turbine performance monitoring: A sensitivity study. last accessed on 31/10/2020," Renewable Energy, vol. 131, pp. 841–853, 2019, ISSN: 0960-1481. DOI: https://doi.org/10.1016/j.renene.2018.07.068. [Online]. Available: http://www.sciencedirect.com/science/article/pii/S0960148118308656.

[67] I. E. Commission et al., "Wind energy generation systems-part 3-1: Design requirements for fixed offshore wind turbines," International standard IEC, pp. 61 400–3, 2019.

[68] G. DNV, "Loads and site conditions for wind turbines," Standard DNVGL-ST-0437, Tech. Rep., 2016.

[69] M. Türk and S. Emeis, "The dependence of offshore turbulence intensity on wind speed," Journal of Wind Engineering and Industrial Aerodynamics, vol. 98, no. 8, pp. 466–471, 2010, ISSN: 0167-6105. DOI: https://doi.org/10.1016/j.jweia.2010.02.005. [Online]. Available: https://www.sciencedirect.com/science/article/pii/S0167610510000279.

[70] M. Petersen, T. Larsen, H. Madsen, and G. Larsen, "More accurate aeroelastic wind-turbine load simulations using detailed inflow information," Wind Energy Science, vol. 4, pp. 303–323, May 2019. DOI: 10.5194/wes-4-303-2019.

[71] A. DeMarco and S. Basu, "On the tails of the wind ramp distributions," Wind Energy, vol. 21, no. 10, pp. 892–905, 2018. DOI: https://doi.org/10.1002/we.2202. eprint: https://onlinelibrary.wiley.com/doi/pdf/10.1002/we.2202. [Online]. Available: https://onlinelibrary.wiley.com/doi/abs/10.1002/we.2202.

[72] D. L. Chandler, Explained: Sigma, 2012. [Online]. Available: https://news.mit.edu/2012/explained-sigma-0209.

[73] M. Office, Uk met office msl pressure charts. [Online]. Available: https://www.willandweather.org.uk/mycharts.php.

[74] A. C. Fitch, "Climate impacts of large-scale wind farms as parameterized in a global climate model," Journal of Climate, vol. 28, no. 15, pp. 6160–6180, 2015. DOI: 10.1175/JCLI-D-14-00245.1. [Online]. Available: https://journals.ametsoc.org/view/journals/clim/28/15/jcli-d-14-00245.1.xml.

[75] P. Argyle, S. Watson, C. Montavon, I. Jones, and M. Smith, "Modelling turbulence intensity within a large offshore wind farm," Wind Energy, vol. 21, no. 12, pp. 1329–1343, 2018. DOI: https://doi.org/10.1002/we.2257. eprint: https://onlinelibrary.wiley.com/doi/pdf/10.1002/we.2257. [Online]. Available: https://onlinelibrary.wiley.com/doi/abs/10.1002/we.2257.

[76] M. Office, Coriolis effect. [Online]. Available: https://www.metoffice.gov.uk/weather/learn-about/weather/how-weather-works/coriolis-effect.

[77] I. E. Commission et al., Iec standards 61400-1, wind turbines part 1:design requirements. edition 3, 2005.

[78] W. Bierbooms, "Investigation of spatial gusts with extreme rise time on the extreme loads of pitch-regulated wind turbines. last accessed on 21/10/2020," Wind Energy, vol. 8, no. 1, pp. 17–34, 2005. DOI: 10.1002/we.139. eprint: https://onlinelibrary.wiley.com/doi/pdf/10.1002/we.139. [Online]. Available: https://onlinelibrary.wiley.com/doi/abs/10.1002/we.139.

[79] M. Kelly, S. J. Andersen, and Á. Hannesdóttir, "Statistical impact of wind-speed ramp events on turbines, via observations and coupled fluid-dynamic and aeroelastic simulations," Wind Energy Science, vol. 6, no. 5, pp. 1227–1245, 2021. DOI: 10.5194/wes-6-1227-2021. [Online]. Available: https://wes.copernicus.org/articles/6/1227/2021/.

[80] S. Grange, "Technical note: Averaging wind speeds and directions," Jun. 2014. DOI: 10.13140/RG.2.1.3349.2006.

[81] Meteorological wind directioin. [Online]. Available: http://tornado.sfsu.edu/geosciences/classes/m430/Wind/WindDirection.html.

[82] A. Estanqueiro, Smoothing effect of the wind generation fluctuations, Jan. 2009. DOI: 10.13140/RG.2.1.1117.2889.

A

Vector and Scalar Averaging Methods

Wind velocity is a vector quantity, i.e., a combination of wind speed (magnitude of a vector) and wind direction. Thus, the vector averaging method can be used to determine the average wind direction of wind farm at each time step. In this report, wind farm speed is determined using scalar averaging of the horizontal wind speed of each wind turbine. The approach is same as proposed by Grange and elaborated in this chapter.

Figure A.1 illustrates the horizontal velocity vector, V_H having magnitude u m/s. The wind direction is represented as per various coordinate systems. Here, ϕ_{POLAR} defines an angle w.r.t. polar coordinates, ϕ_{VECT} is the wind vector azimuth that gives the direction 'towards' which the wind is blowing (oceanographic sign convention), and ϕ_{MET} is the meteorological wind direction, i.e. the direction 'from' which the wind is blowing. In the figure, wind is blowing towards North-East direction (NE) (given by ϕ_{VECT}), and coming from South-West direction (SW) (given by ϕ_{MET}). The meteorological and the oceanographic coordinate systems measure angle in a clockwise direction starting from North direction in contrast to the polar coordinate system. Angle is measured in anticlockwise direction in polar coordinate system starting from east.

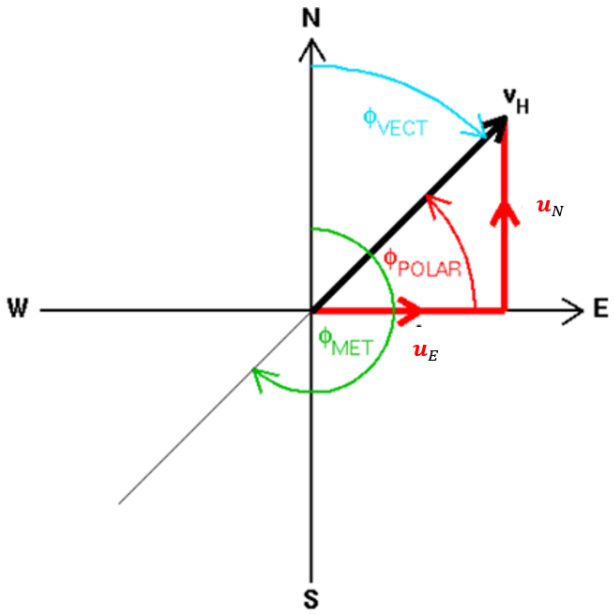

Figure A.1: Meteorological convention in coordinate system [81]

The wind direction data is available in meteorological sign convention, thus the equations are

formulated by using the meteorological coordinate system (similar as [81]). V_H can be decomposed into a velocity vector u_E, towards the east and u_N, towards north. Following aforementioned conventions, velocity component u_E can be calculated using ϕ_{VECT} as given in Equation A.1. since, angels ϕ_{VECT} and ϕ_{MET} have 180^o phase difference, u_E in terms of meteorological convention is estimated with Equation A.2.

$$u_E = u * \sin(\phi_{VECT}) \tag{A.1}$$

or

$$u_E = u * \sin(\phi_{MET} - 180) = -u * \sin(\phi_{MET}) \tag{A.2}$$

Similarly, u_N can be decomposed as

$$u_N = -u * \cos(\phi_{MET}) \tag{A.3}$$

For 'N' wind turbines, the average velocity vector in east and north directions are calculated using equations A.4 and A.5.

$$u_E = \frac{1}{N}\sum_{i=1}^{N} -u_i * \sin(\phi_{METi}) \tag{A.4}$$

$$u_N = \frac{1}{N}\sum_{i=1}^{N} -u_i * \cos(\phi_{METi}) \tag{A.5}$$

From equations A.4 and A.5, it is possible to determine the average wind direction using formula,

$$\phi_{MET} = \arctan(-u_E, -u_N) \tag{A.6}$$

As noticed from equations A.4 and A.5, vector averaging of the wind velocity depends on the wind directions. Consider a hypothetical situation at time t, where half of the wind turbines experience wind from the north direction and other half from the south. If the magnitudes of velocity vectors are same, say 10 m/s, then the average velocity will be 0. In reality, such conditions are unlikely to occur. However, this can not be true because the wind turbines generate power using yaw and pitch mechanisms. Grange, pointed out that vector averaging of wind speed can present atmospheric conditions poorly, and is always less than the scalar average of wind speed. Hence, scalar averaging method is preferred and the average wind speed of the wind farm is given by,

$$u_f(t) = \frac{1}{N}\sum_{i=1}^{N} u_i(t) \tag{A.7}$$

A good example for validating the application of preceding method follows.

Example:

Consider two turbines have wind speeds u_1 = 10 m/s and u_2 = 10 m/s. And wind directions are ϕ_{MET1} = 30^o and ϕ_{MET1} = 330^o.

- **Scalar average of wind speed:**

  Using equation A.7, for N = 2, u_f is 10 m/s

- **Vector average of wind speed:**

  Using equation A.4 and A.5, for N = 2, u_E is 0 m/s and u_N is - 8.67 m/s. Therefore, u_f is $\frac{1}{N}\sqrt{{u_E}^2 + {u_N}^2}$ = 8.67 m/s. As explained before, the resultant wind speed is lower than scalar averaged wind speed because of the difference in wind directions. Hence, the scalar averaging method is used.

- **Scalar average of wind direction:**

  When wind directions are averaged using the scalar approach, for N = 2, ϕ_{MET} is 180^o indicating south. This is due to the large difference in numbers 330^o and 30^o but both show direction close to north. Therefore, in reality, the average wind direction should be from the north direction.

- **Vector average of wind direction:**

  Using equation A.6, for N = 2, u_E = 0 m/s and u_N = - 8.67 m/s, ϕ_{MET} is 360^o(or 0^o). Thus, the vector averaging method gives a more precise wind direction.

For this report, each wind turbine is assumed as an individual turbine. Horizontal turbulence intensity of a turbine i at each time step is estimated using Equation A.8. Ultimately, turbulence intensity of the wind farm is taken as average of turbulence intensity at each wind turbine (Equation A.9). It should be noted that, here N indicates the active number of turbine at each time step similar to 'variable capacity method' (Equation 5.3).

$$TI_i(t) = \frac{\sigma_{ui}(t)}{u_i(t)} \tag{A.8}$$

$$TI_f(t) = \frac{1}{N}\sum_{i=1}^{N} TI_i(t) \tag{A.9}$$

B

Smoothing Effect of Power Fluctuations and Power Differences

B.1. Smoothing effect of power fluctuations

The power output of a turbine fluctuates over the year because of varying inflow conditions, incoming wind direction, location of a wind turbine in a farm (wake or free), the performance of wind turbine (yaw error, pitch error, efficiency of turbine parts), power curtailment and maintenance of an individual turbine. All in all, smoothing of fluctuation then depends on length scale, wind direction, and wind speed of the event as these parameters determine the travel time of the event through the wind farm (downstream wind turbines) [35].

Fluctuations in the power output time series of an individual turbine can be defined as:

$$p_i^{'} = P_i - \overline{P_i} \tag{B.1}$$

where $p_i^{'}$ represent fluctuations in power output time series (P_i) of wind turbine i, and $\bar{P}$ is an average of P_i. Therefore, standard deviation of the power output of turbine i is calculated as:

$$\sigma_{pi}^2 = \overline{(P_i - \overline{P_i})^2} \tag{B.2}$$

From Equation B.1, standard deviation of power output is nothing but the square of the average of power fluctuations, i.e., standard deviation of power fluctuations. i.e.,

$$\sigma_{pi}^2 = \overline{(p_i^{'})^2} \tag{B.3}$$

When powers of two wind turbines (i and j) are aggregated, standard deviation of the new power signal can be obtained similarly as for a single turbine.

$$p_{ij}^{'} = P_i + P_j - (\overline{P_i + P_j}) \tag{B.4}$$

$$p_{ij}^{'} = P_i + P_j - \overline{P_i} - \overline{P_j} \tag{B.5}$$

$$p_{ij}^{'} = p_i^{'} + p_j^{'} \tag{B.6}$$

$$\sigma_{pij}^2 = \overline{(p_i^{'} + p_j^{'})^2} \tag{B.7}$$

$$\sigma_{pij}^2 = \overline{(p_i^{'})^2} + \overline{(p_i^{'})^2} + 2\overline{p_i^{'} p_j^{'}} \tag{B.8}$$

Standard deviation of two aggregated power signals depends upon the correlation between them. The correlation coefficient measures the covariance between two signals normalized with their standard deviation, where covariance gives a directional relationship between two signals.

$$\mathrm{cov}(P_i, P_j) = \overline{p_i' p_j'} \tag{B.9}$$

Pearson's linear correlation coefficient can be given by,

$$r_{pij} = \frac{\mathrm{cov}(P_i, P_j)}{\sigma_{pi}\sigma_{pj}} \tag{B.10}$$

A correlation coefficient, r_{pij} between two signals i and j varies between -1 and 1, where value -1 indicates perfect opposite correlation (when one value increases the other decreases by the same amount), 1 shows perfect correlation and 0 represents the signals are uncorrelated.

Thus, Equation B.8 can be rewritten as:

$$\sigma_{pij}^2 = \sigma_{pi}^2 + \sigma_{pj}^2 + 2r_{pij}\sigma_{pi}\sigma_{pj} \tag{B.11}$$

Assuming same wind regimes at all the turbines, $\sigma_{pi} = \sigma_{pj} = \sigma_p$,i.e., standard deviations of power output signals of individual turbines are similar, even when different correlations are present [34]. It can be validated by calculating the standard deviation of power output for each turbine in a wind farm. Figure B.1 represents the standard deviation of the normalized power output for each turbine, which is normalized with rated power of a turbine. From these plots, it is clear that the standard deviation of each wind turbine is almost similar.

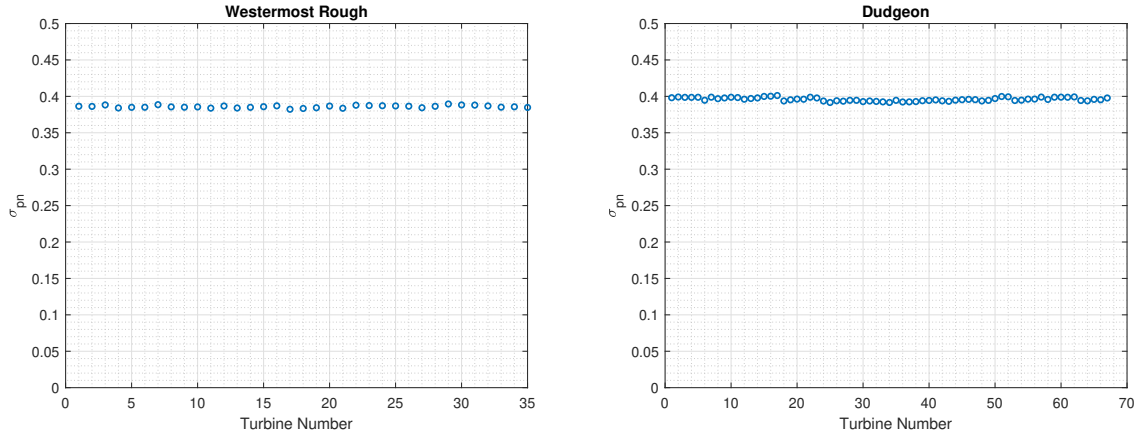

(a) WMR (b) Dudgeon

Figure B.1: Standard deviation of power fluctuation for each wind turbine

This the Equation B.11 will be,

$$\sigma_{pij}^2 = 2\sigma_p^2 + 2r_{pij}\sigma_p^2 \tag{B.12}$$

Extending the above formula for three turbines i, j and k

$$\sigma_{pijk}^2 = \sigma_p^2(3 + 2(r_{pij} + r_{jk} + r_{ik})) \tag{B.13}$$

and further for all N turbines of a wind farm

$$\sigma_{pf}^2 = \sigma_p^2(N + 2\sum_{i=1}^{N-1}\sum_{j=2}^{N} r_{pij}) \tag{B.14}$$

here, σ_{pf} provides the standard deviation of aggregated wind farm power.

$$\sigma_{pf}^2 = \sigma_p^2(N + N(N-1)\overline{r_{pij}}) \tag{B.15}$$

where $\overline{r_{pij}}$ is an average of all correlation coefficients and calculated as:

$$\overline{r_{pij}} = \frac{\sum_{i=1}^{N-1}\sum_{j=i+1}^{N} r_{pij}}{\frac{N(N-1)}{2}} \tag{B.16}$$

When wind turbines are located far apart, fluctuations in the power output associated with short term variations of wind speed are assumed to be independent. In other words, the power output of such turbines at that time instance are uncorrelated and largely cancel out [34]. From Equation B.15, overall standard deviation of uncorrelated wind turbines ($\overline{r_{pij}}$=0) will be $\sqrt{N}\sigma_p$, i.e., standard deviation of aggregated power only increases by $\sqrt{N}$. For normalized power, this standard deviation decreases by $\sqrt{N}$ as shown in Equation B.20 (In [82], equation 1 has an error, as it does not use normalized power).

It should be noted that each wind turbine's power is normalized by the rated power of a turbine, i.e., $P_n = \frac{P}{PR}$. Thus, normalized power fluctuation and its standard deviation a single turbine can be obtained from equations B.1 and B.3 as

$$p_{ni}^{'} = \frac{P_i - \overline{P_i}}{PR} \tag{B.17}$$

$$\sigma_{pn} = p_{ni}^{'} = \frac{\sigma_p}{PR} \tag{B.18}$$

Therefore, for a wind farm of N turbines with the same rated power, the standard deviation of normalized wind farm power fluctuations will be

$$\sigma_{pfn} = \frac{\sigma_p}{N.PR} \tag{B.19}$$

By dividing Equation B.15 by $N.PR$, relation between average correlation coefficient and standard deviation of normalized wind farm power fluctuations can be obtained as follows:

$$\sigma_{pfn} = \sigma_{pn}\sqrt{\frac{(1+(N-1)\overline{r_{pij}})}{N}} \tag{B.20}$$

where, σ_{pn} and σ_{pfn} indicate standard deviation of normalized power output of a single wind turbine and wind farm respectively.

As stated earlier, the standard deviation of normalized aggregated wind farm power (σ_{pfn}) for uncorrelated turbines decreases by $\sqrt{N}$, i.e., $\frac{\sigma_{pn}}{\sqrt{N}}$. Similarly, standard deviation for perfectly correlated turbines ($\overline{r_{pij}}$=1) in a wind farm will be same as a single turbine. In short, standard deviation of normalized wind farm power varies in the range,

$$\frac{\sigma_{pn}}{\sqrt{N}} \leq \sigma_{pfn} \leq \sigma_{pn} \tag{B.21}$$

.
Average correlation coefficients of wind farm power output for WMR and Dudgeon are found to be 0.96 and 0.97, respectively. This result corresponds to two years of power output data set. In conclusion, the standard deviation of wind farm power fluctuations and wind turbine power fluctuation is similar when considered yearly data set.

B.2. Smoothing effect of successive power differences

In subsection 5.1.3, three time standard deviation of successive power differences of normalized wind farm power signal is used to set a threshold value. Figure B.2 illustrates the difference between normalized power fluctuations ($P_n^{'}$) and normalized successive power differences (ΔP_n). Successive power difference at time t in a normalized power signal is evaluated as:

$$\Delta P_n(t) = P_n(t) - P_n(t-k) \tag{B.22}$$

where k is the sample time of the available data set. From Equation B.1, power differences are nothing but successive power fluctuation differences.

$$\Delta P_n(t) = p_n'(t) - p_n'(t-k) \tag{B.23}$$

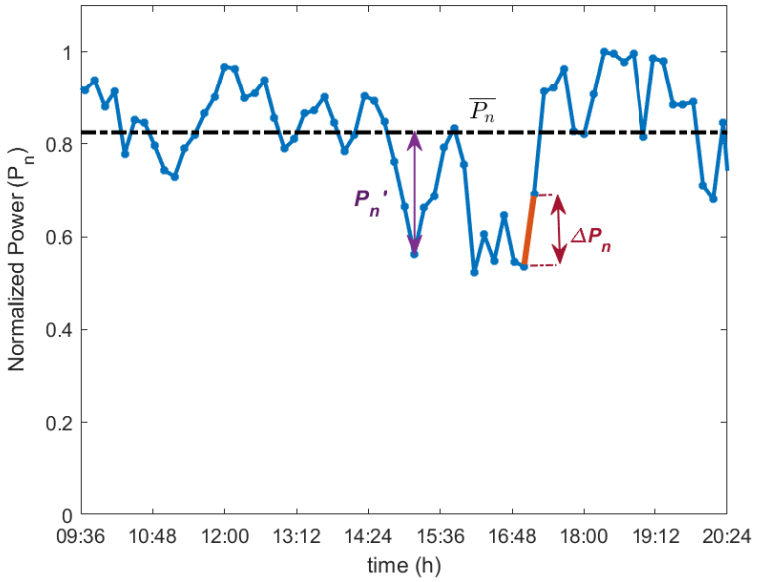

Figure B.2: Normalized power output time series of turbine D40, with average power ($\bar{P}_n$), power fluctuations ($P_n{}'$), and successive power differences (ΔP_n)

Therefore, normalized successive power differences time series show similar characteristics as normalized power fluctuations, i.e., $\overline{\Delta P_n} = 0$ and $\sigma(\Delta P_n) = (\overline{\Delta P_n})^2$. Similarly, standard deviation of normalized successive wind farm power differences can be estimated using Equation B.26

$$\sigma(\Delta P_{fn}) = \sigma(\Delta P_n)\sqrt{\frac{(1+(N-1)\overline{r(\Delta P)_{ij}})}{N}} \tag{B.24}$$

where,

$$\overline{r(\Delta P)_{ij}} = \frac{\sum_{i=1}^{N-1}\sum_{j=i+1}^{N} r(\Delta P)_{ij}}{\frac{N(N-1)}{2}} \tag{B.25}$$

If $\sigma(\Delta P_n)$ of all the turbines are close by but not equals to each other, the average of standard deviations ($\overline{\sigma(\Delta P_n)}$) can be used to estimate overall standard deviation.

$$\sigma(\Delta P_{fn}) = \overline{\sigma(\Delta P_n)}\sqrt{\frac{(1+(N-1)\overline{r(\Delta P)_{ij}})}{N}} \tag{B.26}$$

The estimated average correlation coefficients of successive power differences for WMR and Dudgeon are 0.35 and 0.31, respectively. These low correlation coefficients explain the high smoothing effect observed from the standard deviation of a single turbine to successive power difference of wind farm.

Power fluctuations indicate the variation in the wind farm power w.r.t. average wind farm power, whereas successive power differences depend on the value of fluctuation at each time step. A wind farm consists of several turbines, whose power output are affected by wake interaction, farm layout, spacial distance, length and time scale of meteorological phenomenon and individual wind turbine condition. Depending upon these parameters, weather events take time to pass through different

wind turbines. Besides, due to the difference in turbulence level, yaw or pitch angle at each turbine, the power output of all turbines are not the same at a specific time and show some time shift[35]. Thus, the standard deviation of successive power differences shows a higher smoothing effect. Yet, the correlation coefficient of power fluctuations also depends upon the period of data considered because of the observed seasonal pattern in power fluctuations and length scale of large-scale weather events.

B.3. Validation

In this section, result from Equation B.26 is validated with the standard deviation calculated using normalized power differences, which is considered as reference $(\sigma(\Delta P_{fn})_{ref})$. Figure B.3 demonstrates the flow chart of calculation steps used to estimate percentage deviation of the standard deviations obtained from Equation B.26.

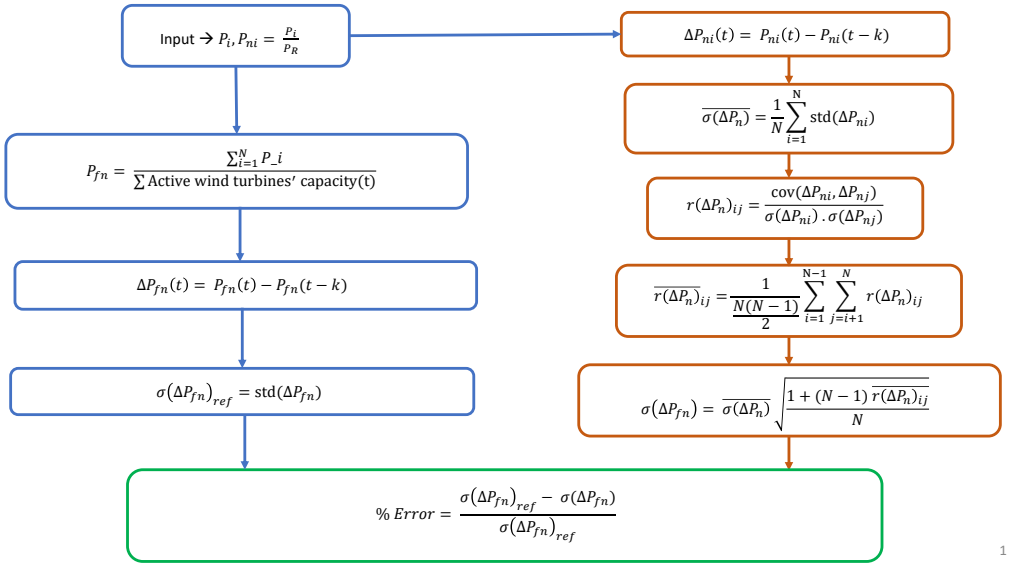

Figure B.3: Validation of derived standard deviation of normalized farm power differences (Equation B.26)

The validation is performed for both wind farms having $\sigma(\Delta P_{fn})_{ref}$ values 0.043 and 0.0386 respectively. The estimated standard deviations, 0.0415 and 0.0364 give percentage error of about 3.5% and 5.8% respectively. As the percentage error is small, $\overline{r(\Delta P)_{ij}}$ can be calculated using $\sigma(\Delta P_{fn})_{ref}$. It considerably reduces the time taken by N(N-1)/2 number of $r(\Delta P)_{ij}$ combination Equation B.25. Errors because time series are not continuous.

C

Additional Results

C.1. Introduction to 10-min statistics

Let us assume that the presented 10-min wind speed time series in Figure C.1 starts at 13:40 hours and ends at 13:50 hours. Then, all statistical values, i.e., average, minimum, maximum and standard deviations are stored at time 13:50 hours for the available system.

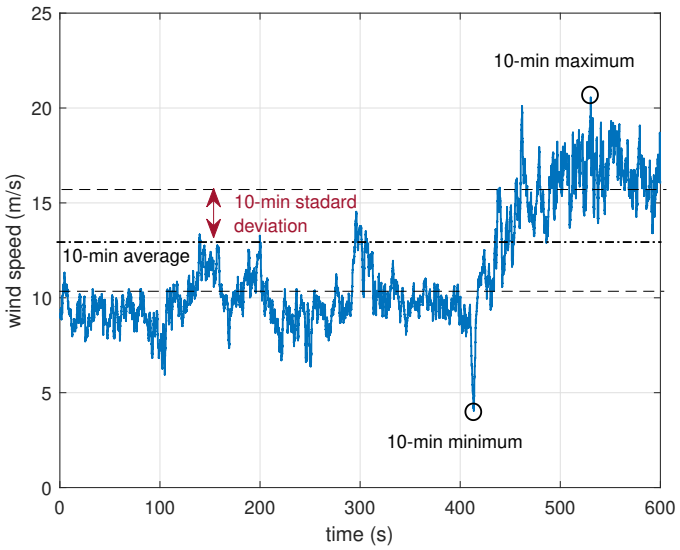

Figure C.1: Representation of 10-min statistics of available 10-min time series.

C.2. Correlation analysis

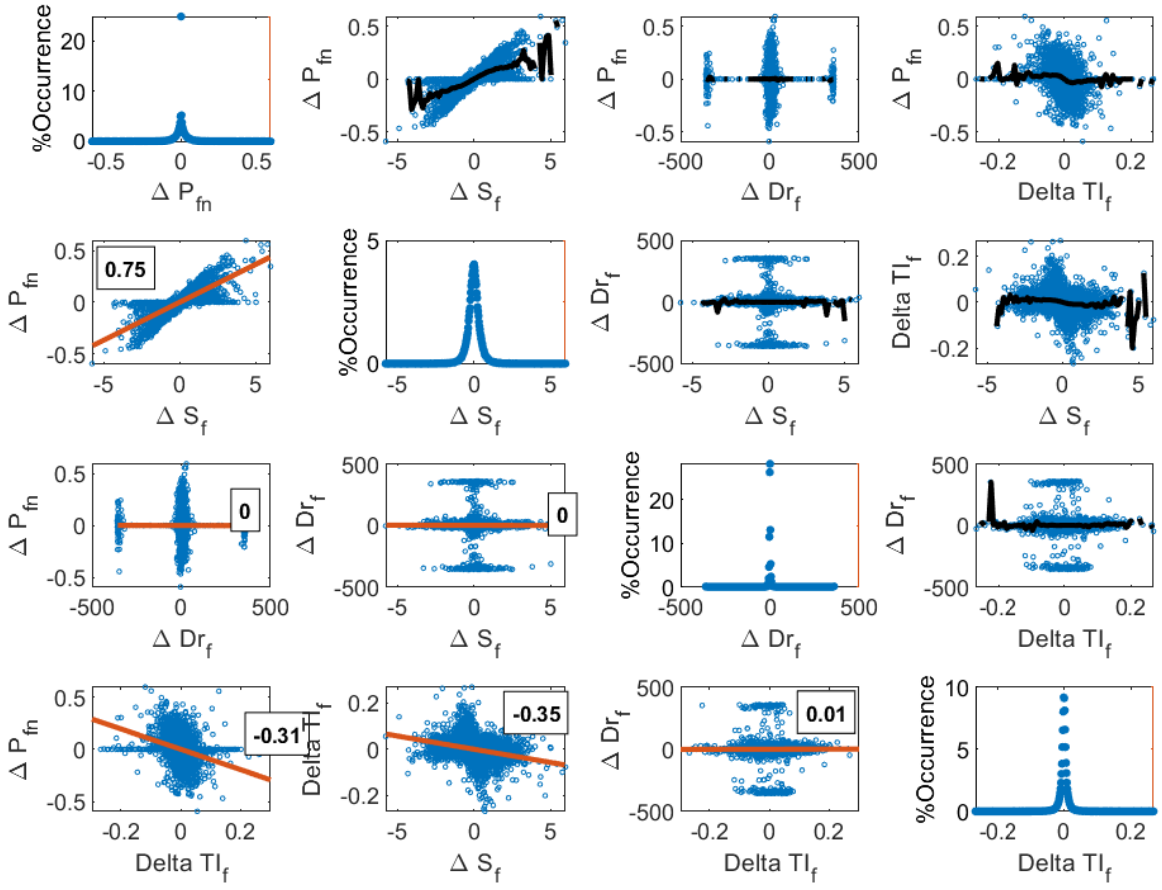

Figure C.2: Correlation matrix: Scattered plot of successive differences in WMR wind farm parameters with linear correlation (lower triangular), histograms(diagonal), nonlinear relation between parameters(upper triangular)

C.3. Weather Maps

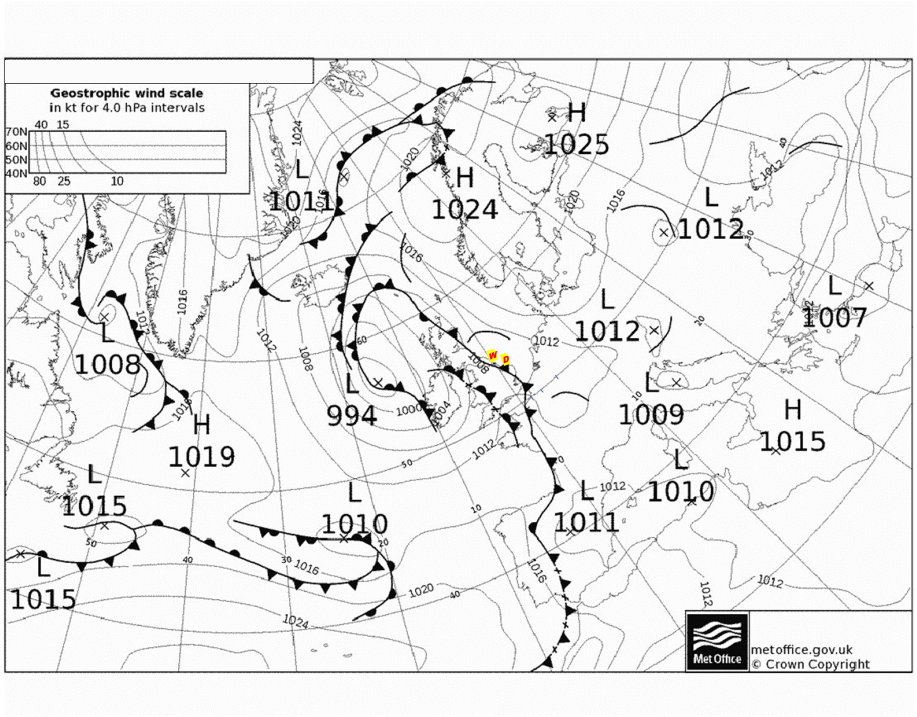

Figure C.3: Surface pressure charts of [73] UK at 00:06 UTC (day before). 'W' and 'D' represents the location of wind farm WMR and Dudgeon, respectively

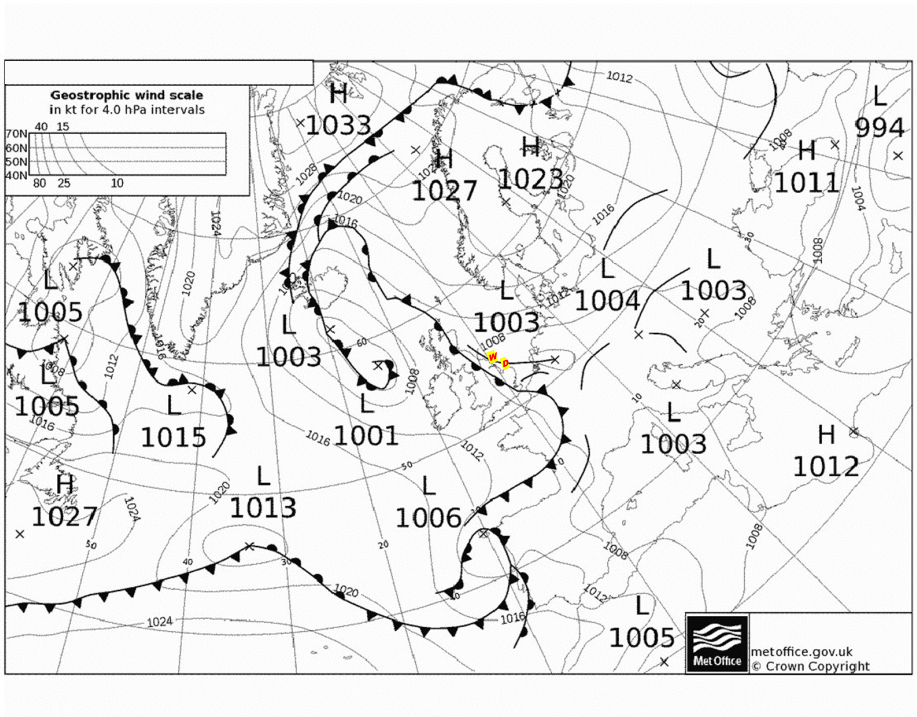

Figure C.4: Surface pressure charts of [73] UK at 00:06 UTC (day after). 'W' and 'D' represents the location of wind farm WMR and Dudgeon, respectively

C.4. Categorization of wind power ramp events

yearly variation plots

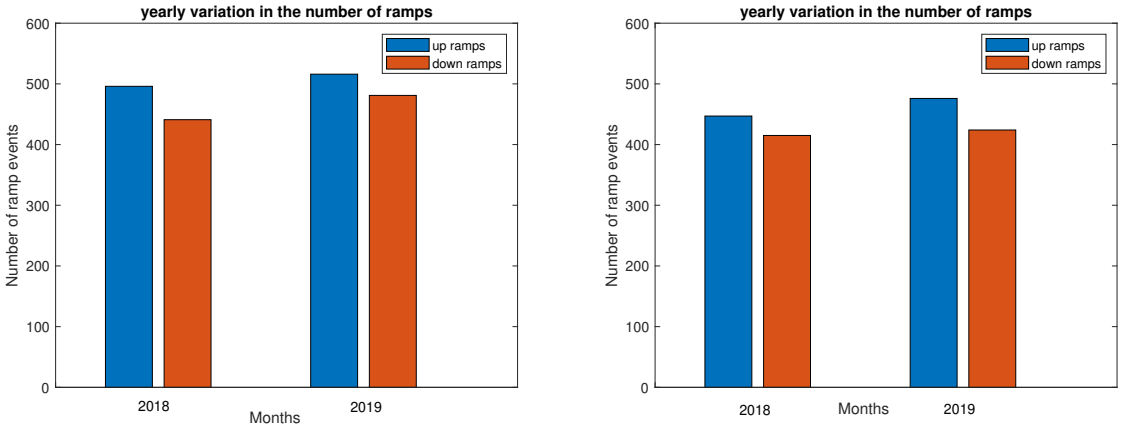

(a) WMR (b) Dudgeon

Figure C.5: Monthly variation of ramp-up and down events

monthly variation plots

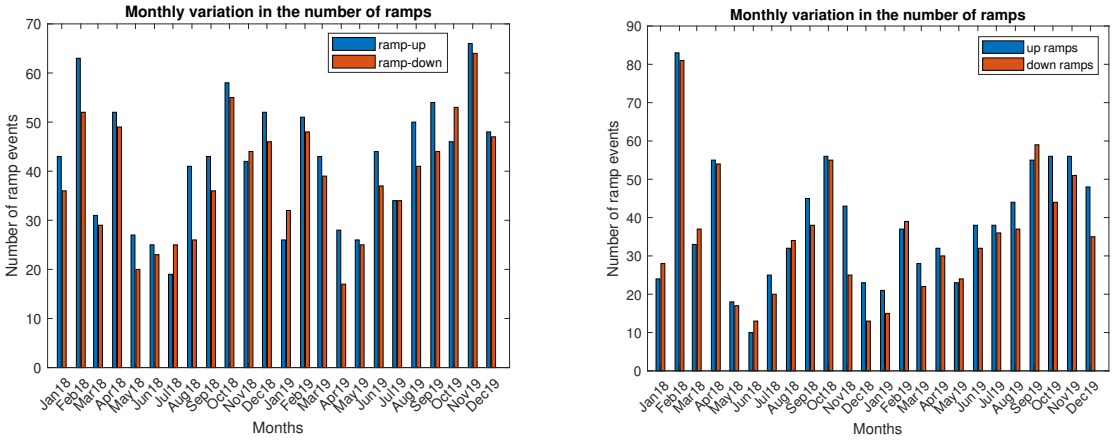

(a) WMR (b) Dudgeon

Figure C.6: Monthly variation of ramp-up and down events

Distribution of Δu_f of ramp events on power curve

Figure C.7 provides frequency distribution of start and end time of the ramp events on the power curve for different change wind speeds. Pichault, Vincent, Skidmore, and Monty has claimed that ramp events associated with $\Delta u_f < 3$ ms^{-1}, occur between speed 5 to 10ms^{-1}. It corresponds to the 40-90% rated speed range. For these plots, wind speeds are normalized with rated wind speed. Even though velocity values lie outside, peaks of the distribution appear close to the proposed range for $\Delta u_f < 3$ ms^{-1}. The ramp events at low wind speed changes occur below rated speed and are predominantly associated with the non-linearity of the power curve. Density distribution plots of the start and end times of the ramps are clustered closely. The distinct peak of the distribution starts separating as the difference in velocity increases. Ramps start near cut-in and end up to a maximum of 1.5 times the rated wind speed. Such a large increase in power and speed, meaning a good correlation between the turbine power and the possibility of mesoscale events.

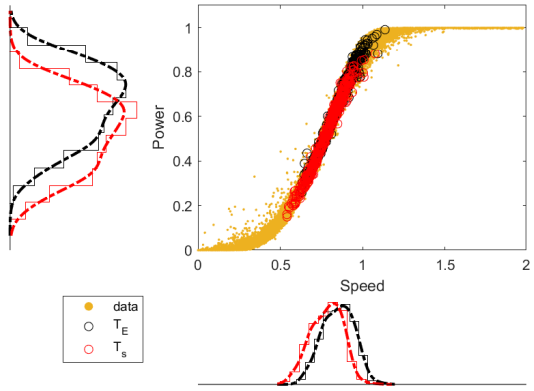

(a) $\Delta S <= 1$m/s

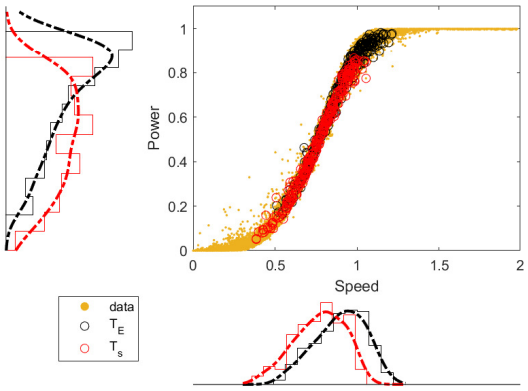

(b) $1 < \Delta S <= 2$m/s

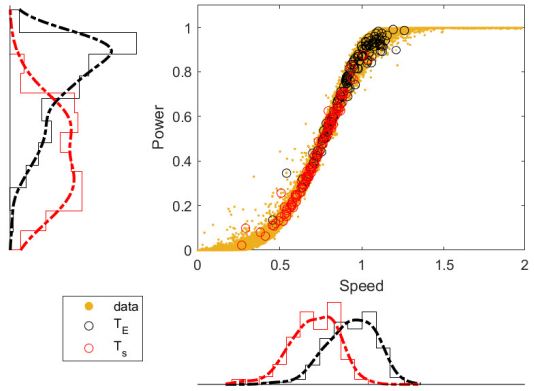

(c) $2 < \Delta S <= 3$m/s

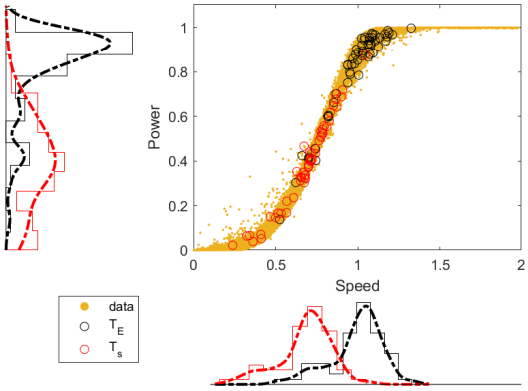

(d) $3 < \Delta S <= 4$m/s

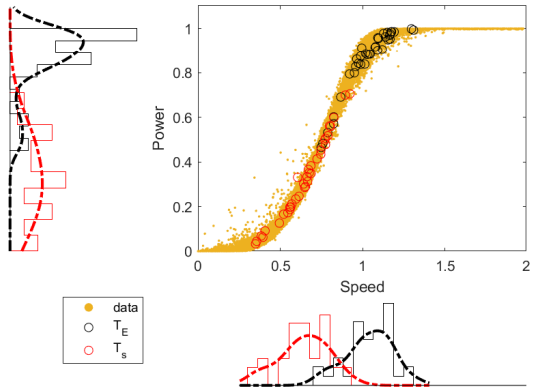

(e) $4 < \Delta S <= 5$m/s

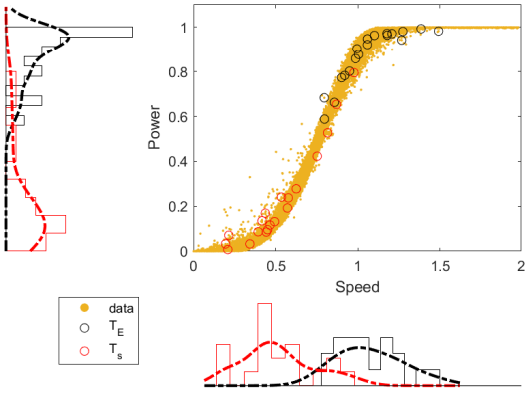

(f) $5 < \Delta S <= 10$m/s

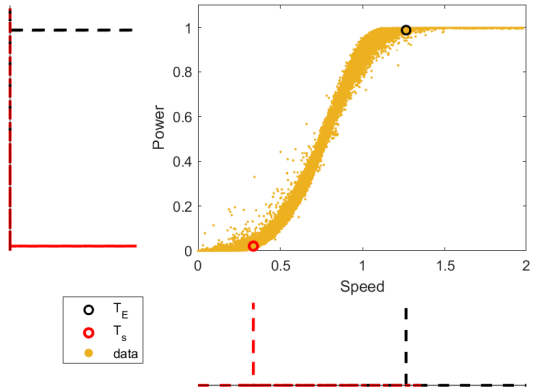

(g) $\Delta S > 10$ m/s

Figure C.7: Representation of start and end time of the observed ramp events on the power curve and corresponding density distribution.

C.5. DLC 1.2 validation

Figures C.8 and C.9 compares the 10-min average measured loads with 10-min average of DLC1.2. When pitch angle is inactive, the misalignment between chord length and rotor plane is insignificant. Therefore, 10-min average flap-wise moment follows thrust curve and edge-wise moment is resulted from tangential force.

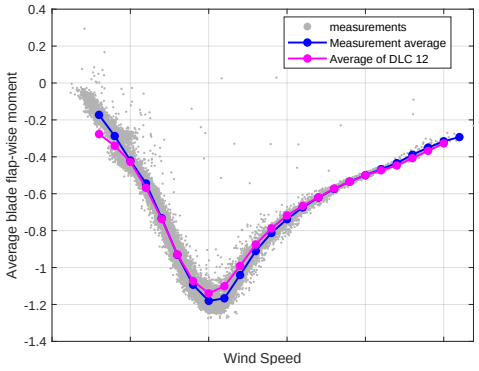

(a) Average blade root flap-wise moment

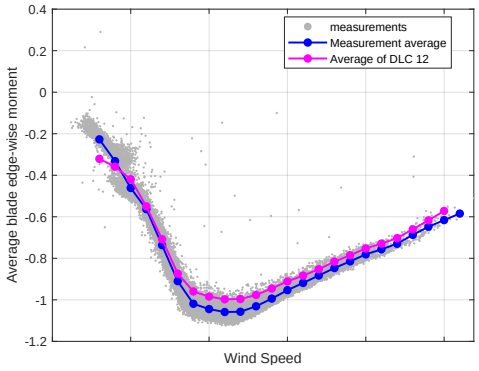

(b) Average blade root edge-wise moment

Figure C.8: Average blade root flap-wise and edge-wise moment of one blade. All moments are normalized with the minimum of average DLC 1.2 at the rated wind speed

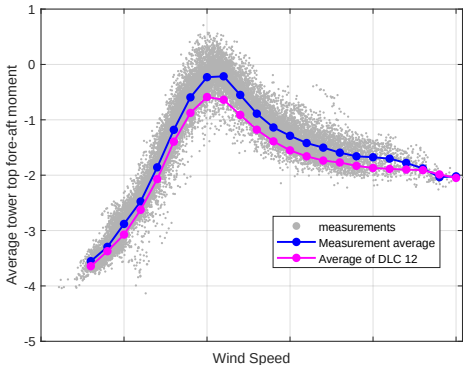

(a) Average tower top fore-aft moment

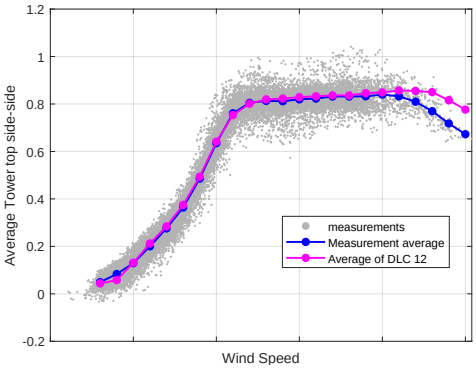

(b) Average tower top side-side moment

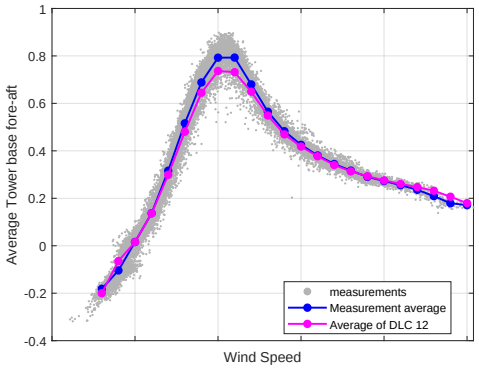

(c) Average tower base fore-aft moment

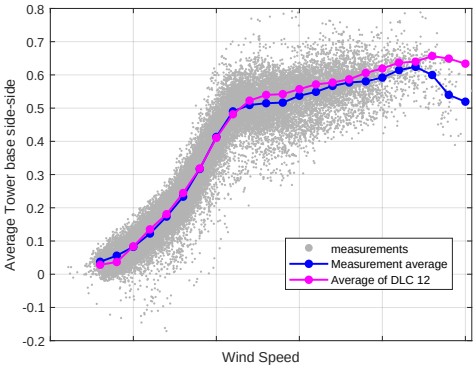

(d) Average tower base side-side moment

Figure C.9: Average tower top and tower base bending moments. All moments are normalized with the maximum of average DLC 1.2 at the rated wind speed

C.6. Wind power and speed ramps

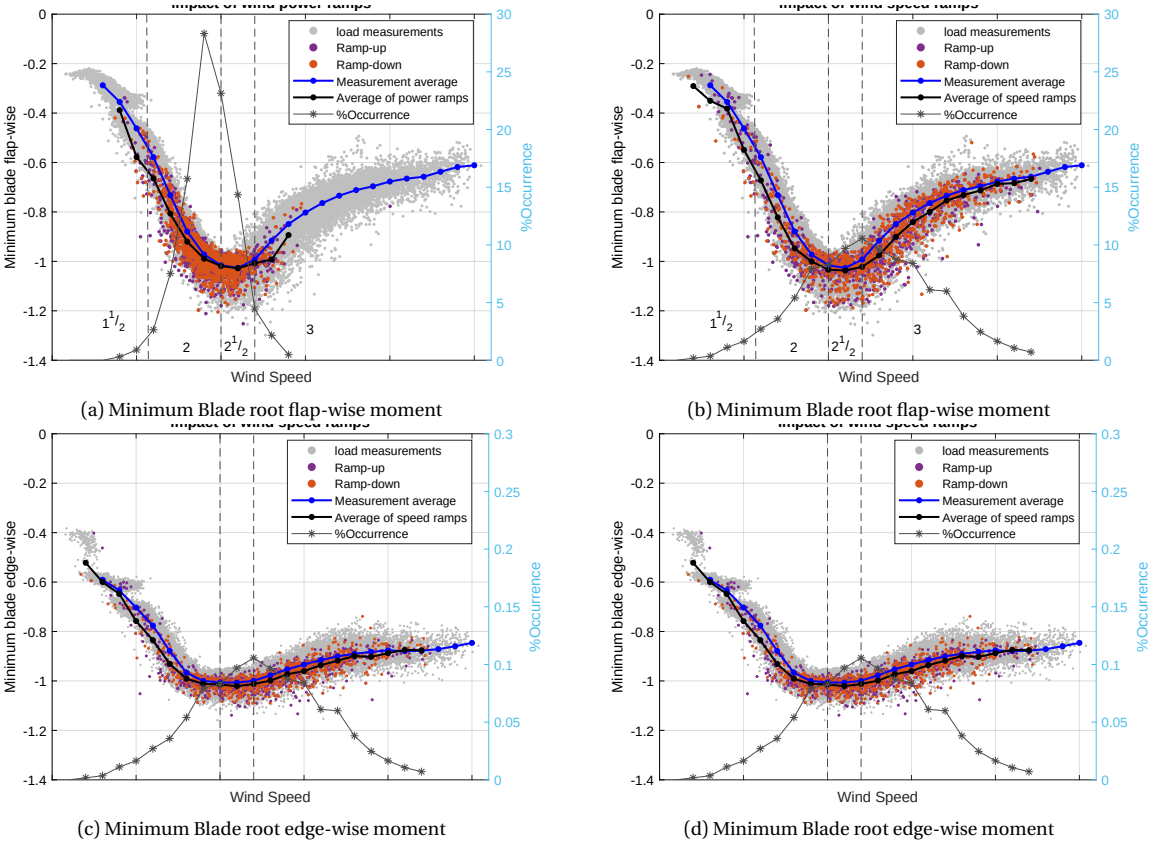

(a) Minimum Blade root flap-wise moment

(b) Minimum Blade root flap-wise moment

(c) Minimum Blade root edge-wise moment

(d) Minimum Blade root edge-wise moment

Figure C.10: Minimum blade root flap-wise and edge-wise moments. All moments are normalized with the respective minimum DLC 1.2 bending moment at the rated wind speed.

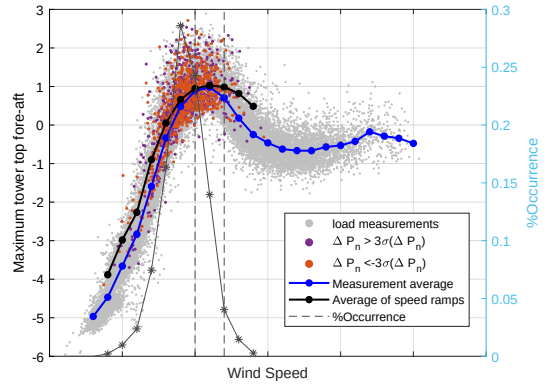

(a) Maximum Tower top fore-aft moment

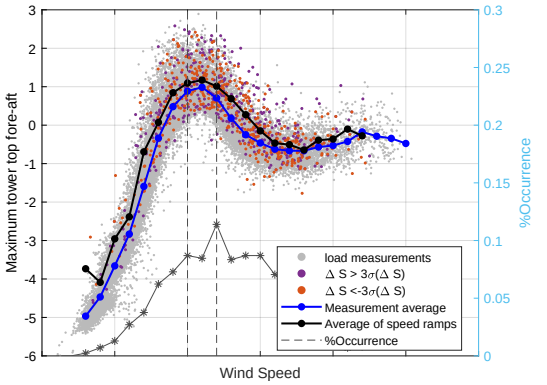

(b) Maximum Tower top fore-aft moment

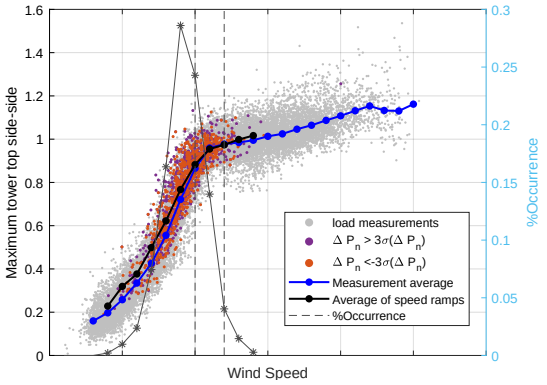

(c) Maximum Tower top side-side moment

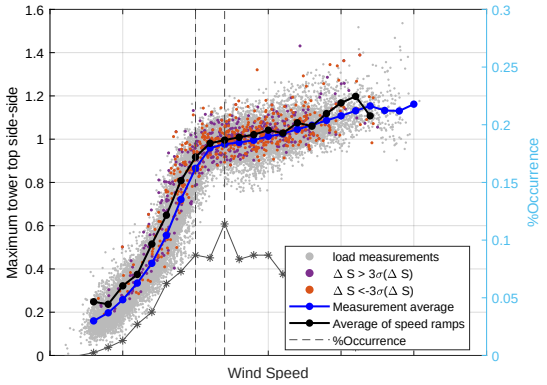

(d) Maximum Tower top side-side moment

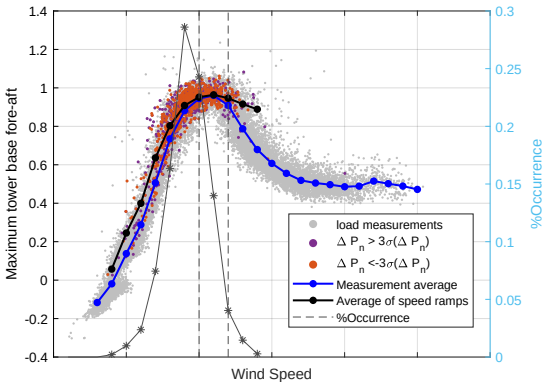

(e) Maximum Tower base fore-aft moment

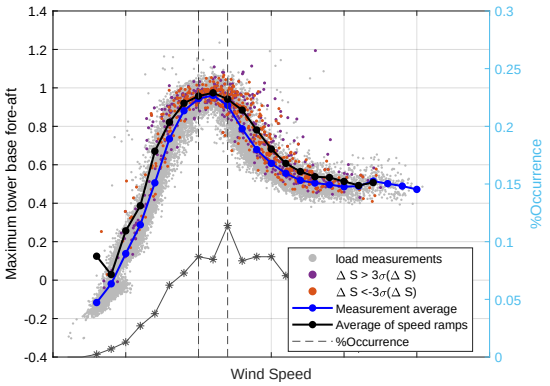

(f) Maximum Tower base fore-aft moment

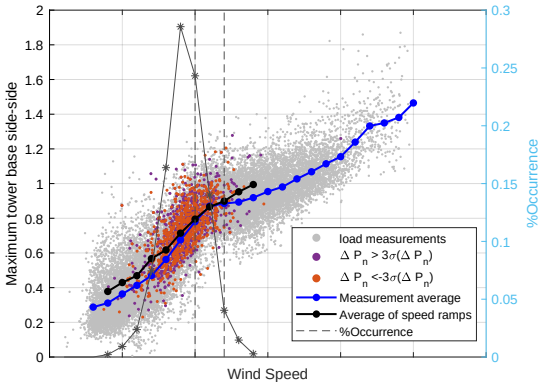

(g) Maximum Tower base side-side moment

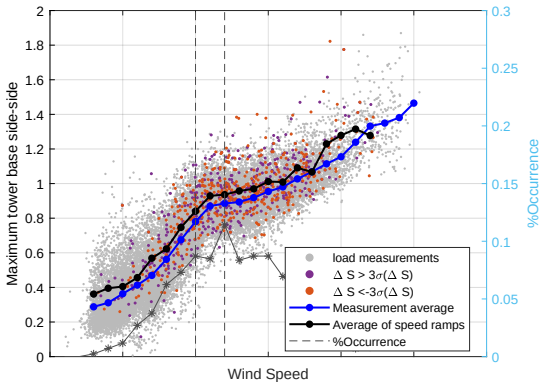

(h) Maximum Tower base side-side moment

Figure C.11: Maximum tower top and tower base bending moments. All values are normalized with the minimum average DLC 1.2 bending moment at the rated wind speed.

C.7. High-frequency events

An event of σ_u > ETM B

For the selected extreme fluctuation events (σ_u > ETM B) event, tower side-side moments exceeded DLC 1.3 simulations. The corresponding time periods are shown in the red boxes Figure C.14. The higher fluctuations in tower side-side moments (Figure C.14 (f) and (i)) could be related to the fluctuating wind speed (Figure C.14 (a)), wind-wave misalignment or yaw error. However, higher frequency time series of wind and wave directions were nor available for this thesis

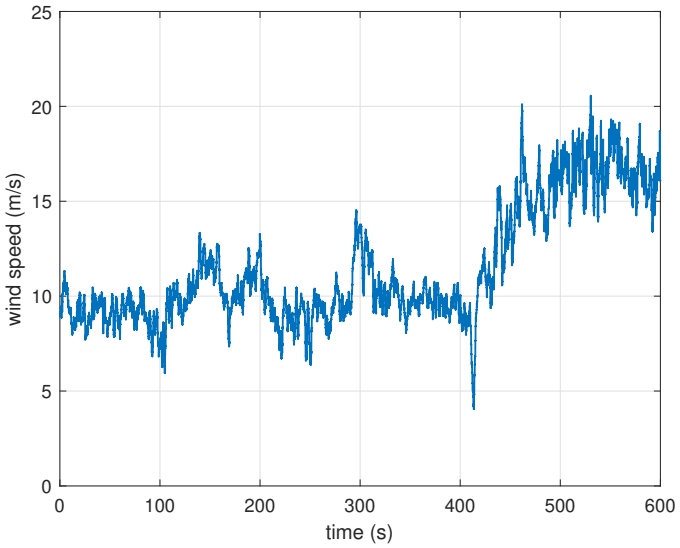

Figure C.12: High-frequency wind speed time series of an event with σ_u > ETM B.

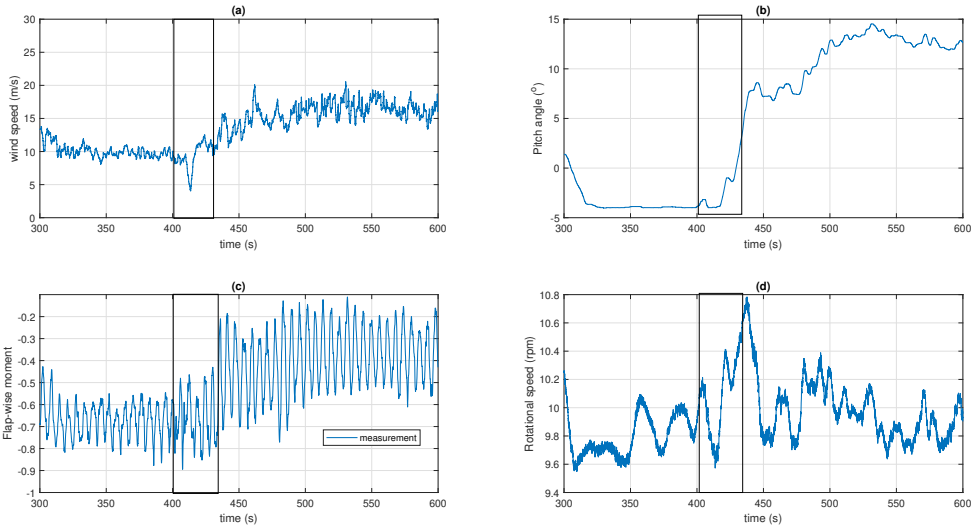

Figure C.13: High-frequency time series of (a) wind speed (b) normalized blade root flap-wise bending moment (c) pitch angle (d) rotational speed

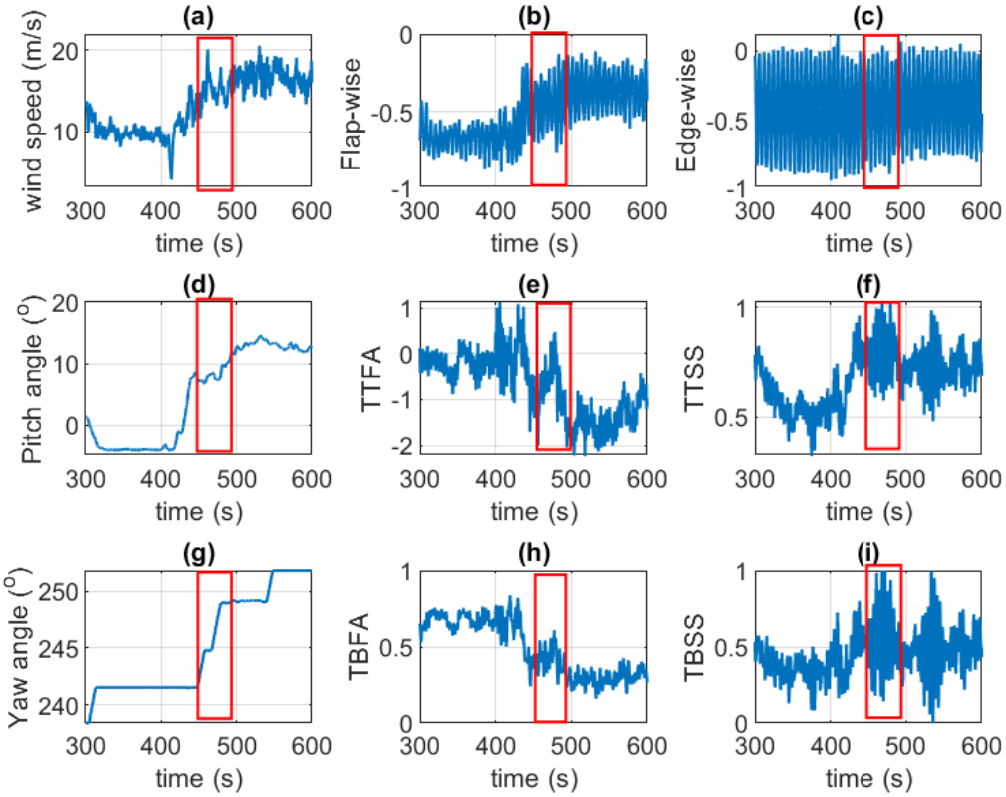

Figure C.14: High-frequency time series of wind speed, pitch angle yaw angle and normalized blade root, tower top and base moments.